



# UNIVERSITÀ DEGLI STUDI DI PALERMO

Dottorato di ricerca in Civil, Environmental and  
Materials Engineering  
Dipartimento di Ingegneria (DI)  
S.S.D. ICAR/02

## THE ROLE OF HYDROLOGICAL PROCESSES ON ENHANCED WEATHERING FOR SOIL CARBON SEQUESTRATION

Ph.D. STUDENT  
**Ing. GIUSEPPE CIPOLLA**

TUTOR  
**Prof. LEONARDO NOTO**

COORDINATORE  
**Prof. ANTONINA PIRROTTA**

CO-TUTOR  
**Prof. AMILCARE PORPORATO**  
**Dott. SALVATORE CALABRESE**

Cycle XXXIV  
2022





# Ringraziamenti

Ho iniziato questo percorso quando avevo appena 23 anni, ero piccolo, non sapevo cosa mi riservasse il futuro e mi sentivo impreparato a lasciare la Sicilia (come la maggior parte delle persone a cui dicevo di fare ingegneria suggeriva). Poi è arrivata la proposta, quella di un professore universitario, quella che non ti aspetti. Chiaramente non avevo la più pallida idea di cosa significasse intraprendere un percorso del genere, per cui, spinto dalla passione per l'idrologia e dal desiderio di crescere professionalmente, ho deciso di accettare. Devo dire che in tre anni sento di averne fatta tanta di strada, sento di essere maturato molto, sia professionalmente che caratterialmente, soprattutto grazie all'esperienza a Princeton, in America! Sento che questa esperienza di tre anni mi ha regalato tanto e mi ha fatto conoscere tante belle persone, che pertanto qui ringrazierò.

Parto ringraziando chi ha creduto molto in me, il Professore Leonardo Valerio Noto, che mi ha preso quando avevo appena 21 anni, per la tesi triennale e mi ha seguito, come un "genitore accademico", fino a questo giorno. Da lui ho imparato tanto, per questo a lui devo tanto. Ringrazio molto l'ingegnere Antonio Francipane che, con la sua immensa professionalità, mi ha seguito anche lui sin dal primo giorno, rendendo tutto molto più leggero con la sua simpatia. Ringrazio l'ingegnere Dario Pumo, del quale ho apprezzato le doti accademiche nelle poche volte con cui ho collaborato con lui. Un sincero ringraziamento va ai miei supervisor esteri, il Prof. Amilcare

Porporato e il Dott. Salvatore Calabrese. Loro sono dei pozzi di scienza, ma soprattutto ho apprezzato l'umiltà con cui si sono posti con me, seguendomi pedissequamente su tutto, riflettendo sugli argomenti insieme, come se lavorassimo insieme da sempre.

Trasferendomi al lato familiare, un immenso e sentito ringraziamento va ai miei genitori, Raffaele e Loredana, e mio fratello Claudio, per aver sempre creduto nelle mie scelte e per aver seguito questi miei tre anni festeggiando ogni traguardo con tanta gioia. Ringrazio con il cuore in mano (e le dita tremolanti) i miei nonni Pino ed Enzina e la mia cara zia Rita. Del primo, in particolare, sento di aver ereditato qualcosa di importante, un talento, che consiste nell'affrontare ogni cosa con estrema calma e razionalità. Loro non sono più fisicamente con me, ma sento di averli vicini ogni giorno. Ah, quanto sarebbero fieri di me oggi! Un grazie speciale alla nonna Lina, che è sempre tanto tanto affettuosa nei miei confronti, vantandomi con gli altri come il suo "scienziato". Un grande grazie va a mio nonno Paolo, che purtroppo ho conosciuto troppo poco. Ringrazio i miei zii Salvatore e Mariella, per i quali provo un affetto che non è possibile descrivere. Per loro: ogni tanto, tra una nuotata e l'altra, trovo il tempo di lavorare :). Ringrazio di cuore mio zio Giuseppe. Lui è stato e continua ad essere più di un semplice zio, è una guida, la persona con cui sento di confidarmi per prima quando c'è una decisione importante da prendere. Ringrazio le mie cugine, per meglio dire sorelle, Silvia, Chiara e Sophie. Per loro sono il cuginetto pieno di soldi :), ma anche quello di cui vanno tanto orgogliose, dimostrandomi il loro affetto in tutti i modi. Infine, nella sfera

familiare, ringrazio Valerio e Sergio, per aver sempre dimostrato tanta stima e amicizia nei miei confronti.

Spostandomi alla sfera degli amici, non posso che ringraziare le persone con cui ho condiviso tutti i miei anni accademici, Francesco, Dario e ultimamente Piero. Siete stati la mia costante, avete reso ogni giorno più leggero con le vostre battute (e le imitazioni di Piero) e grazie a voi è un piacere venire a lavorare. Ringrazio Taise, presenza importante nel corso del mio primo anno, che continua ad esserci nonostante il tempo e le svariate migliaia di km di distanza. Ringrazio Pietro, collega con cui ho condiviso momenti di gioia e di disperazione (soprattutto alla fine). Ringrazio Laura, Michele, Francesco, Alice e tutti gli altri amici con cui ogni giorno passato in dipartimento diventa sempre meno pesante. Ringrazio anche Felix, Sophie, Sara, Shashank e Sam, persone speciali con cui ho condiviso in mio periodo negli States. Un grazie va anche a quelle persone che dall'inizio dell'università si sono dimostrate sempre presenti, ossia Tommaso, Antonio, Ruggero, Chiara, Mario e Matteo, dimostrandomi che l'amicizia va oltre il tempo e le strade che inevitabilmente portano a dividersi. Ringrazio inoltre la mia combriccola di Partinico, ossia Lorenzo, Katia, Vincenzo, Salvo, Antonio, Giuseppe X3 :), Alessia, Serena, Federica e Valeria, per avermi accompagnato in questo mio percorso con stima e affetto. Ringrazio i miei grandi amici del nuoto libero, Salvo, Antonio, Giacomo, Benedetto, Vincenzo, Riccardo e Rosario. Con voi il risveglio all'alba (inverno ed estate) e la nuotata al mare è la carica migliore che ci sia per cominciare la giornata.

Infine, un ringraziamento speciale voglio farlo a me. La persona che sono oggi è frutto soprattutto del mio carattere, di come mi sono rialzato in passato ogni volta che sono caduto. Una parte importante di questo è dovuta alla mia grande passione per lo sport. Negli anni, lo sport mi ha insegnato che cosa vogliono dire sacrificio, sofferenza e impegno per conquistare ogni singola cosa. Lo sport, il nuoto in particolare, è quella cosa che mi fa stare bene quando sono triste, quella cosa che mi spinge a migliorarmi ogni giorno, in tutto quello che faccio. Un ultimo grazie lo devo alla mia terra, alla mia Sicilia che, ogni giorno, regala emozioni e che proverò a non lasciare mai, con la promessa di fare qualcosa, seppur piccola, per migliorarla. Tre anni meravigliosamente trascorsi, ma è soltanto l'inizio!

Giuseppe Cipolla

# Table of contents

Introduction.....	10
Chapter 1 - Climate change and impacts.....	18
1.1 Aridity and desertification .....	23
1.2 Ice melting and sea level rise.....	27
1.3 Increase of weather extremes .....	36
1.4 Influence of climate change on wildfires 53	
1.5 Climate change effects on food security	62
Chapter 2 - Climate change adaptation strategies .....	68
2.1 The SRM techniques .....	72
2.2 The CDR techniques .....	90
Chapter 3 - Enhanced Weathering for carbon sequestration: state-of-the-art and uncertainties .....	104
3.1 Chemical weathering .....	104
3.2 State-of-the-art of EW .....	108
3.3 Uncertainties of EW in field.....	128
Chapter 4 - EW Modeling: rock-dissolution reactions coupled to plant, soil moisture and carbon dynamics ...	138
4.1 Modeling scheme .....	140
4.2 Reduced-order model .....	162

4.3 Model Summary and Numerical Simulations .....	166
Chapter 5 – The role of hydrology on EW: from hydroclimatic scenarios to carbon-sequestration efficiencies.....	180
5.1 EW scenarios and parametrizations....	181
5.2 Climate effects on EW.....	193
5.3 The role of organic matter on EW .....	199
5.4 Analysis of EW benefits.....	204
Chapter 6 – Effect of seasonal variability of precipitation and vegetation cycle on enhanced weathering dynamics: an application for Italy and USA.....	210
6.1 Materials and methods.....	212
6.2 Results .....	231
Conclusions.....	252
Appendix A – List of abbreviations .....	262
References.....	270

# Introduction

Climate change is defined as a long-term variation of local, regional or global weather patterns, that can be attributed to several causes, both natural and anthropic [1-3]. It is clear that, regardless of the cause, a modification in climate characteristics (e.g., temperature and precipitation patterns) affects human society and, for this reason, an in-depth analysis and characterization of this phenomenon is needed. The changes in global climate patterns, that have been observed starting from the beginning of the 20<sup>th</sup> century, are mainly attributed to anthropogenic activities, such as fossil fuels burning, that have been leading to an increase in the greenhouse gases concentration in the atmosphere and a consequent global warming due to the modification of the Earth's energy balance [4,5]. This latter aspect is visible in the significant increase of the global surface temperature in the last 20 years, as compared to the pre-industrial era (1850-1900), significant of the effect of human activities. For this reason, the term “anthropogenic climate change” has been introduced by the scientific community to refer to all climate alterations induced by human activities, thus separating them from those related to natural phenomena. The first chapter of this thesis is therefore devoted to define various sources of climate change, with a particular attention to the anthropogenic ones, and the related consequences on human society. Among all the possible climate change effects, some

studies about desertification, ice melting and sea level rise, the increasing occurrence of weather extremes and wildfires and also its influence on food security are deeply discussed.

In perspective to face climate change, a collective goal to hold global temperature rise below 2 degrees, with a particular effort to limit it to 1.5 degrees above pre-industrial levels by 2030, has been adopted by several countries in 2016 in the adoption of the Paris Agreement [6]. To achieve it, several mitigation measures have been analyzed by the scientific literature and, some of them, are starting to be implemented. Since the reduction of fossil fuels use may not be enough to avoid the most catastrophic consequences of climate change [7,8], given the already high greenhouse gases concentration in the atmosphere, mitigation measures are mostly devoted to sequester atmospheric carbon (i.e., Carbon Dioxide Removal, CDR, techniques) or to reduce the incoming solar radiation from space (i.e., Solar radiation Management, SRM, techniques). To this regard, the second chapter of the present thesis runs into the most important existing technologies, belonging to the two above-mentioned categories. By reducing the incoming extraterrestrial solar radiation or the portion of it adsorbed by the Earth, the SRM techniques aim to reduce the global temperature increase, by means of declining the greenhouse effect due to the presence of a relevant current greenhouse gases concentration in the atmosphere. This goal may be achieved by i) increasing the reflectivity of the Earth surface, by, for instance, enhancing the amount of white surfaces, ii) enhancing the marine cloud reflectivity,

iii) increasing the reflectivity of the stratosphere with aerosol particles or iv) enhancing the reflectivity of the last layer of the atmosphere by means of some shields and mirrors in space. Each of these alternatives has its own advantages and drawbacks, the latter mainly related to leave unchanged the atmospheric greenhouse gases concentration. The most studied methods by the scientific literature regard the terrestrial albedo increase [9], the stratospheric aerosol injection [10] and the marine cloud brightening increase [11].

The CDR technologies, instead, aim to sequester the carbon contained in the atmospheric CO<sub>2</sub> and store it within oceans, vegetation or other terrestrial environments, leading the climate to a similar pre-industrial condition [12]. Their main concern is related to the time the carbon remains stored, that must be long enough to avoid release in the atmosphere after being captured, but also the impact of the adopted technique on terrestrial ecosystems. Unlike the SRM ones, they require a longer time to act, but may provide a greater cooling effect of the Earth (depending on the stability of the carbon storage) since they act on the composition of the atmosphere. The mostly known CDR methods are afforestation [13], the carbon capture by means of biomass or chemical sorbents, the direct air capture [14], the enhancement of oceanic CO<sub>2</sub> uptake and the enhanced chemical weathering in soils [15].

Among these CDR technologies, the present thesis focuses on Enhanced Weathering (EW), that is referred to as one of the most promising strategies to mitigate climate change [16,17]. This technique aims to sequester

atmospheric CO<sub>2</sub> by increasing the rates of naturally occurring chemical reactions in soils, using highly reactive minerals (i.e., silicates) [18]. These processes are favored by hot and humid climatic conditions and also by acid soils [19]. Reacting with CO<sub>2</sub>, silicate grains allow the formation of dissolved bicarbonate (HCO<sub>3</sub><sup>-</sup>) and carbonates (CO<sub>3</sub><sup>2-</sup>), that are leached out of the soil, transported by groundwater, and eventually reach the oceans. Among the various existing silicate minerals, Forsterite (chemical formula: Mg<sub>2</sub>SiO<sub>4</sub>), often referred as olivine, is considered one of the most suitable minerals for EW, given its relatively high dissolution rate, as compared to other silicate minerals, such as albite and orthoclase and abundant presence in the world [15].

So far, the scientific literature has not provided studies about actual applications of EW for carbon sequestration. Asibor, *et al.* [20] provides the technological readiness level for the most common CDR strategies (i.e., forestation, direct air capture, biochar and EW), highlighting that the knowledge of EW process is currently stopped to some pilot scale experiments, given large uncertainties in scaling up laboratory results to field scale [21]. In the last decade, several experimental approaches have been carried out to characterize olivine, or any other silicate mineral used for EW, dissolution dynamics. These are mainly based on laboratory experiments conducted on single mineral particles [22,23] or pot and mesocosm experiments [24-28], with conditions that are more similar to the field.

Laboratory conditions for the derivation of dissolution rate are usually ideal, considering low pH (i.e., 5), high

temperatures (i.e., 25 °C), far from equilibrium conditions for the reaction and considering olivine particles as perfect spheres with diameters of the order of magnitude of a few microns. However, laboratory and field weathering rates may differ a lot for a huge number of intrinsic and extrinsic factors [21] that in laboratory are difficult to be quantified. The most common uncertain aspects regard the formation of secondary minerals, the alteration of soil hydrological properties due to silicate amendments, the formation of preferential flow path in soil pores and the action of fungi, bacteria and microbes that, depending on soil pH, may accelerate or slow down the organic matter decomposition, which is one of the CO<sub>2</sub> sources, and silicates dissolution rate [29]. These uncertainties in field weathering rate estimation inevitably affects the evaluation of a realistic carbon sequestration rate of EW.

To address this lab-field gap, some models have been developed, in order to extrapolate results of laboratory and field experiments in both time and space, as well as for quantifying the impact of hydroclimatic fluctuations on the involved biogeochemical processes. These are known as reactive transport models and basically consist of simulating the interactions among plants and soil biogeochemistry, taking into account, in some cases, the EW process [30]. However, most of these models present many uncertain aspects and limitations. Indeed, not all the above-mentioned processes, and the occurring biochemical reactions in the soil, are considered at the same time. One of the most critical aspect is that, for the sake of simplicity, they often consider homogeneous hydraulic and chemical

properties of the soil, which is far from natural conditions. Furthermore, hydrologic fluctuations of rainfall and its seasonality, that reflect in soil moisture, are never taken into account. This is a strong limitation when, especially for EW, the role of hydrological processes is very important.

Chapter 4 of this thesis attempts to overcome these aspects by presenting a complex mathematical model coupling the key ecohydrological and biogeochemical aspects of EW with a stochastic rainfall forcing. The model, extensively described in Cipolla, *et al.* [31] and Cipolla, *et al.* [32], is composed of four closely related components, starting by modeling the organic matter decomposition, which provides one of the sources of CO<sub>2</sub> in the system, the mass balance of CO<sub>2</sub> in the gas and dissolved phases, the balance of ions not containing carbon (silicates and plant nutrients, such as Mg<sup>2+</sup>, Ca<sup>2+</sup>, K<sup>+</sup> and Na<sup>+</sup>) and the cation exchange process between the dissolved cations and the solid matrix of the soil. The whole system is forced externally by rainfall, which can be in the form of a stochastic or a real time-series. Model applications allow exploring the influence of hydrological fluxes on the individual components of the model, looking especially at soil moisture, pH, weathering rate, and carbon sequestration time dynamics. In chapter 4 the main structure of the model is presented and is followed by a detailed explanation of the constituting equations. After that, a reduced-order version of the model and a scheme of its resolution are provided. Some general applications regarding the role of wetness, cation exchange capacity and plants on EW dynamics are also described here.

Chapter 5 of the present thesis is devoted to a more in-depth application of the here developed EW model, with the aim to figure out which climate conditions, hence areas of the world, may be more suitable to EW, by means of quantifying the actual rates of CO<sub>2</sub> sequestration resulting from olivine dissolution for given climate and land use conditions, including the presence of soil organic matter. In the applications presented in this chapter, the way in which EW dynamics evolve under different stationary precipitation scenarios is analyzed, in order to identify the role of hydrological fluxes on EW. These analyses, in fact, may be a starting point for decision makers to select the most suitable regions of the world in perspective to put EW into practice. A possible improvement of EW yields by amending soil with organic matter is also explored, looking at how much weathering and carbon sequestration rates vary after soil is amended with a certain amount of organic matter. All of these applications consider as constant soil and vegetation parameters, along with the carbon input and the input of calcium, magnesium, potassium and sodium coming from atmospheric deposition, return of cations from plant litter and input from minerals dissolution. Despite these assumptions may be applied to understand the effect of different climatic conditions on olivine dissolution and carbon sequestration dynamics, since MAP is the only parameter that varies, they cannot be applied if one thinks to apply the model to some real case studies. In these latter applications, in fact, it is fundamental to characterize the seasonal variability of many variables of the model, such as rainfall, vegetation cycles and carbon

and cations input to the soil. In this regard, chapter 6 of this thesis regards the application of the EW model to four hypothetical case studies (i.e., agricultural EW applications), i.e., Sicily and the Padan plain for Italy and California and Iowa in the USA. The four places are characterized by very similar MAP values but much different rainfall seasonality. They also present similar soils and different crop types. Furthermore, differences among the selected places in terms of cation exchange capacity and background weathering flux are here taken into account, given that these factors strongly affect soil pH before olivine amendment. The main goal of these analyses is therefore to understand which of the considered factors (i.e., rainfall seasonality, soil type and composition and crop cycle) is mostly connected to changes in EW time dynamics. Moreover, they allow to define the most suitable combined characteristics of climate, soil and vegetation to host an EW intervention. After the six chapters shortly introduced above, the present thesis includes a final section summing up the main conclusions of the work here described, highlighting the main obtained key results with a critical view towards future developments.

# Chapter 1 - Climate change and impacts

It is widely acknowledged that climate influences human societies in several ways, and an alteration of it, whatever the cause, reflects on everything that surrounds us. Climate has always experienced a sort of natural variability due to its chaotic nature [1,33,34]. For example, Ghil [1] refers to periodic variations in Earth's orbit around the sun that, at long time scales, influence the intensity of solar radiation captured by the Earth. Furthermore, there could be some climate variations attributed to volcanic eruptions, that are external to the climate system, or weather fluctuations, which instead are internal to the climate system, that occur at time scales of the order of magnitude of millennia and are unpredictable.

However, since the mid-20th century, there has been a significant increase of Greenhouse Gases (GHG) emissions due to anthropogenic activities. This has led to typical manifestations of global warming due to an alteration of the earth's energy balance [4,35-37]. Indeed, a greater concentration of greenhouse gases in the atmosphere results in a greater amount of longwave radiation, emitted by the Earth, that remains trapped within the atmosphere, since it is adsorbed and re-emitted at all directions, including the Earth surface, by the greenhouse gases. This inevitably leads to an increase in the global temperature and is known as the “greenhouse effect”. The last report from the

International Panel on Climate Change (IPCC) [2] has highlighted that the globally averaged land surface air temperature has risen faster than the global mean surface temperature (i.e., the one defined considering both land and sea surface temperatures), considering the time window from the pre-industrial period (1850-1900) to the last 20 years (2000-2020), as shown in Figure 1, extracted from Jia, *et al.* [2]. Respect to the average values calculated in the period 1850-1900, the globally averaged land surface air temperature (i.e., orange line in Figure 1) has reached an increase of about 1.5 °C in 2020, while the global mean surface temperature (i.e., blue line in Figure 1) is characterized by an increase of about 1 °C in 2020. The most worrying thing is that the increasing trend of both temperatures started to become relevant in the last 20 years, especially the one related to the globally averaged land surface air temperature. This means that the warming rate on land is significantly higher than the one on the oceans, leading to several impacts for terrestrial ecosystems and land.

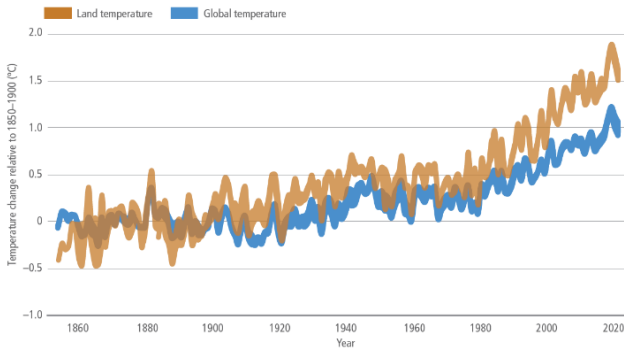


Figure 1 – Evolution of the globally averaged land surface air temperature (i.e., orange line) and of the global mean surface temperature (i.e., blue line) respect to the period 1850-1900 (figure taken from Jia, *et al.* [2]).

As stated in Jia, *et al.* [2], global warming has already resulted in several consequences on organisms and ecosystems, as well as on human systems and well-being, that are expected to significantly grow if no actions will be taken to face this phenomenon in the near future [38]. In Allen, *et al.* [39], five Reasons For Concern (RFC) are introduced to summarize the key impacts of climate change and related risks for ecosystems. In Figure 2, impacts at different scales are illustrated along with the global mean surface temperature increase respect to the pre-industrial level. In particular, the RFC1 regards those systems that are particularly vulnerable to climate change impacts. Among them, it is possible to mention coral reefs, the Arctic and its indigenous people, mountain glaciers and biodiversity hotspots. RFC2 is related to the more frequent occurrence

of extreme weather events, such as heatwaves, heavy rain, drought and associated wildfires, and coastal flooding. Then, RFC3 deals with an uneven distribution of climate change impacts across the globe, highlighting that some areas will be affected more than others. For instance, various regions of Africa and Asia are more likely to be involved in water scarcity and water quality issues more than other parts of the world, if no action is taken in the near future to mitigate global warming. RFC4 analyzes global impacts, with reference to economic damages, global-scale degradation and loss of ecosystems and biodiversity. Under a warmer world, in fact, there is a high risk of extinction for some local species, due to the spread of pests, diseases and forest fires. Even ocean ecosystems are involved in the changing climate. With warmer water temperatures, in fact, some species are bound to migrate and create their ecosystem at higher latitudes. Lastly, RFC5 concerns large-scale singular events, i.e., abrupt and sometimes irreversible changes in systems, such as disintegration of the Greenland and Antarctic ice sheets.

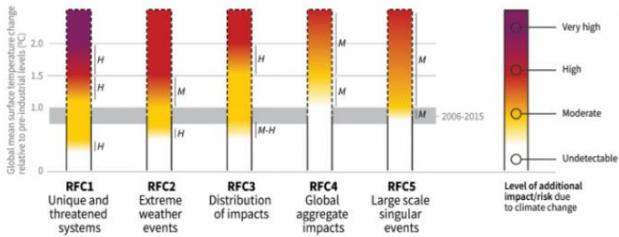


Figure 2 – Five Reasons For Concern (RFC) presenting the impacts and risks of climate change for human society, economy and ecosystems. The colorbar indicates different levels of risk according to the global mean surface temperature increase respect to the pre-industrial levels. The figure is extracted from Allen, et al. [39].

Considering what shown in Figure 2, the most important climate change effects are better described in the sub-sections reported below, where some works that carried out some analyses to quantify the impact of the actual stage of global warming, also making future predictions are presented. In particular, the chapter focuses on the increase/decrease in dry/polar climates worldwide [2], that leads to several consequences, such as desertification [40-45], ice melting and consequent sea level rise [5,46-50], the increase of the frequency of many types of weather extremes [51-56] and a more frequent occurrence of wildfires [57-61]. In addition, a topic that has raised particular interest in the scientific community over the last years regard the influence of climate change on food security [62-67].

## 1.1 Aridity and desertification

Desertification is defined as a rapid change in soil properties, vegetation or climate, resulting in a persistent loss of ecosystem services that are fundamental for life. D’Odorico, *et al.* [44] analyzed various drivers and impacts of desertification at a global scale, trying to understand if climate change can be considered as one of the major drivers of this phenomenon. The authors highlighted that desertification is strongly connected to changes in global patterns of temperature and precipitation, which are due to climate change. The rapid anthropogenic global warming manifested after the industrial era, through the increase of greenhouse gases emissions, significantly contributed to the expansion of dry areas worldwide. In particular, some projections on climate change affirms that a huge part of the Earth, including Northern Africa, Amazonia and the USA, will experiment very dry conditions by the end of the 21<sup>st</sup> century. Desertification leads to several impacts for population. Among these, one of the most relevant is related to the agriculture sector. D’Odorico, *et al.* [44] affirms that the increase of drought could result in a 10%-decrease of maize production by 2055 in Africa and Latin America. One can imagine that this aspect is a serious threat to sustainable livelihoods. Due to temperature increase and precipitation reduction, climate change inevitably causes a decrease in soil moisture, especially in the most semi-arid regions of the world, leading to the expansion of the existing deserts or the formation of new ones, mainly due

to the loss of vegetation. Samaniego, *et al.* [42] estimated the impacts of future climate change scenarios on drought over Europe. The authors considered five global warming scenarios (i.e., 1, 1.5, 2, 2.5 and 3 K) and compared the resulting effects to those related to the 1.5 K target of the Paris agreement. A comparison with a historical condition, related to the period 1971-2000 is also taken into account. Two drought indicators have been defined, i.e., the area covered by drought and the drought duration, by means of coupling multiples hydrological and land-surface models. Results showed that, moving from the 1 K to the 3 K scenarios, there is an increase of the area characterized by drought and, at the same time, a growth of the drought duration. Figure 3, extracted from Samaniego, *et al.* [42], displays the spatial distribution of the drought area, duration and frequency across Europe under the five analyzed global warming scenarios. The most severe drought conditions are expected to occur in correspondence of the Mediterranean area, reaching a fraction of about 50% under the 3 K scenario. In general, also the rest of Europe could experiment more severe drought conditions under this scenario, comparing to the historical condition. Regarding the drought duration, the same pattern of the area covered by drought has been detected, with a significant increase of the duration of the largest drought events under the 3 K scenario with respect to the historical condition. This inevitably reflects on the drought frequency. These results strongly highlight the importance of contrasting climate change and avoiding a global

temperature rise beyond the 1.5 K above pre-industrial levels scenario fixed by the Paris agreement.

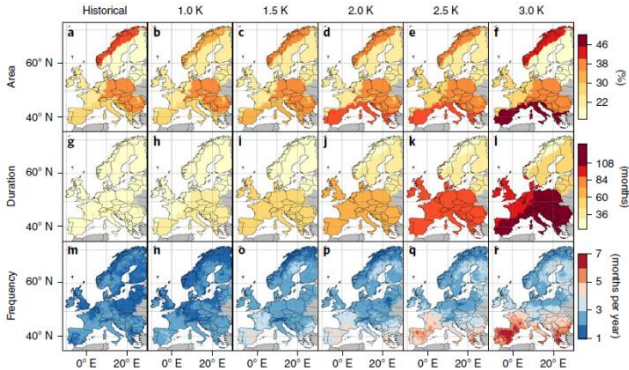


Figure 3 – Spatial distribution of the fraction of (panels a-f) area covered by drought, (panels g-l) the drought duration and (panels m-r) the frequency of drought duration, expressed in months per year, under the historical condition and the five simulated global warming scenarios. The figure is taken from Samaniego, *et al.* [42].

As previously stated, increases in desertification may be due to vegetation cover losses. To this regard, Burrell, *et al.* [41] quantified the changes in vegetation cover at a global scale predominantly caused by anthropogenic climate change by using satellite data. When talking about anthropogenic climate change, the authors consider trends in temperature and precipitation and also the water use efficiency of plants, which is the carbon gain during photosynthesis per unit of water lost (i.e., transpiration). This latter has increased due to climate change since there

has been an increase of available CO<sub>2</sub> in the atmosphere. The authors call this increase of water use efficiency due to the greater amount of atmospheric CO<sub>2</sub> as “CO<sub>2</sub> fertilization”. In this study, the Normalized Difference Vegetation index (NDVI) is derived from satellite maps and a non-parametric trend analysis is applied to the maximum NDVI in correspondence of the growing season, with the aim to identify significant changes of vegetation cover. Results, reported in Figure 4, show that, at the global scale, anthropogenic climate change leads to a general increase of vegetation cover, that is mainly due to CO<sub>2</sub> fertilization. However, many regions of the world are characterized by a negative impact of climate change, which is visible, in Figure 4, in the negative variations of the maximum NDVI. This effect cannot be neglected since the desertification of these areas affects 213 million people.

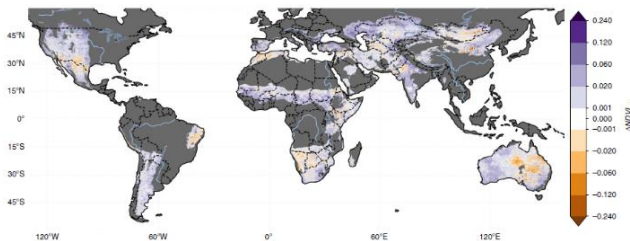


Figure 4 – Global variation of the maximum NDVI during the growing season due to anthropogenic climate change, evaluated in the period 1982-2015. The figure is taken from Burrell, et al. [41].

## 1.2 Ice melting and sea level rise

It is known that ice melting is connected to sea temperature rise, thus to global warming. A consequence of the ice melting is certainly the sea level rise that can lead to several phenomena, such as inundation of terrestrial coastal areas [68] and a loss of wetlands [69]. These aspects are added to the loss of permafrost with consequent damages for living ecosystems in the Arctic land [70]. Figure 5, taken from the National Oceanic and Atmospheric Administration (NOAA) Arctic Report Card (<https://arctic.noaa.gov/Report-Card>), compares the minimum of Arctic Sea ice extent reached in 2020 with its median extent related to the period 1981-2010. It is here visible that there has been a significant reduction of sea ice extent among this time period. Furthermore, the lower panel of the figure shows that the daily Arctic sea ice extent in 2020 is significantly less than in previous years, with a decreasing trend from the 1981-2010 average onwards.

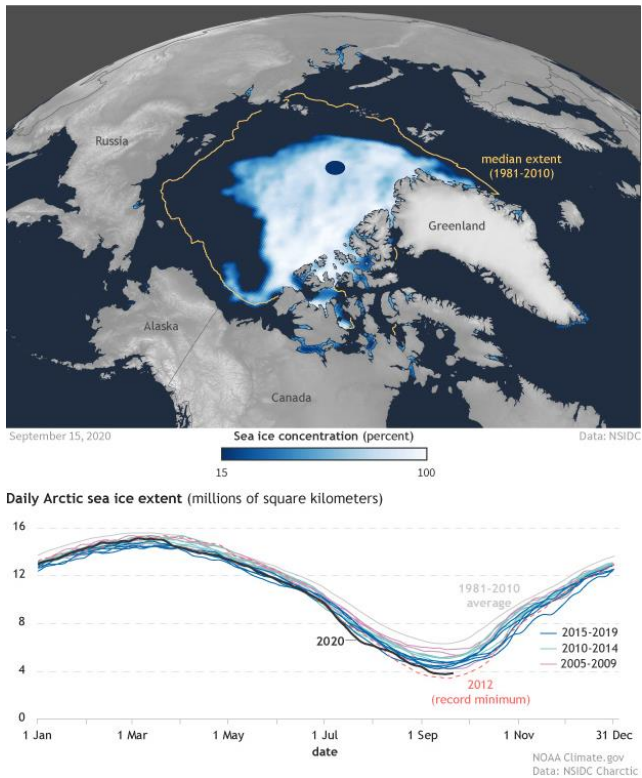


Figure 5 – Summer minimum of Arctic sea ice extent reached in 2020 compared with the median extent calculated in the period 1981-2010 (upper panel). In the lower panel of the figure, a comparison of the average daily arctic sea ice extent over different time periods within the time window 1981-2020 is shown. Figure provided by NOAA.

Shepherd, *et al.* [5] affirms that one of the relevant indicators of climate change could be the status of the

Antarctic Ice Sheet since its potential contribution to the global sea level rise, due to its melting, may be by 58 m [71]. For this reason, the authors estimated the mass changes of Ice Sheet in various regions of Antarctica in the period 1990-2017 and its contribution to sea-level rise. Their approach combines different estimates of ice-sheet mass balance, such as those based on satellite altimetry, gravimetry, input-output method and model estimates of Surface Mass Balance (SMB) and Glacial Isostatic Adjustment (GIA). Their analysis was carried out for the East Antarctic Ice Sheet (EAIS), West Antarctic Ice Sheet (WAIS) and Antarctica Peninsula Ice Sheet (APIS). Combining the Ice Sheet mass changes for these regions, the authors found the mass changes and the related uncertainties for the whole Antarctica. All results are also compared with a previous approach conducted by the same authors in 2012 (IMBIE 2012). In Figure 6, the annual Ice Sheet mass changes with the uncertainty thresholds related to the period 1990-2017 and the different regions of Antarctica are reported. In the same plot, the corresponding contribution to sea-level variation is reported. It is here possible to observe that, excluding EAIS, all the other regions of Antarctica under study have shown a decrease of Ice Sheet mass, which is more significant at WAIS and the whole Antarctica region. Furthermore, this decreasing trend becomes more relevant from 2005 onwards, highlighting the progressively more damaging effect of global warming. Especially looking at the whole Antarctica region, the contribution to sea-level rise is important (i.e., about 8 mm) and this trend will continue or be exacerbated

if no actions to mitigate climate change will be soon introduced.

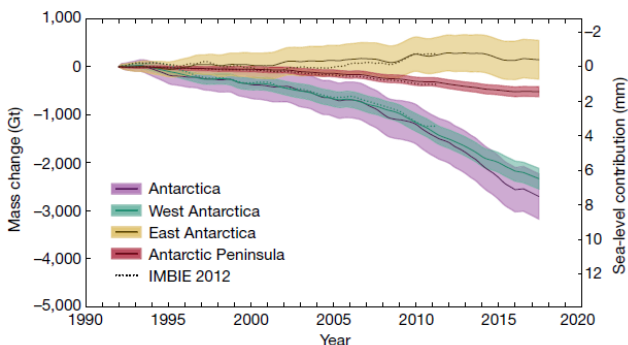


Figure 6 – Annual mass changes of Ice Sheet for various regions of Antarctica. The shaded areas represent the estimated uncertainty thresholds. The contribution, in terms of sea-level rise is also displayed. The figure is extracted from Shepherd, *et al.* [5].

Due to the melting of glaciers, glacial lakes can form. Shugar, *et al.* [46] affirms that, because of climate change, there has been a progressive formation of glacial lakes. If water does not drain away from glacial lakes, glaciers can rapidly reform; otherwise, the drainage can have a negative impact, apart from avoiding the reformation of glaciers, that is given by the modification of hydrologic and geomorphic conditions of the environment. By means of Landsat-8 satellite maps, acquired from 1990 to 2018, the authors were able to quantify the growth of glacial lake areas and volumes at the global scale. The extent of glacial

lakes was obtained through two different optical spectral indices, i.e., the Normalized Difference Water Index (NDWI) and the Normalized Difference Snow Index (NDSI), that let distinguish water and snow from satellite observations on the base of their spectral response and, in particular, using the green and near-infrared bands in the NDWI and the green and shortwave infrared band in the NDSI.

The goal of the study was to understand if, especially in the last decade, climate change has significantly contributed to a substantial glacial lakes formation or expansion. The glacial lakes distribution across the world, assessed for the period 1990-1999, was compared to the one related to the period 2015-2018 and the change, in terms of percentage of land occupied by glacial lakes and their volume, was evaluated. In Figure 7 the volume changes of glacial lake from the period 1990-1999 to 2015-2018 expressed in percentage (panel a) and in terms of absolute magnitude (panel b) are reported. An indication of where the greatest changes are recorded is also provided, showing the glacial lake volume change respect to the latitude and longitude. Comparing the two different time periods, it is shown that the number and area of glacial lakes has consistently increase in the period 2015-2018 respect to the past.

The authors affirm that in the period 1990-1999 there were about 9000 glacial lakes, with an area greater than  $0.05 \text{ km}^2$ , that occupied a total area of about  $6000 \text{ km}^2$ . In the period 2015-2018, instead, the number of glacial lakes increased by 53%, reaching a total number of about 14000,

while their area grew by 51%, reaching a value of about 9000 km<sup>2</sup>. Obviously, there has been a similar increase of the magnitude of glacial lakes volume. The effect of that increase of the number and the volume of glacial lakes corresponds to a sea-level rise of about 0.14 mm. Looking at Figure 7, it is also possible to notice that the greatest increase of glacial lakes volume has been obtained at medium-high latitudes, especially in Alaska, northern Canada, Scandinavia, Greenland and Patagonia. However, some areas of the world, highlighted in blue in Figure 7, were characterized by a decrease of glacial lake volumes, mainly due to drainage of water, rather than the formation of new glaciers.

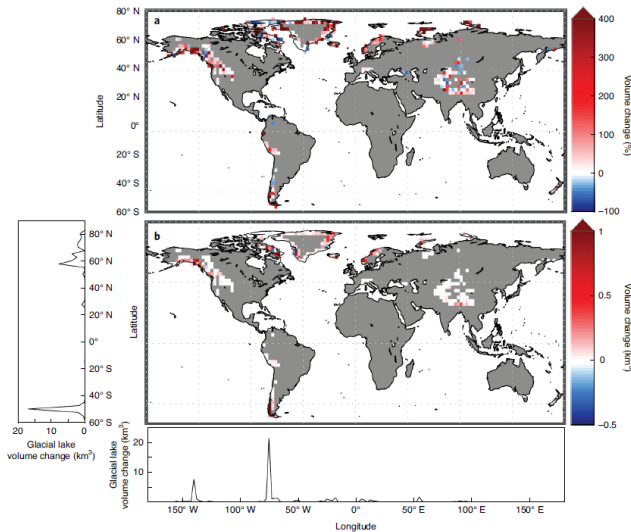


Figure 7 – Change of the volume of glacial lakes from 1990-1999 to 2015-2018 expressed in percentage (panel a) and in  $\text{km}^3$  (panel b). An indication of the locations where the highest changes are recorded is also provided. The figure is taken from Shugar, et al. [46].

An important impact of climate change, connected to ice melting, is related to the changes in the sea surface partial pressure of  $\text{CO}_2$ . Studying these changes is important since the gradient between the sea surface partial pressure of  $\text{CO}_2$  and the partial pressure of atmospheric  $\text{CO}_2$  affects the exchanges of this element between the sea and the atmosphere. A general increase of the sea surface partial pressure of  $\text{CO}_2$  during the last decade has been observed worldwide, due to the atmospheric  $\text{CO}_2$  increase. Since there are few studies about this aspect involving the

Arctic ocean, Ouyang, *et al.* [47] tried to quantify the variation of the partial pressure of CO<sub>2</sub> from 1994 to 2017 in this area, with the aim to analyze how much the ocean carbon cycle is affected by the increase of atmospheric CO<sub>2</sub>, that is clearly attributed to climate change. The authors put together different international datasets of the partial pressure of CO<sub>2</sub>, such as the one of the Carbon Dioxide Information Analysis Center (CDIAC), the Japan Agency for Marine-Earth Science and Technology (JAMSTEC) and the United States Geological Survey (USGS). Combining these datasets, they set up an extensive database containing more than 358,000 data points of partial pressure of CO<sub>2</sub>. All data related to the summer period, which is the period from 1 July to 15 October, have been taken into account since it is the ice-melting season. In Figure 8, extracted from Ouyang, *et al.* [47], the observed partial pressure of CO<sub>2</sub> in the western Arctic ocean related to the summer period between 1994 and 2017 is reported. This figure is composed by overlying the observed annual partial pressure data of CO<sub>2</sub> and highlights that there is a net difference between the Chukchi Shelf area and the Beaufort Sea and Canada Basin. Regarding the Ice-covered region, few changes are reported since ice is a sort of barrier limiting CO<sub>2</sub> exchanges between ocean and atmosphere.

The spatial distribution of the partial pressure of CO<sub>2</sub> appears to have low values in correspondence of the Chukchi Shelf area and very high values at the Beaufort Sea and Canada Basin. Given this observed pattern, the authors decided to differently analyze the reasons why this happens

in the areas under study. In particular, the Canada basin has experienced an increase of partial pressure of sea surface CO<sub>2</sub> more than two times greater than the increasing rate of atmospheric CO<sub>2</sub> and much greater than any other ocean basin. This results in a decreasing gradient among the sea surface and the atmospheric CO<sub>2</sub>, hence in a less CO<sub>2</sub> uptake potential of the ocean. Extending the trend up to 2030, the authors found a very alarming result, consisting of a near zero sea-air CO<sub>2</sub> gradient, meaning that this ocean basin will not be able to uptake CO<sub>2</sub> from the atmosphere anymore. The reason why there is such an increase of CO<sub>2</sub> partial pressure in Canada Basin is that, especially over the last decade, it has been characterized by the ice melting in a very relevant way. The ice melting and the consequent presence of melt water have caused the absence of the barrier for air-sea CO<sub>2</sub> exchanges and, above all, the greater stratification of the ocean, given by the different temperatures of water layers. This leads to a greater difficulty in vertical mixing of water and, therefore, to the limitation of biological and ocean CO<sub>2</sub> uptake.

Regarding the Chukchi Shelf area, instead, it is possible to observe low values of the partial pressure of CO<sub>2</sub>, resulting in a decreasing trend of the gradient with the atmospheric CO<sub>2</sub> among the period 1994-2017. This happens since this area, in general, is characterized by an inflow of water from Pacific Ocean in the summer period that is rich of nutrients. The biomass produced due to this high quantity of nutrients acts as an atmospheric CO<sub>2</sub> sink. This beneficial effect, however, does not protract to the Canada basin since, the water from the Pacific Ocean that

moves towards this area, has a greater density than the water in the Canada basin, leading to the above-mentioned stratification that avoids water mixing and CO<sub>2</sub> exchanges with the atmosphere.

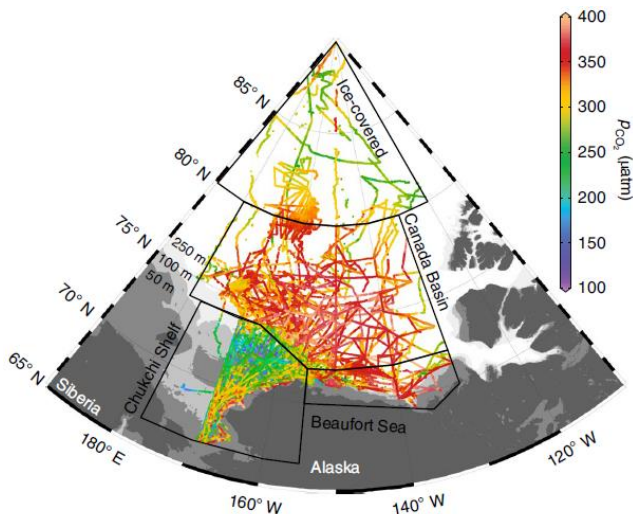


Figure 8 – Spatial distribution of the partial pressure of CO<sub>2</sub> within the summer period between 1994 and 2017. The different analyzed sub-regions are also highlighted with some boxes.

### 1.3 Increase of weather extremes

It is currently well known that climate change has been leading to the increase in the frequency of occurrence of

several types of weather extremes, such as drought and floods. Hegerl, *et al.* [72] affirms that one of the possible fingerprints of climate change is the variation of rainfall characteristics, especially the one related to short-duration and high-intensity precipitation events. Indeed, if they hit small catchments, with low times of concentration, they could result in flash floods, possibly causing loss of human lives and several economic damages [73].

With the aim to assess the response of precipitation extremes to global warming, the INTElligent use of climate models for adaptioN to non-Stationary hydrological Extremes (INTENSE) project was developed to figure out the relationship between large-scale warming, atmospheric circulation, and short-duration extreme rainfall events [55]. To achieve this goal, the INTENSE project based on a huge database of sub-daily rainfall observations at the global scale. The dataset, along with advanced climate models, has been employed to better understand which are the drivers of extreme rainfall events and look at the influence of large-scale atmospheric circulation and local thermodynamics on the extremes. To better understand how the INTENSE project works, its research themes, data and outcomes are shown in the flow chart of Figure 9. The data collection procedure is fundamental for this project. It consists of extracting global sub-daily rainfall, temperature and humidity data from various databases and carrying out homogeneity and quality control procedures. These data are useful to assess changes of extreme precipitation characteristics and for the validation of data acquired from remote. Data are used as input of climate models or for the

validation of their outcomes to better understand the mechanisms (i.e., atmospheric and thermodynamic processes) that are associated with extreme rainfall events. The use of Climate Prediction Models (CPM) is also considered in the INTENSE project since it allows to better characterize, along with ground-based and remote observations, the drivers and impacts of climate change investigating, for example, the influence of local thermodynamics and large-scale atmospheric circulation on rainfall extremes.

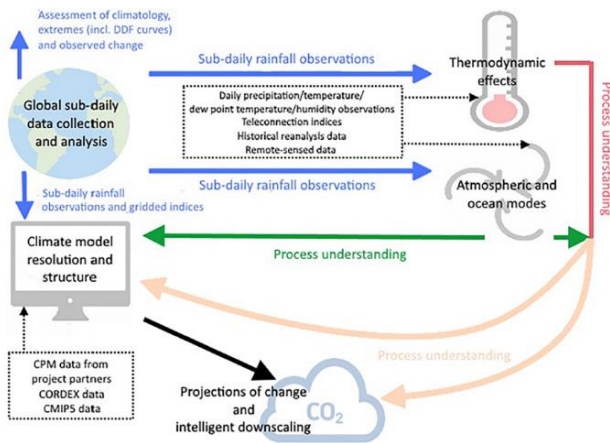


Figure 9 – Flow chart showing the structure of the INTENSE project. The project consists of different parts: the data collection (blue arrows), the understanding of atmospheric and thermodynamic processes (green and red arrows, respectively) and the model outputs (black arrow). The Figure is taken from Blenkinsop, et al. [55].

Regarding the broad-scale atmospheric circulation, Neal, *et al.* [74] presented some weather circulation patterns (WPs) derived by the *UK-Met Office*. Each WP is representative of a specific type of atmospheric circulation over Europe for each day ranging between 1850 and 2016. These WPs have been used by various studies, within the context of the INTENSE project.

Regarding heavy rainfall events, Cipolla, *et al.* [75] connected the atmospheric circulation with the occurrence of rainfall annual maxima over Sicily, the greatest region of the Mediterranean area, in Italy, with the aim to identify which WPs lead to the greatest occurrence of annual maxima, especially those characterized by short durations. The annual maxima used in this study have been recorded at the duration of 1, 3, 6, 12, and 24 hours by a rain gauge network of the *Autorità di Bacino - Regione Siciliana*. The database of the weather circulation patterns, provided by Neal, *et al.* [74] consisted of eight different WPs defined over a European domain centered in the UK. The analyses carried out on the whole sample of the pooled annual maxima, for all the Sicilian rain gauges, highlighted that the major contribution to their occurrence, at all durations, is given by the first WP. This is classified by Neal, *et al.* [74] as a NAO- (negative North Atlantic Oscillation) pattern, in which Sicily is located in correspondence of a negative Mean Sea Level Pressure (MSLP). This pattern results in a displacement of air mass from the North Atlantic Ocean to the south of Europe, where Sicily is located, bringing warm and humid air that probably causes high intensity and short duration rainfall events. This result is confirmed also for

some subsets of annual maxima dataset, made of the most severe ones, namely those higher than the corresponding 75<sup>th</sup>, 90<sup>th</sup>, and 99<sup>th</sup> percentiles. This study, therefore, provides an approach that could be helpful to forecast severe rainfall events by simply monitoring the atmospheric circulation patterns, given that this is shown to be one of the most triggering factors of their occurrence.

Trends related to short-duration precipitation events over the last 20 years have been analyzed by Treppiedi, *et al.* [76]. The analyzed region is the same to that in Cipolla, *et al.* [75], since Sicily is the largest island of the Mediterranean Sea and, due to its central position in the Mediterranean area, it has often been selected for detecting changes in precipitation characteristics, potentially related to climate change. The authors applied the Quantile Regression procedure to detect trends for rainfall time-series provided by the *Servizio Informativo Agrometeorologico Siciliano* (SIAS), at the durations of 10, 20, 30, 40 minutes and 1, 3, 6, 12 and 24 hours and the quantile levels of 0.2, 0.5, 0.9, 0.95 and 0.99, with reference to the period 2002-2019. The significance of trends has been obtained through the t-Student's test, at the significancy levels of 0.05 and 0.1. In Figure 10, the percentage of the Sicilian gauges characterized by a positive/negative/non-significant trend of rainfall intensity in the period 2002-2019 is indicated in red/green/gray. Considering the highest quantiles, which are representative of the most severe rainfall events, it is possible to see a clear increase of the percentage of gauges characterized by a positive trend as the duration decreases. In particular, at 10-

minute duration and 0.95 and 0.99 quantile levels, more than 50 % of the considered gauges shows a positive trend of rainfall intensity. This means that, extreme rainfall events have been increasing over the last two decades, probably as an effect of climate change. Similar results have been achieved by Arnone, *et al.* [77], even using a different dataset, methodology and time window of observation for the trend analysis.

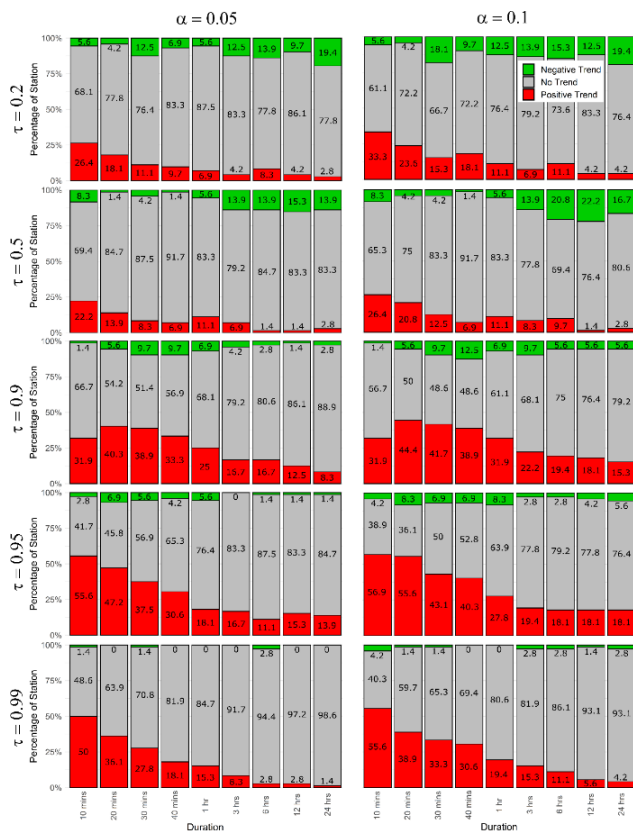


Figure 10 – Percentage of Sicilian rain gauges showing a positive (red), negative (green) and non-significant (gray) trend resulted from Quantile Regression at all the duration and quantile levels under study. The figure is taken from Treppiedi, et al. [76].

Apart from these studies that involve the Mediterranean area, many efforts have been dedicated to understand climate change impacts on the occurrence of extreme precipitation and floods, involving other parts of the world, or at the global scale. For instance, Tabari [52] evaluated the intensification of extreme precipitation and floods events at the global scale with reference to some climate projections related to the end of the 21<sup>st</sup> century. This analysis evaluates the impacts of climate change for various climatic regions, such as the humid, arid and semi-arid ones, due to the fact that changes in precipitation extremes could significantly spatially vary since there are different triggering factors. Furthermore, the relationship of the increase of extreme precipitation with water availability for the above-mentioned areas has been investigated. Precipitation changes are evaluated per K of global warming under the RCP8.5 (Representative Concentration Pathway) scenario and compared with the historical condition, related to the period 1971-2000. The simulations have been carried out by means of 24 Global Climate Models (GCMs) from the Coupled Model Intercomparison Project Phase 5 (CMIP5). Water availability is obtained on the base of the Aridity Index, which is the ratio between potential evapotranspiration and precipitation for a certain time period.

In Figure 11, extracted from Tabari [52], the spatial distribution of the changes of 1 to 30-year return level precipitation intensity, expressed per K of global warming of the 2070-2099 RCP 8.5 climate projection, respect to the historical condition is presented. The figure shows in panels

a-d the changes related to humid, semi-humid, semi-arid and arid regions, respectively. It is here possible to notice that the percentage of 1 to 30-year return level precipitation intensity uniformly increases across all the considered climate regimes. More specifically, the percentage of land area showing this increase is about 99 %. As shown in panel e) of Figure 11, the highest average increase of precipitation intensity is recorded under the humid regions, with a rate of 6.31 %/K, while the lowest one is defined for the arid regions, reaching a value of 5.45 %/K. In this panel the salmon dots represent the changes evaluated by means of different climate models and the salmon curves represent the empirical probability density functions (pdfs) for each climate region. These curves reveal that the variation of precipitation changes (i.e., the width of the curve) tends to increase moving from humid towards arid regions and there are also multiple peaks, representative of different most probable values. Therefore, the study reveal that there may be a significant intensification of extreme precipitation intensity under the projected climatic conditions, all over the world. This intensification is more relevant in humid areas, where water availability is higher and the aridity index is lower. Indeed, a warming climate, especially in more humid areas, increases the potential of the atmosphere to hold more water vapor, as described by the Clausius-Clapeyron (CC) relationship, with a corresponding intensification of the intensity and occurrence of precipitation events. Since floods occurrence is strongly connected to extreme precipitation one, the authors reveal that flood intensity is expected to increase across different

areas of the world following, more or less, the same pattern of precipitation.

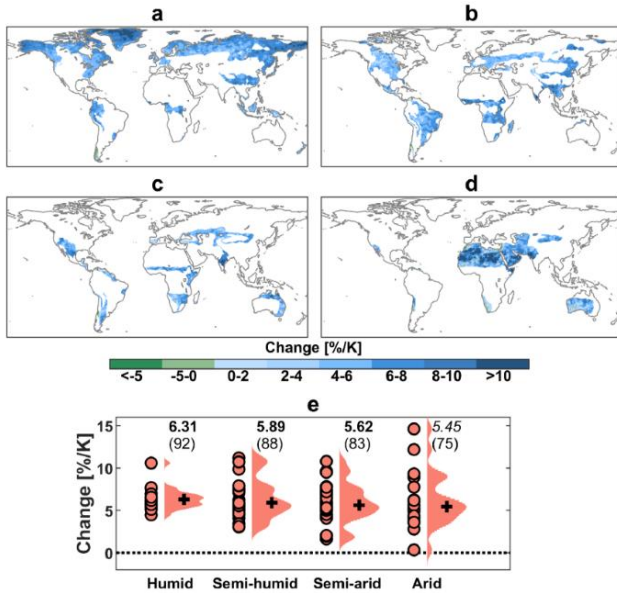


Figure 11 – Changes of 1 to 30-year return level precipitation intensity evaluated per K of global warming in 2070-2099 under RCP8.5 compared to the historical condition (i.e., defined from 1971 to 2000). Panel a) is related to humid, b) to semi-humid, c) to semi-arid and d) to arid regions. In panel e) the pdfs of changes for each climate regime are shown contextually to the median change and uncertainty. The salmon dots represent the results from different climate models. The figure is taken from Tabari [52].

The fact that global warming leads to the increase of extreme precipitation events is also confirmed by Swain, et

*al.* [56]. In this study, the authors analyze extreme precipitation increase due to anthropogenic climate change and connect this aspect to the increase in flood occurrence, since it may represent a serious risk for exposed population. Furthermore, while precipitation increase due to global warming is a widely studied issue, quantifying the related changes in flood risk is still an unexplored aspect. Indeed, flood risk also depends on soil type and use, hence it is more difficult to isolate the effect of the increase in extreme precipitation on flood occurrence. The study is conducted for the entire United States and, connecting the outcomes of a climate model ensemble with a hydrodynamic flood model, evaluates the effects of some projected rainfall scenarios on flood risk, also quantifying the number of exposed people. The ensemble of precipitation data used in this study includes a pre-industrial condition, where anthropogenic climate change is not considered, some replications of the 20<sup>th</sup> century precipitation condition (i.e., the historical scenario), including the after-industrial condition and, lastly, two climatic projections extended until the end of the 21<sup>st</sup> century. These latter cases consist of some replications defined at a medium (i.e., medium warming scenario) and a high (i.e., high warming scenario) rate of greenhouse gases emission scenarios (RCP8.5), with the aim to explore the relationship between precipitation extremes and flood risk increase and global warming.

In Figure 12, taken from Swain, *et al.* [56], the change in frequency and magnitude of 100-year return level daily precipitation among all the selected scenarios respect to the historical one is presented. The changes in precipitation

magnitude are evaluated as the difference between the precipitation value under each global warming scenario, at a fixed duration (1 day in the case of Figure 12) and return period (100 years in the case of Figure 12), and the one related to the historical scenario. The changes in precipitation frequency, instead, are assessed by means of a peak over threshold approach, where the threshold is the value at the historical scenario. The frequency represents the number of times the simulated precipitation at each scenario exceeds the one of the historical condition over the number of replications. Figure 12 highlights that, moving from the pre-industrial towards the high warming scenario, there is a clear increase of changes both in terms of frequency and magnitude of 100-year return level daily precipitation. In particular, the changes in frequency reach about 300 % in the West and East of the United States in the high warming scenario, while those in magnitude reach at maximum about 30 % in the south-west coast of the country, always in this climate condition. The most worrying thing is that, with reference to the medium and high warming scenarios, only positive changes in terms of frequency and magnitude of 100-year return level daily precipitation are recorded. This means that anthropogenic global warming would cause an increase of extreme precipitation events, both in terms of their magnitude and frequency of occurrence.

The different precipitation scenarios have been used to force the hydrodynamic flood model, resulting in different flood hazard maps. These latter, along with the vulnerability map for the United States, allowed to obtain

the spatial distribution of the change in the number of exposed people to flood risk at this selected return period. This variation has been computed by comparing the number of people living within the 100-year floodplain area at two different scenarios. It is easy to imagine that, as the precipitation magnitude and frequency increases, the extent of the corresponding floodplain area increases as well. Basing on the 100-year return level daily precipitation showed in Figure 12, the authors evaluated a general growth of the number of exposed people to flood risk across all the United States, which becomes more relevant moving towards the high warming scenario. The highest increase of the number of people exposed to this risk is obtained in many states of the Eastern and western coast of the country, where the greatest precipitation change, along with the greatest number of living people, is recorded.

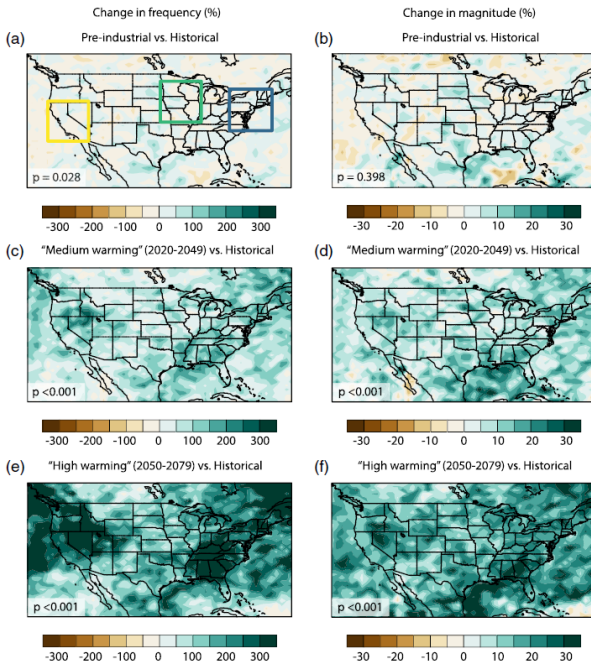


Figure 12 – Changes in frequency and magnitude of 100-year return level daily precipitation in a-b) pre-industrial, c-d) medium warming and e-f) high warming respect to the historical condition. The figure is extracted from Swain, et al. [56].

Since, as affirmed above, climate change has been leading to the increase of the frequency of occurrence and magnitude of extreme precipitation, it is very important to select the proper method to carry out a reliable statistical analysis of extremes. According to Tabari [51], two main methods are currently more used for the statistical inference

of extremes: the block maxima and the peak-over-threshold. This study highlights the importance of choosing the most suitable among these two methods in the context of future projections of climate change at the global scale. In this paper, a comparative analysis between the two methodologies in the evaluation of the increase of extreme precipitation and floods under the RCP8.5 is provided. The changes in extreme precipitation characteristics are evaluated by means of 24 Coupled Model Intercomparison Project Phase 5 (CMIP5) General Circulation Models (GCMs) that are based on the high greenhouse gases emission scenarios for the future projection related to the period 2070-2099. A comparison with a historical period ranging from 1971 to 2000 is also assessed. The advantages and drawbacks of both procedures are thus explored. Indeed, while the block maxima method takes only the maximum precipitation value for each year, the peak-over-threshold provides all the precipitation values above a selected threshold, thus setting up a larger dataset than the block maxima. The main drawback of the block maxima is that some precipitation values that are lower than the maximum of the same year but, at the same time, exceed the maxima of other years are not considered in the dataset. The peak-over-threshold, instead, would consider these data, but is characterized by the complexity in defining the more suitable threshold level.

The extreme value analysis through the block maxima method consists of extracting the annual maxima precipitation value for each year and grid cell for the historical period and the future projection. After that, the

annual maxima are fitted with a Generalized Extreme Value (GEV) distribution function and their return period is computed. The peak-over-threshold, instead, is used to extract, for each year and grid cell, all the precipitation values exceeding the threshold, so that the average number of peaks per year is greater than 1.65. The corresponding return period is assessed by means of the Generalized Pareto Distribution (GPD). For each return period between 1 and 50 years, changes in extreme precipitation intensity are defined as the ratio between the corresponding precipitation related to the future projection and the one for the historical period, for both the block maxima and the peak-over-threshold procedures.

Comparing results obtained through the two methods, the authors highlights that the changes in precipitation intensity are almost the same at low return periods and tend to differ increasingly as the return period increases. In particular, the block maxima method always provides an overestimation of changes respect to the peak-over-threshold. It is hence possible to affirm that the two methods diverge in terms of magnitude, but both agree about the positive change of precipitation intensity, meaning that future projections present more intense precipitation than the historical period, due to global warming. As an explicative case, Figure 13, taken from Tabari [51], shows the changes in the 25-year return period precipitation intensity at the global scale, derived with the two methods. It is highlighted that changes in precipitation intensity are, more or less worldwide, positive. The 25-year precipitation intensity, therefore, is expected to increase by

20-40 % for the greatest part of the world under both the two methods. The main differences can be noticed in Africa and Australia, where the peak-over-threshold assesses much lower (somewhere negative) changes respect to the block maxima. This inevitably affects floods occurrence and intensity; indeed, its global pattern is more or less the same of the one related to precipitation, showing an increase in floods intensity in future projection respect to historical condition. This happens since the same soil type and land use are used under the precipitation forces shown in Figure 13, in such a way to isolate the effects of precipitation increase on floods.

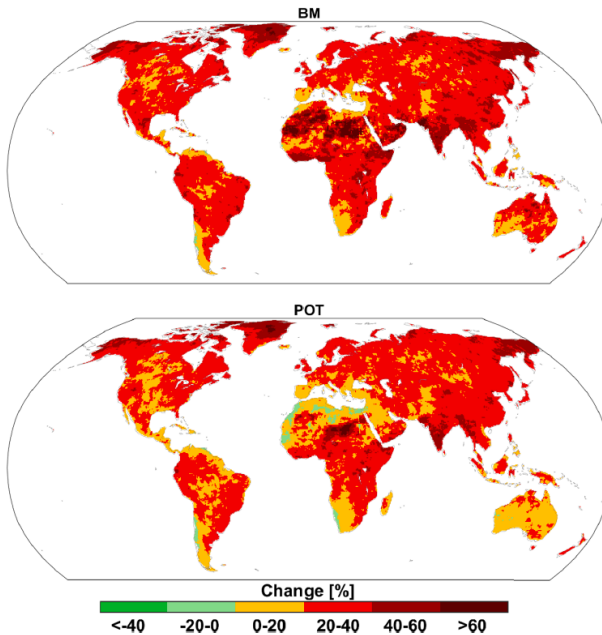


Figure 13 – Changes of 25-year return period precipitation intensity at the global scale, derived by means of the block maxima (upper panel) and the peak-over-threshold (lower panel) methods. The figure is taken from Tabari [51].

## 1.4 Influence of climate change on wildfires

Analyzing the effects of climate change on wildfires occurrence is not an easy task since fire regimes are influenced by many ecological and human-induced factors,

such as land cover changes (i.e., deforestation or particular agricultural practices), lightning activity and population expansion, especially within the areas characterized by a high risk of wildfires occurrence. However, studying the effects of anthropogenic climate change on wildfires occurrence is very important since uncontrolled fires, depending on the extension of the affected area, can cause human fatalities, degradation of natural resources and various economic damages, even to cities and infrastructure [78]. Another serious effect of wildfires is connected to the consequent release of greenhouse gases in the atmosphere, especially CO<sub>2</sub>, CO and CH<sub>4</sub>, due to the fuel (i.e., vegetation and organic soil) combustion.

There are several aspects connected to climate change that could potentially affect the occurrence of wildfires. Among these it is possible to recognize the increase of the global surface temperature, the frequency and intensity of heatwaves, and also of drought periods. Indeed, Jia, *et al.* [2] affirms that drought is the main driver of fire emissions and that warmer temperatures increase vegetation flammability. This is also confirmed by Loehman [61] that analyzed the role of different drivers in wildfires and related carbon emissions. In this study, the authors focus on the boreal region of North America since it has experiencing a faster increase of surface temperature, respect to the rest of the world and, therefore, more severe fires. It is here highlighted that the fuel availability and composition is one of the main drivers of wildfires occurrence and severity, evaluated in terms of vegetation loss and carbon release. In this context, climate change

plays a relevant role since it is responsible of changes in fuel structure and availability, such as tree mortality caused by long periods of drought, that inevitably increase fuel flammability.

Many other studies have been conducted at the local or global scale to understand how wildfire regimes have been changing over the last decades and what is the actual role of anthropogenic climate change. For instance, Abatzoglou and Williams [58] tried to quantify the contribution of anthropogenic climate change to the increase of wildfires activity in the forests of the western Unites States, with reference to the period 2000-2015. The authors calculated eight indices representative of fuel aridity. Some of them, such as the potential evapotranspiration ( $ET_0$ ), the Vapor Pressure Deficit (VPD), the Climatic Water Deficit (CWD), and the Palmer Drought Severity Index (PDSI) are representative of the climatic condition, while others, such as the Fire Weather Index (FWI), the Energy Release Component (ERC), the McArthur Forest Fire Danger Index (FFDI) and the Keetch-Bryam Drought Index (KBDI) are some fire danger indices, indicating the vulnerability of the area to fires. The influence of anthropogenic climate change to wildfires has been evaluated basing on climate predictions from 27 CMIP5 GCMs forced with the RCP8.5 emission scenario for the future projection (i.e., 2006-2099) and considering the historical scenario related to the period 1850-2005. The anthropogenic climate change signal on some representative climatic variables, such as the minimum and the maximum temperature and the water vapor pressure, has been extracted through a low-pass-filter

technique on the time-series of the considered variables. In particular, this technique consists of averaging the annual anomalies of each climatic variable calculated by each GCM under the RCP8.5 scenario respect to the historical period. The anthropogenic climate change signal on the fuel aridity indices has been defined by making the difference between these indices calculated with the temperature and water vapor pressure coming out from the GCMs and those defined once this signal is subtracted.

The change in each of the fuel aridity indices due to anthropogenic climate change related to the period 2000-2015 is shown in Figure 14, taken from Abatzoglou and Williams [58]. GCMs reveal that global warming has led to the increase of temperature and water vapor pressure deficit. This reflects in an increase of all fuel aridity metrics, as it is possible to see from Figure 14, for the period 2000-2015. The authors reveal that there is a positive correlation between the forest fire area and the fuel aridity for the area under study meaning that, as fuel aridity metrics increase, there is a consequent growth of the potentially burned area that involve forests. Translating the changes in fuel aridity into forests loss, the study reveals that, between 1984 and 2015, the anthropogenic climate change has caused the loss of 4.2 million of hectares of forested areas in the western United States. This is raised as a serious effect of climate change that could potentially increase in magnitude if no limiting actions are taken.

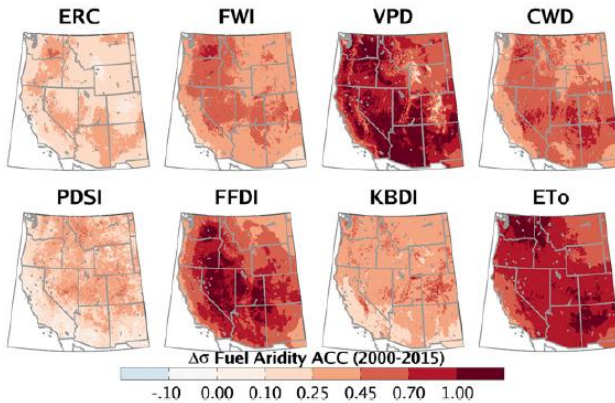


Figure 14 – Changes in each of the eight fuel aridity indices caused by anthropogenic climate change related to the period 2000-2015.

Stambaugh, *et al.* [59] is a further demonstration of the effects of climate change projections on fire regimes at the local scale. The study focuses on the southcentral United States, involving the States of Oklahoma, Texas and New Mexico. The authors tried to extract the fire probability associated with future projections of climate change by means of the Physical Chemistry Fire Frequency Model (PC2FM). This latter is a complex model that defines the spatially distributed fire probability on the base of some climatic data, i.e., temperature and rainfall, and other parameters connected to fire regimes, such as fuel availability and local moisture. The model was forced with climate data obtained from three Atmosphere-Ocean GCMs (AOGCMs), i.e., the CGCM3T47, the HADCM3 and the GFDL, considering a future mid-emission of

greenhouse gases scenario. For each GCM, a spatial distribution of the 30-year average Mean Maximum Temperature (MMT) and the Mean Annual Precipitation (MAP) was obtained. These maps were calculated for three different time windows; i.e., the baseline that considers data from 1900 to 1929, the mid-twenty-first century that goes from 2040 to 2069 and, lastly, the end-of-century period that is the 2070-2099 one. By comparing the outcoming spatial distribution of MMT and MAP obtained through the three AOGCMs, the authors found a general increase of MMT and decrease of MAP within the mid-twenty-first century and the end-of-century periods respect to the baseline condition, at almost all the areas under study. This means that climate change is expected to lead to hotter and drier conditions, which are certainly triggering factors for wildfires occurrence.

The fire probability was calculated as the inverse of the mean fire occurrence, that is defined by the PC2FM model as a function of precipitation, temperature and fuel availability. A spatial distribution of the percent change of fire probability respect to the baseline condition for the area under study is shown in Figure 15, taken from Stambaugh, *et al.* [59]. It is here interesting to observe that results from the CGCM3T47 are not in agreement with those obtained with the other two AOGCMs. Indeed, while this latter shows a general increase of the future fire probability, both in the mid-twenty-first century and the end-of-century periods respect to baseline, the HADCM3 and the GFLD derived a net difference between the Western (i.e., negative changes) and Eastern (i.e., positive changes) sides of the

analyzed area. The areas characterized by negative changes, thus by a reduction in terms of fire probability, are defined as “reactant-limited ecosystems”, while those highlighting positive changes are “reaction-limited ecosystems”. The former represents a condition in which fuel availability is a limiting factor and, therefore, the decrease in fire frequency is due to desertification. The “reaction-limited ecosystems”, instead, are those areas that are not affected by desertification and, at the same time, are characterized by an increase in MMT and a MAP reduction, which inevitably contribute to increase fire frequency.

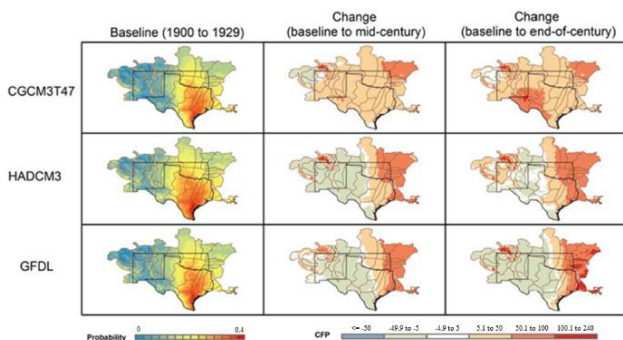


Figure 15 – Projections in change of fire probability obtained through the three AOGCMs respect to the baseline period (i.e., 1900-1929). The figure is taken from Stambaugh, *et al.* [59].

A global spatial distribution of the fire season length and wildfire frequency under two different climate scenarios has been obtained by Sun, *et al.* [79]. The authors affirm that the risk of wildfires strongly depends on

heatwaves and drought periods that, consequently to global warming, are tending to more frequently occur nowadays. In this study, global warming impacts are evaluated under the 1.5 °C and 2 °C targets of the Paris Agreement, with the aim to explore the wildfires risk worldwide and, eventually to encourage policy makers to take decisions allowing a significant mitigation of this effect of climate change. Five GCMs from the Inter-Sectoral Impact Model Intercomparison Project (ISI-MIP) have been used to extract climate projections under the 1.5 °C and 2 °C above pre-industrial level scenarios. A 20-year time window, from 1981 to 2000, was taken as reference for historical simulation, while a future climate change projection, under the RCP 8.5, is related to the 20-year time period from 2080 to 2099. The wildfire risk has been assessed on the base of a wildfire danger index, i.e., the McArthur Forest Fire Danger Index (FFDI), and an exposure index. The FFDI defines the danger of wildfires occurrence as a function of relative humidity, air and soil surface temperature, annual precipitation deficit respect to the mean and wind speed. The exposure index, instead, was defined basing on some socio-economic indicators, such as the population growth and the development of infrastructures.

Figure 16 (from Sun, *et al.* [79]) shows the global spatial distribution of changes of wildfire season length and frequency under the 1.5 °C, 2 °C and the 2080-2099 future projection respect to the historical condition. It is noteworthy that both wildfires season length and frequency are expected to increase under the three global warming levels, as compared to the historical period. In particular,

the greatest increase of fire season length, under the 1.5 °C warming scenario, was obtained for South America, the west side of United States, Africa, Central Asia and Australia. The same areas are expected to run into a longer fire season length under the 2 °C warming scenario. The 2080-2099 projection, instead, shows a significantly high increase of fire season length all over the world which is noticeably relevant at the above-mentioned areas, where it reaches almost 50 days. With reference to the wildfire frequency, it is expected to increase respect to the historical condition in the western United States, Argentina, Australia and Russia, especially under the 2080-2099 scenario, while a decrease has been assessed at Central Africa, the rest of United States, Russia and Southern Asia. Putting together these results, the authors derived that about 75 % of land area would experience a relevant increase in wildfires risk, highlighting that even the 1.5 °C above pre-industrial levels warming target of the Paris Agreement could not be enough to avoid, or at least mitigate, the major effects of climate change in the context of wildfires occurrence and forest loss.

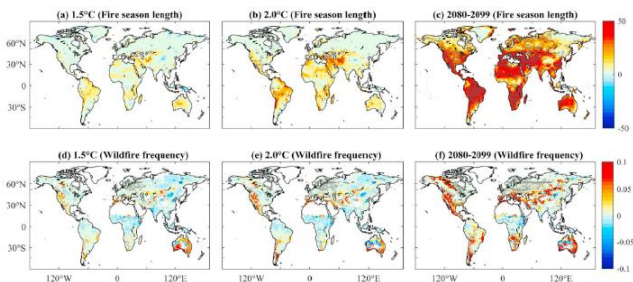


Figure 16 – Global spatial distribution of changes in wildfires season length and frequency under the (a) 1.5 °C scenario, (b) 2 °C scenario and (c) 2080-2099 future projection, respect to the historical condition (i.e., 1981-2000). The figure is taken from Sun, et al. [79].

## 1.5 Climate change effects on food security

A serious climate change impact that could probably regard the world population in the next future is related to food production. Leisner [65] presented a review on recent works about how the effects of spatial and temporal changes of climatic variables, i.e., temperature and precipitation patterns, may affect future food production. This aspect is analyzed in the context of the growth of the world population, which is set to reach 9.1 billion by 2050. One of the most important aspects here described is related to the maintenance of crop nutritional values, apart from the need of increasing crop production and yields, in order to meet the needs of a growing population. For instance, the authors affirm that, despite the increase of atmospheric CO<sub>2</sub>

concentration could result in an increase of the leaf photosynthesis of some crops (CO<sub>2</sub> fertilization phenomenon), such as soybean, wheat and rice, and hence on their yield, the same could lead to a reduction of nutrients and proteins in these crops, resulting in an inefficient growth of food production. To this regard, the study highlights that in the future diverse food sources could be used, in order to overcome the possible future lack of nutrients of common crops. An in-depth analysis of how much future projections of climate change may affect food production and its nutritional quality is nowadays a very important, even though not easy, challenge. Indeed, this requires a multifaceted approach that is able to put together different disciplines, such as plant physiology, genomics and the modeling of future climate scenarios.

Ortiz-Bobea, *et al.* [62] analyzed the impacts of the historical anthropogenic climate change on agricultural productivity at the global scale, with reference to the period 1961-2015. To this purpose, the authors analyzed a dataset of the Total Factor Productivity (TFP) provided by the United States Department of Agriculture (USDA) and involving 172 countries all over the world. This index allows to take into account different factors, in response to a variation in the output yield of a certain crop. In particular, apart from changes in weather regimes, also agricultural technologies and practices are considered. In order to isolate the effects of climate change, the authors carried out a regressive analysis of TPF dataset at a country level, thus excluding any TPF change due to other factors, which are more connected to the economy of the country.

The authors used the Global Meteorological Forcing Dataset of the minimum and maximum temperature and total precipitation for the period under study. Seven GCMs were also used to define the contribution of anthropogenic climate change to temperature rise and total precipitation decrease. The effect of anthropogenic climate change was assessed by subtracting TPF changes evaluated through a quadratic regression on temperature and precipitation data without anthropogenic climate change for a certain GCM from those related to the same GCM considering the anthropogenic greenhouse gases emissions. The analyses have been carried out for a 5-month period for each year, centered within the month characterized by the greatest NDVI, to consider the vegetation growing season. The statistical uncertainty of TPF changes has been computed through a bootstrap method, for each year and each country under study. The study highlights a strong linear relationship between TPF change and temperature, representative of a more significant TPF decrease in warmer countries. Regarding precipitation, instead, there is an almost quadratic function, characterized by a peak at around 500 mm. In Figure 17 (from Ortiz-Bobea, *et al.* [62]) the spatial distribution of the global TPF changes due to anthropogenic climate change, evaluated at a country-level, is reported. Panel (a) of this figure also provides the mean change of TPF and the corresponding confidence intervals at different significancy levels for different areas of the world. The global mean behavior is also reported in red. Panel (b), instead, represents the average TPF changes for each country. It is here possible to notice that

anthropogenic climate change in the period 1961-2015 has contributed to the TPF reduction for almost all the world. The more significant impacts involve the warmer countries, such as Africa and South America, even though a not negligible agricultural productivity reduction is recorded for colder areas. The global average TPF reduction is about 21% which is equivalent, according to the study, to the loss of seven years of crop productivity. This certainly represents a serious damage especially for those countries (i.e., Africa) where agriculture is the sector that employ most of the people and, unfortunately, it is expected to increase with future climate projections.



Figure 17 – TPF changes due to anthropogenic climate change for (a) some areas of the world with the corresponding 95%, 90% and 80% confidence intervals and (b) average TPF change at the global scale. The figure is taken from Ortiz-Bobea, *et al.* [62].

The loss of agricultural productivity inevitably affects people health status. One of its important consequences regards global hunger, which is particularly relevant in poor countries. Janssens, *et al.* [63] presented a study regarding the global population exposed to the risk of hunger in 2050 under different climate and international trade scenarios.

Indeed, the authors affirm that modifying international trade policies, that connect poor and rich countries, could be an important strategy to deal with the loss of food production due to global warming. The study tries to explore different trade adaptation mechanisms to more efficiently perform food exchanges between different countries under various greenhouse gases emissions scenarios. Global climate change and hunger projections to 2050 are defined on the base of some climate and economic models. In particular, climate projections were defined on the base of different climate models, considering various greenhouse gases emissions scenarios, ranging from RCP 2.6 (i.e., global temperature increase by 2 °C above pre-industrial levels) to RCP 8.5 (i.e., global temperature increase by 2.6-4.8 °C above pre-industrial levels). The worst climate change condition is the RCP 8.5 without the fertilizing CO<sub>2</sub> effect, that increases plant productivity, as described above. For all the considered climate scenarios, the population exposed at hunger risk has been assessed at different international trade policies. This latter is defined as a function of crop yield, which depends on climate change, and trade costs. In Figure 18, taken from Janssens, *et al.* [63], the global population exposed at hunger risk, under the different analyzed climate change and international trade scenarios, is presented. The figure also shows a dotted line, which represents the baseline scenario, where current baseline trade costs and climate conditions are considered. It is noteworthy that, whatever the trade costs scenario, climate change has a negative contribution on the global population affected by risk of hunger, that

become even worse moving from RCP 2.6 to RCP 8.5, namely as the global temperature rise is higher. The international trade costs can be an optimal adaptation strategy to climate change since they may help to reduce the gap, in terms of food availability, between poor and rich countries. The most suitable strategy seems to be the one that combines facilitation and tariff elimination, that consists of eliminating agricultural tariffs and infrastructure costs, involving logistic, that are higher in developed countries. In any case, the study aims to highlight the negative impact of a severe global warming scenario since, modifying the international trade policies to facilitate poor countries, is just an adaptation strategy, that could be avoided if measures to mitigate climate change will be applied in the near future.

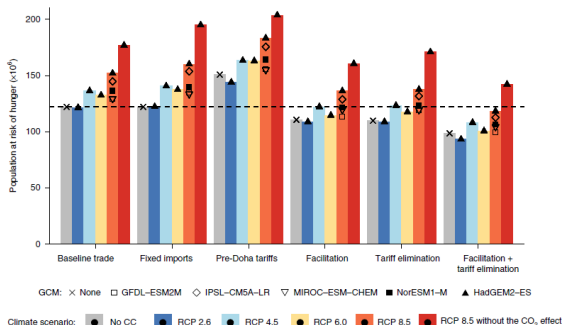


Figure 18 – Total population that is exposed at risk of hunger globally evaluated under different climate change and international trades conditions. The dotted line represents the baseline condition in terms of trade costs and climate change. The figure is taken from Janssens, et al. [63].

## Chapter 2 - Climate change adaptation strategies

Basing on the greenhouse gases emissions given by anthropogenic activities over the last decades, causing global warming with all the above-mentioned impacts, in 2016, 196 state parties all over the world signed the Paris Agreement on climate change. The main scope of the Agreement is to face climate change, in such a way not to run into severe climate projections and damages in the future (as many times mentioned in Chapter 1). In particular, the main collective goal is to hold global temperature rise below 2 degrees, with a particular effort to limit it to 1.5 degrees above pre-industrial levels by 2030 [6]. This would lead to significantly reduce risks and impacts of climate change. Furthermore, other aims of the Agreement consist of improving the ability of the population to deal with climate change impacts (i.e., climate resilience) and to provide a constant and relevant support to underdeveloped and developing countries. This global warming goal was already previously suggested by the United Nations Framework Convention on Climate Change in Copenhagen in 2009, where the 2-degrees goal was defined as a tolerable threshold to avoid the most catastrophic consequences.

Some studies [7,8] affirm that, despite the most straightforward way to respect the Paris Agreement goal is to reduce greenhouse gases emissions (i.e., by reducing the

use of fossil fuels), this could not be enough. In addition, this is not an easy task to achieve since it would mean to radically change the habits of the worldwide population. The most recent and explicative example of carbon emissions reduction has been given by the COVID-19 pandemic, particularly during the most restrictive lockdowns. It is clear that, a global pandemic that has caused more than 5 million deaths in the world so far is the worst way to reduce greenhouse gases emissions, but it is equally true that, during the global forced confinement, in the first months of 2020, daily global CO<sub>2</sub> emissions has reduced by 17%, as compared to the average 2019 values. This effect was particularly significant in the most developed countries, such as China and the United States, and was mainly due to the significant reduction in industry, surface transport and aviation sectors [80,81]. Other estimates of greenhouse gases and air pollutant reductions in the period February-June 2020 are provided by Forster, *et al.* [82], that also provides the consequent effects in terms of the response of global temperature in the future. The analyses presented in this study have been carried out by means of Google and Apple mobility data, which allowed to reconstruct the effects of restrictions in global mobility on greenhouse gases emissions and to identify the contribution of the industrial and commercial sectors. A comparison with the data of Le Quéré, *et al.* [80] and Liu, *et al.* [83], with the aim to provide a more reliable estimation of COVID-19 effects, is also presented. Once found a good match between the different datasets, the authors extended the analysis of Le Quéré, *et al.* [80] from

69 to 123 countries of the world. In Figure 19, taken from Forster, *et al.* [82], a comparison of the daily global CO<sub>2</sub> emissions changes, respect to the 2019 average values, caused by global restrictions during April 2020 in various sectors is provided. It is here possible to notice that restrictions in surface transport have resulted in the greatest percentage of emissions reductions, as compared to other sectors. The residential one, instead, resulted in slight CO<sub>2</sub> emissions increase, due to persistent lockdowns.

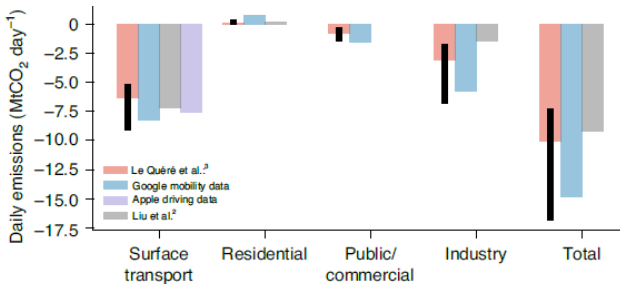


Figure 19 – Global daily CO<sub>2</sub> emissions changes in April 2020, as compared to the 2019 average values, due to global restrictions in different sectors. The figure is taken from Forster, *et al.* [82].

Analyses regarding different greenhouse gases in the period February-June 2020 revealed that, COVID-19 restrictions caused about a 35%-reduction of NO<sub>x</sub> and a 30%-reduction of CO<sub>2</sub> emissions, as compared to a baseline condition, where countries meet their climate mitigation actions defined in the Paris Agreement by 2030 without any other significant action for mitigating climate change. To

see if these emissions reductions due to COVID-19 pandemic may lead to a relevant effect in limiting the global temperature rise, the authors assessed the surface temperature response, considering that the 66% of the emission decrease of April 2020 are projected to be maintained until the end of 2021. The authors found that only for a couple of years after the end of restrictions there could be a decrease of surface temperature, called “cooling effect”, that is however very small (i.e., about 0.015 °C), as compared to the baseline condition. After that, global warming will carry on at previous rates. This could be due to the long residence times of greenhouse gases, and particularly of CO<sub>2</sub>, in the atmosphere. Scientists therefore came out with the consideration that, the damages produced by the COVID-19 pandemic has not led to any benefit in facing climate change. This study, therefore, aims to encourage international policies towards investments in renewable technologies rather than the use of fossil fuels or in adopting strategies to reduce the current greenhouse gases concentration in the atmosphere.

A distinction of different global warming mitigation strategies has been provided by Hartmann, *et al.* [15], that distinguish between Carbon Dioxide Removal (CDR) and Solar Radiation Management (SRM) techniques. Technologies belonging to the first category consist of reducing the atmospheric CO<sub>2</sub> concentration by removing the carbon within it and, for this reason, they are well known as “carbon sequestration” techniques. Those that are part of the SRM, instead, aim to reduce the global average temperature by modifying the Earth’s energy balance,

reducing the extraterrestrial solar radiation being absorbed by the planet. The most known examples of CDR techniques are based on the “geoengineering” discipline since they involve processes at the scale of the Earth. Among these, it is possible to mention afforestation, ocean liming, direct air capture and enhanced weathering. Among SRM technologies, instead, there are cloud brightening, stratospheric aerosols, roof whitening and mirrors in space [84]. Some of the CDR techniques, such as afforestation and enhanced weathering are considered as NCS since they aim to sequester carbon by means of naturally occurring processes which, in turn, can be enhanced [85]. In this chapter, a comprehensive view of some CDR and SRM techniques is provided, describing their capabilities to face climate change and also their potential effects on ecosystems.

## 2.1 The SRM techniques

The SRM technologies goal is to reflect a percentage of the incoming solar radiation back to the space and, thus, reducing the increasing rate of the global average temperature, due to the presence of greenhouse gases in the atmosphere. Russell, *et al.* [12] affirms that these techniques provide an immediate cooling (after only few months the intervention), but require a constant maintenance in order to avoid that the greenhouse gases excess in the atmosphere cause an immediate temperature increase.

Figure 20, taken from NOAA, shows the mostly known SRM techniques in scientific literature and their level of application in the atmosphere. These methods could consist of increasing the reflectivity of the Earth surface by, for instance, enhancing the amount of white surfaces, or putting highly reflective materials in the desert. Another method could provide the enhancement of marine cloud reflectivity, through the growth of the amount of particles acting as cloud condensation nuclei over the oceans. Then, there could be the possibility of injecting aerosol particles into the stratosphere, that lead to increase the reflectivity of that layer of the atmosphere. Lastly, some studies suggested the idea of putting shields or mirrors in space, with the aim to decrease the amount of solar energy that reaches the Earth.

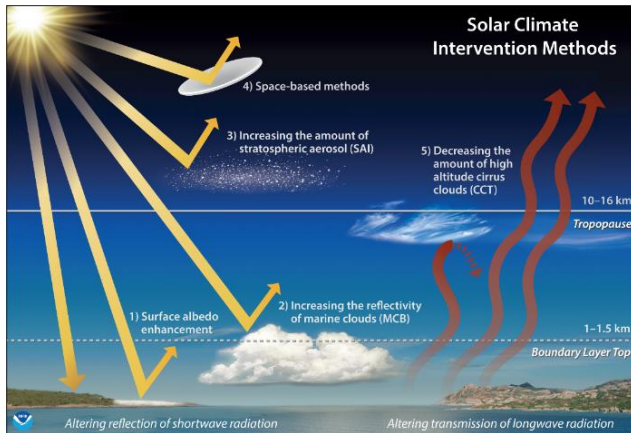


Figure 20 – Solar radiation management strategies to face global warming and their level of application in the atmosphere. The figure is taken from NOAA.

The benefits and drawbacks of SRM technologies are different and may essentially consist of changes in temperature and precipitation patterns, even in the long term, and of the fact that greenhouse gases concentrations remain unchanged. Their effects, in fact, mainly depend on the adopted technology and, for this reason, a more in-depth analysis of the most relevant ones is needed. Among all these possible SRM technologies, the following sections provide a description of some studies about the increase of terrestrial surface albedo, the stratospheric aerosol injection and the increase of marine cloud brightening, describing their possible impacts on climate change and eventual benefits/drawbacks on Earth's ecosystems.

### 2.1.1 The terrestrial albedo increase

The main goal of this technology is to reduce the adsorption of incoming shortwave solar radiation and, at the same time, to increase the amount of this energy that is reflected by the Earth surface and sent back to the space, leading to the reduction of the global temperature rise. This may involve increasing the reflectivity of the Earth's surface, including vegetated areas, oceans and urban environments. One of the most important issue for this technology is the capability of efficiently detecting albedo changes, in order to see if it is effective in the change of the Earth's energy balance and, furthermore, its potential effects on temperature and precipitation patterns.

To this regard, Seidel, *et al.* [9] based the detection of albedo changes through a balance of incoming and outgoing shortwave radiation at the global scale. The authors affirm that detecting albedo changes is not trivial and it is rather difficult to isolate its effects on the planetary energy balance. Indeed, some regions characterized by albedo increases may be hidden or counterpoised by other areas where there has been an albedo decrease. Another issue could be connected to the fact that the intervention could not lead to immediate changes in energy balance, hence it is not detectable. Other SRM technologies, such as aerosol injection in the stratosphere could lead to a sudden and significant albedo increase that may mask the albedo increase due to some specific interventions in the Earth's surface. The authors proposed an approach to detect the

maximum and minimum albedo changes for a hypothetical SRM intervention at the global scale, also analyzing some specific cases at a regional scale. They used satellite data of incoming and outgoing shortwave solar radiation from the Clouds and Earth's Radiant Energy System (CERES) Energy Balanced and Filled (EBAF) dataset provided by the NASA. Albedo data for the period 2000-2012 have also been extracted from this solar radiation dataset. By analyzing these data, the authors assessed which part of the planet could be more suitable to adopt this SRM intervention. They found that the highest albedo variability is recorded at high latitudes, where there is a great seasonal albedo change due to variations in snow and ice cover, and at the tropical Pacific and Indian Oceans, due to the greatest variability of cloud cover. Since these signals may mask or excessively enhance albedo increases of an SRM intervention in the ground, the authors states that those areas characterized by low averages and interannual albedo variability, such as Africa, the northern part of South America and Australia, are the most suitable to adopt this technology, for instance by enhancing the reflectivity of grasslands.

Since oceans occupy the greatest part of the planet area, Crook, *et al.* [86] focuses their attention of increasing reflectivity of their surface, rather than planning intervention involving land areas. In this study, the change of global surface temperature and precipitation due to an albedo increase of existing ship wakes is assessed. In general, the presence of a high number of microbubbles in the atmospheric layer few meters above the ocean surface,

helps increasing albedo. Ship wakes generate bubbles that, unfortunately, have a short lifetime (i.e., some minutes). For this reason, the study aims to explore the possibility of increasing the lifetime of already existing ship wakes bubbles, in order to increase albedo of the oceans' surface, so as to have a global response to climate change. The authors evaluated the instantaneous shortwave radiative forcing as a function of ship wake albedo and the near surface lifetime of bubbles, that is related to those bubbles located in few meters above the sea surface. Datasets of international ship transport have been employed to define the spatial distribution of ships location any time. Then, the fraction of each grid cell covered by ship wakes has been obtained on the base of the number of ships in each cell and the typical area of a ship wake. The shortwave radiative forcing, instead, is expressed on the base of the near surface lifetime of bubbles and the albedo increase given by the presence of the ship wakes respect to the oceans albedo, that is about 0.05. The input of shortwave radiative forcing has been defined by means of the HadGEM2-CCS GCM, provided by the UK Met Office, under the RCP 4.5 emissions scenario. Figure 21, extracted from Crook, *et al.* [86], represents how the shortwave radiative forcing varies depending on the increase of the near surface lifetime of bubbles and under different albedo changes, due to the longer lifetimes of bubbles. It is here possible to see that there is a non-linear relationship between the change of the shortwave radiative forcing and the bubbles lifetime increase. A near surface lifetime increase factor of 1440 is estimated to stand for an increase in bubbles lifetimes of

about 10 days, starting from a basic lifetime of some minutes. This would result in a reduction of the shortwave radiative forcing of about  $0.9 \text{ W m}^{-2}$ , corresponding to a reduction of the global mean surface temperature of about  $0.5 \text{ }^{\circ}\text{C}$ . If the near surface lifetime increase factor reached about 8000, this would require an increase of bubbles lifetime of about 3 months, corresponding to a reduction of the shortwave radiative forcing of about  $3 \text{ W m}^{-2}$  and a cooling rate of  $1.5 \text{ }^{\circ}\text{C}$ . Such increases of bubbles lifetime would require the addition of surfactant to ship lanes, since they allow to stabilize microbubbles, thus enhancing their residence time in the sub-surface layer of the atmosphere.

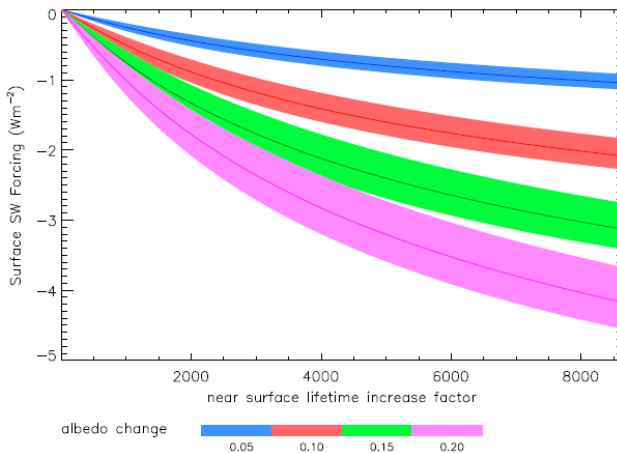


Figure 21 – Changes in surface shortwave radiative forcing vs the increase of the near surface lifetimes of ship wakes bubbles under different albedo changes. The shaded areas represent the uncertainty thresholds

*basing on a certain range of the number of transiting ships. The figure is taken from Crook, et al. [86].*

The increase of surface reflectivity on urban environments is also considered a powerful method to face the global temperature rise, if extensively applied. To this regard, Jandaghian and Akbari [87] tried to understand if increasing urban albedo, for example by using highly reflective materials on roofs and streets, may help reducing urban temperature and air pollutions. Their study focuses on three highly populated cities in the United States, i.e., Sacramento, Houston and Chicago. The authors coupled the online Weather Research and Forecasting model with Chemistry (WRF-Chem) with the Multi-Layer of the Urban Canopy Model (ML-UCL). Apart from 2-m air temperature, these models allowed to see the effects of urban albedo changes in some air quality parameters, such as fine particulate (PM<sub>2.5</sub>), nitrogen dioxide (NO<sub>2</sub>) and ozone (O<sub>3</sub>). Results show that, by increasing albedo of roofs, walls and pavements by 0.4, a significant decrease in air temperature both in urban (i.e., 2.3 °C) and suburban (i.e., 0.7 °C) areas is provided. The effects of enhancing the reflective power of cities also leads to an improvement of air quality, since the authors observed a great reduction of the PM<sub>2.5</sub> and O<sub>3</sub> concentrations in both urban and suburban areas. Therefore, if cities, especially the most populated ones, adopted these strategies of albedo increase, an improvement of the quality of life, apart from the mean surface temperature reduction, would be achieved. If applied at the global scale, this would result in a global

temperature reduction, playing a good contribution in facing global warming.

### 2.1.2 Stratospheric aerosol injection

Stratospheric aerosol injection is one of the most discussed SRM techniques to counteract global warming. Tjiputra, *et al.* [88] affirm that this technology takes inspiration from the natural spread of sulfur gases in the atmosphere from volcanic eruptions, which is a natural phenomenon. Indeed, sulfur gases in the atmosphere are quickly converted into sulfate aerosols that, thanks to the atmospheric circulation, may spread in various areas or at the global scale. Their effect is to reflect part of the shortwave solar radiation back to the space, hence resulting in a fast global temperature reduction. One of the most important aspect, which can determine the feasibility of the intervention, regards the available technologies to spread these aerosols into the stratosphere, their related costs, and also the impacts on precipitation patterns and Earth's ecosystems, which are not well understood nowadays.

Trying addressing this latter issue, Sun, *et al.* [10] carried out an extensive analysis to define the impacts of this technology to global monsoon precipitation. The authors analyzed a 140-year sulfate aerosols injection in the lower stratosphere, considering an amount ranging from 10 to 100 Tg y<sup>-1</sup> since a similar value is spread by large volcano eruptions. Then, they looked at the corresponding effects in terms of global temperature reduction and global

monsoon precipitation changes, also comparing two different strategies, i.e., the Arctic and tropical injections, with a scenario that considers a 1% CO<sub>2</sub> increase per year, which leads to an almost linear increase in the global surface temperature. To evaluate the effects of this SRM technologies, the authors used the Community Earth System Model (CESM), that divides the atmosphere in a number of control volumes, in which the most representative variables are calculated.

Results show that a reduction of the global average surface temperature is achieved, at all the 140 years under study, considering the injection of sulfate aerosols concentration only above 40 Tg y<sup>-1</sup> in the tropics. Regarding the Arctic injection, the authors found that similar results can be achieved only using sulfate aerosols concentration above 80 Tg y<sup>-1</sup>. This means that, tropical injection leads to a greater surface temperature reduction than the Arctic one, given the same concentration of sulfate aerosols. Figure 22, taken from Sun, *et al.* [10], synthetize the mean surface temperature variations across the years 101-140 of the intervention at the global scale. These variations are evaluated respect to the 1% CO<sub>2</sub> increase per year, that causes a global temperature rise respect to the historical condition, given by the pre-industrial era (panel a). Panels b-d of the figure are related to the tropical injection, while panels e-g to Arctic injection. The sulfate aerosols concentrations, that are here considered, are equal to 20, 50 and 80 Tg y<sup>-1</sup>. It is here possible to see that, globally, tropical sulfate aerosol injection has a greater cooling effect than the Arctic one, leading to a global surface

temperature reduction of about 8 °C in some parts of the world, spreading 80 Tg y<sup>-1</sup> of sulfate aerosols in the stratosphere. In general, cooling effect is more highlighted over land areas than oceans and this pattern is reflected under both tropical and Arctic injections and all the different sulfate aerosols concentrations. Lastly, the northern hemisphere seems to be characterized by a stronger cooling effect due to the greater land areas respect to the southern hemisphere.

Regarding changes in monsoon precipitation patterns, a similar representation to Figure 22 shows that, while CO<sub>2</sub> increase scenario leads to a global monsoon precipitation increase (i.e., greater occurrence of extreme events), the greater the sulfate aerosols concentration, the greater the global monsoon precipitation reduction, maintaining the same pattern under both tropical and Arctic injection, even though with slightly smaller values in the case of Arctic one, given the lower cooling effect. In general, under the tropical injection, this reduction is more evident in equatorial areas, where it may reach about -2.5 mm day<sup>-1</sup>; in any case, a global precipitation reduction is recognized globally. The Arctic injection instead, results in some areas of the southern hemisphere which are characterized by a remarkable increase of monsoon precipitation, due to a low temperature change (i.e., white areas of Figure 22). These simulations suggest that, despite stratospheric aerosol injection may be a powerful SRM technology to face global warming, given the significant cooling effects, especially if applied in tropical areas, it leads to changes in global precipitation patterns. Precipitation reduction may be beneficial if

talking about the reduction of extreme events occurrence, but it is surely detrimental if one thinks to aridity and desertification consequences. Many of these aspects are still needed to be extensively explored before applying this technology, in order to avoid catastrophic consequences for the planet.

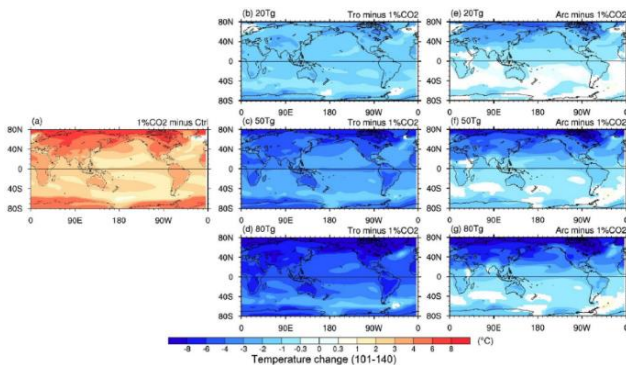


Figure 22 – Mean surface temperature variations evaluated between the years 101-140 of the stratospheric aerosol injection at the global scale. Panel (a) compares the  $\text{CO}_2$  increase scenario with historical condition (i.e., pre-industrial era), panels (b-d) reflects the impact of three different sulfate aerosols concentrations injected in tropical areas, while panels (e-g) are related to the same concentrations at the Arctic. The figure is taken from Sun, et al. [10].

Another important aspect regarding sulfate aerosol injection, that is still not widely explored, is the availability of technologies to deliver sulfate aerosols into the lower stratosphere (i.e., about 20 km of altitude) and related costs [89,90].

With regard to this, Smith and Wagner [90] reviewed all the methods that are currently available to spread a huge amount of  $\text{SO}_2$  (they talk about millions of tons) up to 20 km of the atmosphere, analyzing the feasibility and costs of the intervention. The authors propose an intervention plan consisting of reducing the global average surface temperature of about 0.3 K in 15 years, consisting of halving the impacts of the RCP 6.0 emissions scenario. This would require to release onto the lower stratosphere a total amount of 3 Mt of  $\text{SO}_2$ . The more convenient way is to loft S instead of  $\text{SO}_2$  and to convert S to  $\text{SO}_2$  on board, given that the mass of sulfate to loft exactly corresponds to half of the dispersed mass of  $\text{SO}_2$ . Another relevant aspect is connected to the latitudes where sulfates are spread. According to many studies, as mentioned above, tropical areas are the most suitable ones, since there is a greater cooling effect. Since all existing commercial and military aircrafts are not able to reach the required altitude having such a high payload, the authors proposed a novel aircraft, called Sulfate Aerosols Injection Lofter (SAIL) to fulfill this mission, also providing cost estimates. This system consists of an aircraft that is characterized by larger wings and a more compact fuselage, having four engines instead of two. These characteristics allow to load more weight than usual plains and remain at 20 km of altitude for a great amount of time. The aircraft is also equipped with a combustion system to generate  $\text{SO}_2$  from sulfate. Taking into account all the development and operating costs, the authors come out with a total average cost of about 2.25 billion \$ per year, over the total period of 15 years, with the

aim to provide a global cooling effect of 0.3 K. This total cost is considered cheap if compared to the benefits in terms of facing global warming, since many countries of the world can afford these costs for a global benefit without adversely affecting their economy.

### 2.1.3 Increasing marine cloud brightening

This geoengineering technique consists of enhancing the droplet concentration of the stratocumulus clouds above the sea surface, by means of spreading sub-micrometer sea water particles into the marine boundary layer, that is the layer of the atmosphere where the great part of exchanges of heat and moisture occur. In this way, the effect would be the increase of cloud albedo that enhance the reflected component of incoming solar shortwave radiation back to the space. Therefore, differently from the stratospheric aerosols injection, that may be applied at broad scales, this kind of intervention can involve specific oceanic regions, since it only focuses on clouds close to the sea surface.

Stjern, *et al.* [11] analyzed the impacts, in terms of global average temperature decrease and changes in precipitation patterns, of a marine cloud brightening experiment provided by the Geoengineering Model Intercomparison Project (GeoMIP). The tested experiment is the G4cdnc, which assumes a 50 % increase in the Cloud Droplet Number Concentration (CDNC) of clouds in the marine boundary layer of the oceans at the global scale. The aim of this experiment is to mitigate the effects of the RCP

4.5 emissions scenario, that represents a growth of greenhouse gases emissions at the current rate of increase until 2040. To have an extensive view, nine GCMs of the CMIP5 have been tested and, for each one of them, the differences of global temperature and precipitation patterns under the RCP 4.5 with and without the G4cdnc experiment have been assessed. The effects of cloud brightening have been evaluated for the period 2020-2069, as a hypothetical time window to actually apply the intervention. Each GCM model simulates the total cloud cover and related characteristics in different ways, depending on the atmospheric circulation. This obviously affects the G4cdnc experiment since it focuses on enhancing the reflectivity of marine clouds. For this reason, the median results were considered to be representative of all the GCMs response to the G4cdnc experiment.

Figure 23 displays the difference between G4cdnc and RCP 4.5 scenarios related to the period 2020-2069. Panels represent the median changes of Top Of Atmosphere (TOA) energy flux imbalance (a), of the near-surface temperature (b), of the cloud cover (c) and the total annual precipitation (d). The TOA energy flux imbalance represents the variation in the radiative forcing provided by the increase in the CDNC by 50 %. It is possible to observe that, over the oceans, where cloud brightening should be increased, there is a negative TOA net radiative flux imbalance, meaning that there is an outgoing solar radiation component that is higher under the G4cdnc experiment than the RCP 4.5 scenario. This leads to a cooling effect, as it is possible to observe from panel (b) of the figure, that also

involves land areas due to heat transport from the oceans. The global median change of near-surface temperature reveals a cooling effect more significant at the Arctic. This also involves land areas, especially those at low latitudes, since the cloud cover increase, due to the increase in marine cloud brightening, leads to the albedo increase. The increase of cloud cover is not visible at too high and low latitudes, due to the presence of ice and a stronger temperature reduction. Regarding the impacts on precipitation patterns, it is possible to notice a general reduction of the total annual precipitation at the global scale, which reaches even 20 % over the tropical oceans. This is resulted from the general reduction of global temperature. However, some parts of Africa and Australia show a precipitation increase, which is due to some atmospheric circulation pattern that generates from the near-surface temperature reduction over the oceans that is more significant than over the land areas. It is therefore worth to notice that, despite increasing marine cloud brightening leads to a global cooling effect, it also results in a significant precipitation reduction for the greatest part of the world, which may have catastrophic consequences connected to drought.

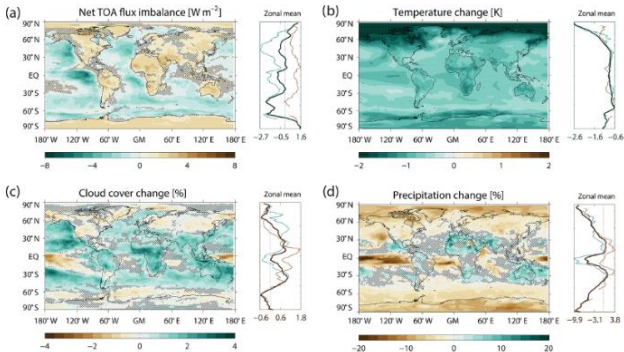


Figure 23 – Median difference between G4cnc and RCP 4.5 scenarios in the period 2020-2069 related to (a) net TOA flux imbalance, (b) near-surface temperature, (c) global cloud cover and (d) total annual precipitation pattern. The zonal means for land (brown lines), ocean (blue lines) and total areas (black lines) are also reported. The figure is taken from Stjern, et al. [11].

An interesting study that compares two different SRM technologies, namely marine cloud brightening and ocean albedo modification, has been conducted by Zhao, et al. [91]. Despite the two techniques have the same scope, i.e., reflecting more incoming shortwave solar radiation only acting on ocean areas, they differ in the mechanism. Indeed, while the marine cloud brightening aims to increase the albedo of clouds situated in the marine boundary layer, the ocean albedo modification consists of increasing the albedo of ocean surface, for example by uniformly dispersing a sort of foam to the ocean surface, composed of microbubbles able to reflect a great quantity of solar radiation. Comparing these two SRM techniques is

important since the albedo change at different heights may lead to different climate responses, in terms of variations of temperature and precipitation patterns.

The authors used the CESM model to carry out a simulation related to the current atmospheric CO<sub>2</sub> concentration (i.e., 400 ppm), a simulation where this concentration is the double of current level (i.e., 800 ppm), a marine cloud brightening scenario, simulating the injection of sea salt and a consequent 3 μm reduction of the cloud water droplet diameter and, lastly, the ocean albedo modification by uniformly increasing by 0.1 the direct and diffuse components of ocean surface albedo, simulating the use of a uniformly distributed foam above the sea surface. The purpose of these two SRM techniques is to offset the 800 ppm atmospheric CO<sub>2</sub> concentration scenario.

With reference to the fast adjustment condition, where climate has not reached the equilibrium yet, the two SRM techniques lead to different responses. Indeed, marine cloud brightening leads to a reduction of the air temperature in the atmospheric layer between the ocean surface and the clouds. This is due to the increased albedo of marine clouds that reduces the amount of shortwave radiation reaching the oceans. Regarding the ocean albedo modification, the short-term effect consists of increasing the air temperature over the oceans due to the fact that the back-scattering of shortwave solar radiation happens only at the sea surface, thus all the tropospheric layers above are reached by this radiation and tend to warm. Despite the two interventions only involve ocean areas, the same effects are obtained for land, due to the atmospheric heat transport between oceans

and land areas. When climate reaches the equilibrium condition, instead, the two techniques results in similar effects. Indeed, the spatial distribution of the surface air temperature reduction at the global scale, produced by the two SRM approaches, is almost the same. This pattern strongly reflects the one achieved by Stjern, *et al.* [11], since a greater cooling is obtained at the Arctic region, due to the polar amplification effect. Analyzing the impacts on global mean precipitation at equilibrium conditions, the authors found out that marine cloud brightening causes a greater cooling effect than ocean albedo modification. However, the spatial distribution of precipitation change reveals that both approaches lead to a precipitation increase at tropical land areas and a reduction over tropical oceans and Arctic areas. A further comparison of the two methods revealed that, to produce the same cooling effect, ocean albedo modification requires a greater amount of effective radiative forcing, which is an indicator of the alteration in the amount of shortwave solar radiation reflected back to the space. This makes this technique less effective than marine cloud brightening.

## 2.2 The CDR techniques

The CDR techniques aim to sequester the carbon contained in the atmospheric CO<sub>2</sub> and store it within oceans, vegetation or other terrestrial environments. According to Russell, *et al.* [12], they have the potential to reduce the greenhouse gases atmospheric concentration and

could lead the climate to a similar pre-industrial condition. These technologies can also reduce ocean acidification, that is defined as “the other CO<sub>2</sub> problem” [92], due to the alteration of biogeochemical cycles in the oceans and consequent damages for the ecosystems. For this reason, they may be preferred to the SRM techniques; however, unlike the latest, they require a longer time to act. Among all the possible alternatives, summarized in Figure 24, it is worth to cite some land use strategies that allow to protect or enhance terrestrial natural carbon sinks (i.e., afforestation), the use of biomass or chemical sorbent materials to capture atmospheric carbon, the direct air capture with consequent CO<sub>2</sub> sequestration and carbon storage, the increase of the oceanic CO<sub>2</sub> uptake by means of increasing biological productivity that sequester carbon and, lastly, the enhanced chemical weathering in soils. When talking about CDR techniques, the most relevant aspect concerns the time the carbon remains stored, that must be long enough to avoid release in the atmosphere after being captured. This strongly depends on which part of the environment it is stored. Another relevant aspect concerns the impacts on terrestrial ecosystems, that may vary depending on the adopted technology.

To better address these aspects, the following sections describe some recent studies regarding the most discussed CDR techniques, i.e., afforestation and direct air capture. In the next chapter, instead, a more comprehensive view of enhanced chemical weathering is provided.

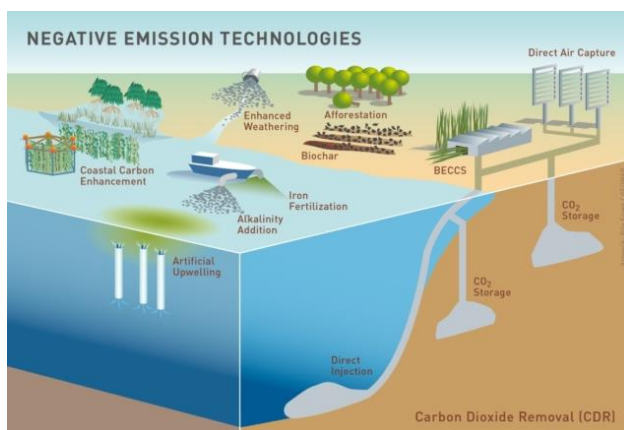


Figure 24 – Summary of the existing CDR techniques that remove carbon from atmosphere and store it within soil, plants, oceans or other terrestrial environments. The figure is taken from Betz, et al. [93].

### 2.2.1 Afforestation

Afforestation is considered as one of the most performing NCS to offset anthropogenic climate change. Indeed, CO<sub>2</sub> is removed from the atmosphere by plants, through the photosynthesis phenomenon, and the carbon within it may be stored in the vegetation itself or in the soil in the form of organic matter (i.e., vegetation litter). However, to have a more comprehensive view of the impacts of increasing the forested areas, it is important to largely analyze all the processes regarding carbon sequestration and changes in soil chemistry.

Williams, *et al.* [94] provided an insight of a great number of aspects linked to the change in forest cover across the United States, since scientific literature is characterized by different visions about effects of afforestation on global climate. As stated in the study, forest loss is detrimental for climate since deforestation leads to a reduction of evapotranspiration and, therefore, a consequent warming due to a decrease in cloud cover. However, there is also an increase in surface albedo that, as analyzed in section 2.1, results in a cooling effect. For this reason, when planning for an afforestation intervention, it may be important not to cover areas characterized by a high albedo with plants, since reflectivity of incoming solar radiation would be reduced otherwise, causing a warming effect. Furthermore, the amount of captured carbon from plants depends on the fate of vegetation litter. In general, carbon contained in dead leaves and roots leads to an increase in the sub-surface soil organic matter and, therefore, carbon may be released into the atmosphere by means of the soil respiration process. Another relevant aspect is connected to the release of Volatile Organic Compounds (VOCs) by trees, that has an influence on cloud formation and changes in global precipitation patterns. Russell, *et al.* [12] further affirms that the impacts on ecosystems strongly depends on the plant species involved. Indeed, afforestation also leads to changes in soil chemistry and, above all, on soil pH, since plants tend to uptake nutrients (i.e.,  $\text{Ca}^{2+}$ ,  $\text{Mg}^{2+}$  and  $\text{K}^{+}$ ) from soil water and release back  $\text{H}^{+}$  ions, in order to maintain a neutral charge balance. Other impacts on soil chemistry and

ecosystems are related to the type and amount of fertilizers, especially during the growing phase of the vegetation. All of these aspects need to be deeply analyzed, with the aim to see if an afforestation intervention on a certain area allows to face climate change in a sustainable time period and which are the related side effects (i.e., other benefits or drawbacks).

When an afforestation intervention is planned, a great importance is held by the comparison between the economic losses given by the land use change and the carbon sequestration provided by trees. This consists of a cost/benefit analysis, where the carbon gain is compared with the incomes of the previous land use type. To this regard, Duffy, *et al.* [95] analyzed a possible afforestation scenario in Ireland that would replace some livestock systems, responsible of the greatest part of greenhouse gases emissions of the country. The authors computed the carbon sequestration rate of the intervention and the amount of avoided emissions due to the change in land use and, lastly, they also carried out a sort of cost/benefit analysis. The estimation of trees carbon sequestration includes the evaluation of the carbon stored in plant biomass and in dead organic matter. Furthermore, the study takes into account the carbon emissions due to the conversion from grassland to forests, by making the difference between the total carbon stocks after and before the land use change. Regarding the avoided livestock greenhouse gases emissions, the authors calculated, basing on average values and IPCC guidelines, the rates of CH<sub>4</sub> and N<sub>2</sub>O emissions from cattle and manure management.

All of these carbon rates have been quantified, in economic terms, through a social cost of carbon, so that it has been possible to compare the carbon sequestration gain with the missing income due to the replacement of livestock with forests. Results revealed that, among all the possible forms of livestock systems, intensive dairy are those with higher greenhouse gases emissions. For this reason, replacing this land use with forests would provide the best carbon sequestration and emissions avoidance yields. Extending this intervention to a broader scale (i.e., 100,000 ha occupied by forests), the authors simulated a total carbon sequestration of about 14 Mt CO<sub>2</sub> in ten years after the land use change. This result even includes the emission avoided due to livestock displacement, which consists of about 37 % of this carbon sequestration amount. This study therefore highlights the importance of afforestation in the context of mitigating anthropogenic climate change. Particular role is played by which kind of land use is substituted by forests, since the greater the greenhouse gases emissions, the higher the carbon sequestration from the forested areas.

Since impacts of afforestation on carbon sequestration and soil chemistry strongly depends on the type of vegetation, Hou, *et al.* [13] analyzed the role of three different species situated in various parts of the globe. Such an analysis is certainly useful to estimate carbon sequestration rates of different vegetation species if direct measurements are not available. The authors considered three different tree species, i.e., deciduous broadleaf, evergreen broadleaf and evergreen conifer and analyzed their capability of sequestering soil organic carbon, with the

aim to define the best plant species in perspective of an afforestation intervention. The way of grouping trees to a single species proposed by the authors is made in purpose of having a more homogeneous as possible carbon sequestration rate of those trees belonging to the same plant species, given the same climatic condition (i.e., temperature and precipitation). This allows to define a single value of the carbon sequestration rate for each of the considered species, thus seeing which one tends to sequester more carbon. The organic carbon sequestration rate for each plant species has been evaluated after carrying out an extensive literature review about afforestation interventions all over the world, or simply about carbon sequestration of already forested sites. The carbon sequestration rate is generally evaluated as the plants carbon stock subtracted from the carbon stock of a non-forested site (i.e., cropland or grassland) close to the forested site under study. The tree grouping procedure within the three considered species classes has been carried out by means of a one-way analysis of variance (ANOVA) on the carbon sequestration dataset of different trees, in order to group in the same species trees characterized by non-significant differences in terms of carbon sequestration. Lastly, a multiple regression allowed to see the effects of plant species on carbon sequestration after afforestation. Figure 25, extracted from Hou, *et al.* [13], shows the linear regression lines interpolating Soil Organic Carbon (SOC) stock changes (i.e., carbon sequestration) with plants stand age (i.e., the time after afforestation), related to the three considered plant species. It is here possible to notice that the carbon sequestration

rate (i.e., the slope of the regression lines) is characterized by a great variation among the different species. In particular, the evergreen broadleaf provides the highest carbon sequestration rate, with a value of  $0.73 \text{ Mg ha}^{-1} \text{ y}^{-1}$ , followed by the evergreen conifer (i.e.,  $0.48 \text{ Mg ha}^{-1} \text{ y}^{-1}$ ) and the deciduous broadleaf (i.e.,  $0.42 \text{ Mg ha}^{-1} \text{ y}^{-1}$ ). These differences are mainly due to the plant physiology, such as their growth and litterfall rate, and also the litter composition (i.e., nutrients content). Therefore, in perspective to apply an afforestation intervention, the authors suggest to plant all those trees belonging to the evergreen broadleaf species, due to their greatest capability to sequester soil organic carbon.

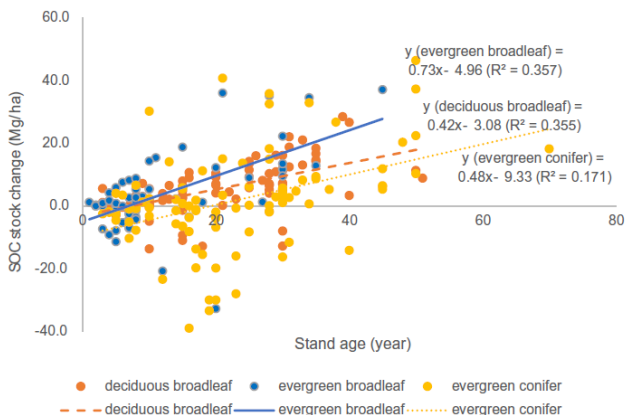


Figure 25 – Linear regression on the Soil Organic Carbon (SOC) stock change (i.e., carbon sequestration rate) vs the stand age for three different plant species (i.e., the time after afforestation). The figure is taken from Hou, et al. [13].

### 2.2.2 Direct air capture

Direct air capture is a CDR technique that consists of extracting CO<sub>2</sub> from the atmosphere by means of chemical sorbents and, then, store it into geological formations [12]. It is easy to imagine that, the carbon sequestration potential of this technology strongly depends on the trade-off between the CO<sub>2</sub> extracted from the atmosphere and the amount of energy and materials employed.

Deutz and Bardow [14] refers to two different types of direct air capture, i.e., absorption and adsorption. While the former extracts atmospheric CO<sub>2</sub> with aqueous sorbents, for instance alkali, the latter is based on solid sorbents, namely solid organic materials or amine supported on oxides. Both methods have their advantages and drawbacks, which differ depending on costs and required energy. The study proposes a detailed analysis about the environmental impacts of the direct air capture based on adsorption method, particularly analyzing two existing plants, by means of the life-cycle assessment technique. These plants consist of adsorbing CO<sub>2</sub> by means of a chemical reaction with the adsorbent material and a consequent desorption process working at temperatures close to 100 °C, that separates CO<sub>2</sub> from the adsorbent. Within this mechanism, the type of adsorbent material and the source of energy used to reach the required temperature for the desorption process, play a relevant role in the total carbon footprint of the plant. Regarding this latter aspect, Figure 26, taken from Deutz and Bardow [14], represents

the carbon footprint of captured CO<sub>2</sub> as a function of the carbon footprint of electricity (i.e., the energy source for direct air capture). It is here possible to see that, there is a linear relationship between these two variables, explaining that, if the carbon footprint of electricity increases, there is a greater carbon footprint of captured CO<sub>2</sub> and a consequent decrease in the carbon capture yield (right y axis of the figure). Comparing two different energy sources that provide high temperatures in the desorption process, i.e., the heat pump and waste heat, the study explains that extracting heat from waste leads to a greater carbon capture yield, respect to the heat pump system. However, for both types of energy sources, the future projection, when a greater efficiency of them is expected, highlights a higher carbon capture yield. This can be also seen by looking at the global future projections related to 2030 and, above all, to 2050, where the carbon capture yield can exceed values of 75% under both heat energy sources. Lastly, the two existing plants, the Hinwil in Switzerland and the Hellisheidi in Norway, are currently characterized by a high carbon capture efficiency, respectively of 85.4 % and 93.1 % since the former uses waste heat from municipal waste incineration and the latter employs geothermal energy. The study further explains that carbon sequestration efficiency can never reach 100 % because of the emissions related to the plant construction and, moreover, of the production of adsorbent materials. In addition, the required energy to store the captured CO<sub>2</sub> into geological formations must be taken into account, since it could lead to a reduction of the total carbon sequestration yield. A detailed analysis of all

the energy sources and adsorbent materials employed is therefore required before applying such an intervention, in order to let the carbon capture be higher than indirect emissions.

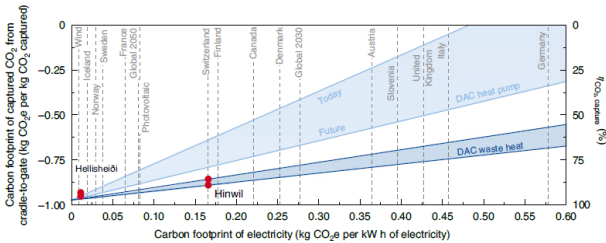


Figure 26 – Carbon footprint of captured CO<sub>2</sub> (left y axis) as a function of the carbon footprint of electricity. The right y axis shows the carbon capture yield. The shaded areas represent two different energy sources (i.e., heat pump and waste heat) in the current (i.e., upper line) and future (i.e., lower line) scenarios. The dashed lines, instead, represent the carbon footprint of different countries, including two renewable energy systems (i.e., wind and photovoltaic) and two global projections to 2030 and 2050. Lastly, the red dots represent the current and future carbon footprints of captured CO<sub>2</sub> by the two existing plants. The figure is taken from Deutz and Bardow [14].

All the possible side effects of direct air capture technology are needed to be considered before thinking to apply it at broad spatial scales. Among these, its influence on the energy and water demand plays a very important role since, as explained above, this technology requires a high amount of energy but, at the same time, it does not require a great amount of water, comparing to other CDR methods, such as afforestation.

To this regard, Fuhrman, *et al.* [96] analyzed the impacts of direct air capture on energy use and water availability, in the context of two global CO<sub>2</sub> representative emissions pathways, where the 1.5 °C climate target of the Paris Agreement is reached, in the first case (called high-overshoot) by the end of 2045 and, in the second case (called low-overshoot), by the end of 2055. Regarding the low-overshoot case, that is more realistic, the authors propose a direct air capture intervention at the global scale to be starting by the beginning of 2035, with particular reference to those nations that could provide a low-carbon energy sources and a significant geologic storage capacity for the sequestered CO<sub>2</sub>. These countries are United States, South America, China and Australia. By the end of 2035, direct air capture can induce a negative emission of 3 Gt CO<sub>2</sub>, which is bound to increase year by year if extensively applied.

Regarding the impacts on environmental systems, the authors compared the change in food supply due to the application of direct air capture and afforestation. It is true that, drought and floods are expected to more frequently occur due to global warming, reducing crop yields and increasing food price. However, the study affirms that an extensive land use change to forested areas, that would replace croplands, would lead to a reduced food availability with a significant price increase. This CDR drawback could be reduced by the application of low-energy-cost direct air capture, since the land use requirement is considerably less than afforestation. Furthermore, the study shows that water requirement of direct air capture is significantly less respect

to afforestation. However, this is exactly the opposite when talking about energy requirements. Considering the low-overshoot case, direct air capture requires about  $100 \text{ EJ y}^{-1}$ , which is a remarkable amount of energy that makes this intervention feasible only if renewable energy sources are employed. Further delays in applying this method, according to the study, could result in a higher energy demand for the intervention, with even more difficulties in reaching the Paris Agreement climate target by the above-mentioned times.

From the two above-cited studies one can evince that the most relevant aspect concerning the application of direct air capture is the great requirement of energy and materials, that may make the technique unfeasible if renewable sources are not used instead of fossil fuels. Chatterjee and Huang [97] analyzed both adsorption and absorption direct air capture processes at the Gt-CO<sub>2</sub> scale, in perspective to satisfy the climate target of 2 °C of the Paris Agreement, consisting of sequestering 30 Gt-CO<sub>2</sub> y<sup>-1</sup>. Analyzing both direct air capture methods, the authors come up with the idea that direct air capture requires enormous amount of energy and materials, due to different parts of the processes. The first high use of energy is due to the production of sorbent materials and to their replacement with a rate that is approximately 0.3 ton per ton of sequestered CO<sub>2</sub>. Other significant energy requirements are due to the huge heat production for CO<sub>2</sub> desorption process and the not negligible energy usage for carbon storage in geological formations.

For all of these reasons, the authors affirm that direct air capture is considered as a negligible option to offset global warming that does not allow to reach the Paris Agreement climate target, even if low-carbon and renewable energy sources are involved to reduce indirect emissions. Nowadays, indeed, the development status of low-carbon energy sources is not sufficient to limit the use of fossil fuels and, therefore, this technology at the Gt-CO<sub>2</sub> scale in the short term seems to be currently unrealistic.

## Chapter 3 - Enhanced Weathering for carbon sequestration: state-of-the-art and uncertainties

EW is considered as a CDR technique, belonging to the NCS group, since it aims to sequester atmospheric CO<sub>2</sub> by means of increasing the rates of naturally occurring chemical reactions in soils, using highly reactive minerals (i.e., silicates). EW is therefore the enhancement of the natural chemical weathering process, which is responsible of soil formation and plays a very important role in the carbon cycle. In the next sections, a focus on chemical weathering and on the current status of EW technique with its carbon sequestration potential and uncertainties is provided.

### 3.1 Chemical weathering

The weathering of rocks and minerals is a process that leads to a physical and chemical breakdown of particles, thus to the alteration of parent rocks. Minerals can be distinguished in two categories: primary minerals, those that have not been altered since their creation, and secondary minerals, which instead are the result of the physical and chemical alteration of the primary minerals. In the first category it is possible to place quartz, muscovite,

olivine and albite, while all the clay minerals, gibbsite and dolomite can be recognized as secondary minerals.

In general, weathering is a biochemical process that causes the physical disintegration and chemical decomposition of primary rocks and minerals [19]. Despite these two processes are very different, they happen simultaneously and are both fundamental in the alteration of original rocks and minerals. The physical disintegration breaks the original rocks into smaller particles which are more easily altered by the chemical decomposition process; indeed, the smaller the size of the particle, the higher the specific surface available to chemically react. Due to these processes, the particles of the original rocks/minerals tend to decrease in size and new soluble and/or stable products are created. These could combine with other substances to create secondary minerals, may be leached away from the soil or taken up by plants. Physical (or mechanical) weathering is caused by different factors, among which it is possible to include temperature, abrasion by water, ice and wind and the effect of plants and animals. The temperature excursions between day and night inevitably cause the expansion and contraction of minerals that constitute the rocks, making a consequent disintegration in smaller particles easier. Water, ice and wind actions, instead, result in rocks abrasion and their fragmentation as well as the action of plant roots and animals, which may erode and disintegrate rocks.

Chemical weathering, better known as biogeochemical weathering, due to the geological (water action) and biological (microbial and plant-root metabolism) aspects

constituting this phenomenon, is the ensemble of all the chemical and biochemical reactions that are responsible for modifying the nature of rocks and minerals. It is widely known [15,19,98] that these reactions are accentuated in hot and humid environments, that is exactly the opposite of what happens for physical weathering, that mostly occur under cold and dry climate conditions, as represented in Figure 27, taken from Peltier [99].

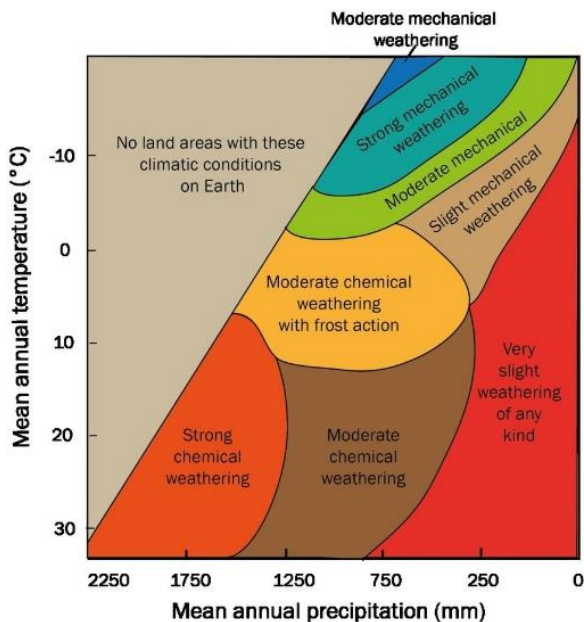


Figure 27 – Peltier's diagram showing the relevance of physical and chemical weathering with climatic conditions (i.e., mean annual temperature and precipitation). The figure is taken from Peltier [99].

The reactions taking part in the biogeochemical weathering occur because of various factors, among which the presence of water is the most important. Water is the reactant of several types of reactions, such as hydration, hydrolysis, dissolution, carbonation and acid reactions, oxidation-reduction and complexation. Furthermore, the presence of water significantly enhances the rates of the involved reactions, leading to a faster and greater production of secondary minerals. Apart from water, other important factors contribute to enhance the weathering reactions. More specifically, the presence of acids speeds up weathering rates since it results in a more accentuated activity by the hydrogen ions in water. Indeed, in many weathering reactions,  $H^+$  ions are the reactants that contribute to alter primary minerals to form secondary products. Further aspects enhancing weathering reactions rate are the nature of the primary minerals and land use. In particular, if the parent material contains limestone (i.e., calcite or aragonite), it releases calcium ion during dissolution, that causes a soil pH increase and a consequent slowdown of the reaction rate. At the same time, for example, forested areas are characterized by very acid soils, since trees tend to release  $H^+$  and  $Al^{3+}$  ions to the soil to balance the uptake of positive charged nutrients (i.e.,  $Ca^{2+}$ ,  $Mg^{2+}$  and  $K^+$ ). This represents an ideal environment for weathering reactions.

## 3.2 State-of-the-art of EW

Among all the CDR technologies recently introduced to mitigate climate change effects, EW is considered as one of the most promising [16,17]. The idea of enhancing naturally occurring weathering reaction rates was born from the fact that the dissolution of the greatest part of minerals naturally present in soils is generally a slow process, that results in small carbon sequestration rates, given that CO<sub>2</sub> is the reactant of many weathering reactions. EW is therefore the enhancement of this natural weathering process, simply achieved by adding highly reactive minerals, such as silicate minerals, to the soil [15]. Because of its high dissolution rate constant, as compared to other minerals [100], and relative abundance throughout the world, forsterite or Mg-olivine is one of the best choices. In general, olivine may be a silicate of Fe<sup>2+</sup> (i.e. fayalite) or Mg<sup>2+</sup> (i.e. forsterite, whose chemical formula is Mg<sub>2</sub>SiO<sub>4</sub>), but the latter is the most common choice [15,25,26] and, for this reason, hereafter it is simply referred to as olivine. This mineral can be found in mafic and ultramafic igneous rocks, such as basalt or gabbro, that are especially present in volcanic areas, or in dolomitic marbles. Its crystals present a green color, as represented in Figure 28 and, if grinded into nanometer size, particles are very hard, resistant at high temperatures and to water and many chemical agents action; it follows that dissolution rates are low anyway, especially in field rather than in laboratory

conditions, since many limiting factors slowing down the dissolution process are present.



*Figure 28 – Representation of a typical crystal of olivine (<https://www.minerals.net/mineral/olivine.aspx>).*

So far, the scientific literature does not present studies about actual applications of EW for carbon sequestration. Asibor, *et al.* [20], providing the technological readiness level for the most common CDR strategies (i.e., forestation, direct air capture, biochar and EW), highlights that the knowledge of EW process is currently stopped to some pilot scale experiments. Apart from these experiments, some modeling approaches estimating carbon sequestration potential of EW currently exist [29,30].

### 3.2.1 Laboratory characterization of EW

In the last decade, several experimental approaches have been carried out to characterize olivine, or any other silicate mineral used for EW, dissolution dynamics. These are mainly based on laboratory experiments conducted on single mineral particles [22,23] or pot and mesocosm experiments [24-28], with conditions that are more similar to the field. In laboratory, dissolution rates are commonly derived by fixing pH to low values (commonly to 5), high temperature (i.e., 25 °C), when the reaction is far from equilibrium conditions and considering olivine particles as perfect spheres with diameters of the order of magnitude of a few microns [100-102]. In field conditions, instead, evaluating olivine dissolution rates in a reliable way is still a challenge, due to the great number of unknown or not widely explored aspects that influence the olivine weathering reaction [21]. For instance, Vicca, *et al.* [29] defines the most common uncertain aspects that happen in field and are not easily replicable in laboratory. They regard the formation of secondary minerals, the alteration of soil hydrological properties due to silicate amendments, the formation of preferential flow path in soil pores and the action of fungi, bacteria and microbes that, depending on soil pH, may accelerate or slow down the organic matter decomposition, which is one of the CO<sub>2</sub> sources, and silicates dissolution rate. To try addressing these uncertainties, ten Berge, *et al.* [26] and Renforth, *et al.* [25] conducted pot experiments to estimate the olivine weathering rate in soils extracted from agricultural fields,

while some years later Amann, *et al.* [24] realized a mesocosm experiment to reproduce an even more similar condition to the field, with respect to the two above-mentioned works.

In ten Berge, *et al.* [26], a pot experiment was carried out for 32 weeks at Wageningen (Netherlands), with the aim to explore, apart from olivine weathering rate in field, the effects of olivine dissolution on plant growth and nutrient uptake. The experiment considered seven different situations; a first control situation, where no olivine is added, four pots with different doses of olivine powder (8, 40, 200 and 1000 grams of olivine per pot) and other two pots fed with kieserite, a fertilizer that is high in magnesium. Olivine was originally ground according to a particle size distribution, so that to have a certain mass fraction for different particle sizes, and then it was mixed to the soil extracted from an agricultural field, being poor in magnesium and potassium. Regarding the type of vegetation, a perennial ryegrass species was chosen because of its capability to adsorb huge amounts of nutrients over long periods.

At the beginning of the experiment, all pots were fertilized by adding sodium, potassium and phosphorous to enable the initial step of plant growth. The same practice has been conducted at each harvest. Then, pots were fed with olivine and, at the end of the experiment, the amount of weathered olivine (i.e., the dissolved part of the initial dose) was determined with different methods and results were then compared. The first one consisted of evaluating the weathered olivine on the base of the  $Mg^{2+}$  balance,

comparing pots fed with different olivine doses and the control situation, without olivine. This method relies on the fact that, when dissolving, olivine releases magnesium in solution; therefore, the higher the initial olivine dose, the greater the magnesium concentration in soil water. The second method compares magnesium concentration in soil water of those pots fed with different olivine concentrations and those fertilized with kieserite, with the aim to compare the effects on different response variables, for instance plant growth and nutrient uptake, of the two minerals. Assuming that the same amount of magnesium is dissolved from olivine and kieserite, the authors were able to calculate the fraction of olivine used for weathering by making the difference of the dissolved magnesium in soil water found in each pot fed with olivine and the amount of dissolved magnesium from kieserite application used to have the same variation of an output variable X (i.e. the concentration of a certain ion in soil water). The weathered olivine estimated by the two methods were also compared to the kinetic values calculated through equations coming out from laboratory experiments (Olsen's method), that takes into account the effects of pH and temperature on weathering rate. This comparison led to a general underestimation of weathering rates obtained using soils extracted from field, that is more accentuated in the first method, mainly due to the fact that the part of magnesium, coming from olivine dissolution, exchanged with soil colloids or stored in plant biomass is not here taken into account. Comparing the first and the second methods, entirely based on field soils, the authors obtained a

weathering rate value between  $10^{-14}$  and  $10^{-16}$  moles  $\text{cm}^{-2} \text{s}^{-1}$ , that is about four orders of magnitude less than laboratory estimates.

The authors then evaluated the effects of olivine on plants by analyzing the concentrations of seven different elements (N, P, K, Mg, Ca, Si, Ni), finding an increase in magnesium and silicates concentrations in plant dry matter that became more relevant as the olivine dose increased. As a change in soil chemistry, an increase in soil water pH with the amount of added olivine has been found as well, due to the fact that olivine consumes  $\text{H}^+$  ions during dissolution. Regarding carbon sequestration, the authors based on the gross estimate of the sequestered  $\text{CO}_2$ , considering the stoichiometric ratio between the reacted olivine and  $\text{CO}_2$  in the weathering reaction. This is equal to 1.25 kg of sequestered  $\text{CO}_2$  per kg of olivine reacted. However, the authors specified that the net sequestration is definitely lower than the gross one since part of the carbonates resulting from olivine dissolution can react with the acids present in the soil, sending back  $\text{CO}_2$  in the atmosphere.

The pot experiment conducted by Renforth, *et al.* [25] assessed the weathering rates of olivine added to three samples of soil extracted from an agricultural site situated in the North of Oxford, UK. The authors collected the soil samples within a column 1-meter-high and 0.1-meter diameter and derived olivine dissolution rates by adding olivine from the top of the column and studying the chemical properties of the leached water. Olivine, originally extracted from a site in Norway, was ground at a certain particle size distribution and 100 g of it were added

to two samples of soils under 0.2 m of terrain, corresponding to about  $12 \text{ kg}_{\text{olivine}} \text{ m}^{-2}$ , while the other sample was considered as a control case study since no olivine was added. The particle size distribution represents the olivine mass fraction for different particle sizes; in this case, the diameter ranges from about  $50 \mu\text{m}$  to  $500 \mu\text{m}$ , with the greatest percentage of the mass of olivine (i.e., about 78 %) characterized by a diameter greater than  $125 \mu\text{m}$ . The temperature under which the experiment was conducted was about  $19 \text{ }^\circ\text{C}$ , fixed constant during all the duration of the experiment. The whole experiment was carried out over five months, during which all the soil columns were kept at saturation, maintaining a continuous extraction of leached water from the bottom.

A comparison of the chemical composition of soil water between the samples including olivine and the control system is provided in Figure 29, taken from Renforth, *et al.* [25], where the concentration of different ions across the days that involved the experiment is represented. Results revealed that the  $\text{Mg}^{2+}$  concentration in solution related to the sample including olivine resulted much higher than that of the sample without olivine. This is certainly due to the fact that olivine releases magnesium during its dissolution. However, a significant increase of  $\text{Ca}^{2+}$  concentration in soil samples treated with olivine was detected as well. The authors attributed this fact to the cation exchanges between soil solution and colloids in solid phase. Furthermore, an increase in soil water pH has been noticed in the samples fed with olivine, given that it consumes  $\text{H}^+$  ions during the

dissolution process and  $\text{Mg}^{2+}$  release increases the alkalinity of the solution.

The olivine dissolution rate was calculated by comparing the dissolved  $\text{Mg}^{2+}$  concentrations in the effluent of the samples fed with olivine and the one of the control system. They found dissolution rate values around  $10^{-15}$  moles  $\text{cm}^{-2} \text{ s}^{-1}$ , which were comparable with those obtained in the pot experiment of ten Berge, *et al.* [26] and are much lower than the typical laboratory weathering rate, which are about  $10^{-11}$  moles  $\text{cm}^{-2} \text{ s}^{-1}$  [101-103] confirming that in field there are many limiting factors reducing the weathering rates, which are not taken into account in laboratory experiments.

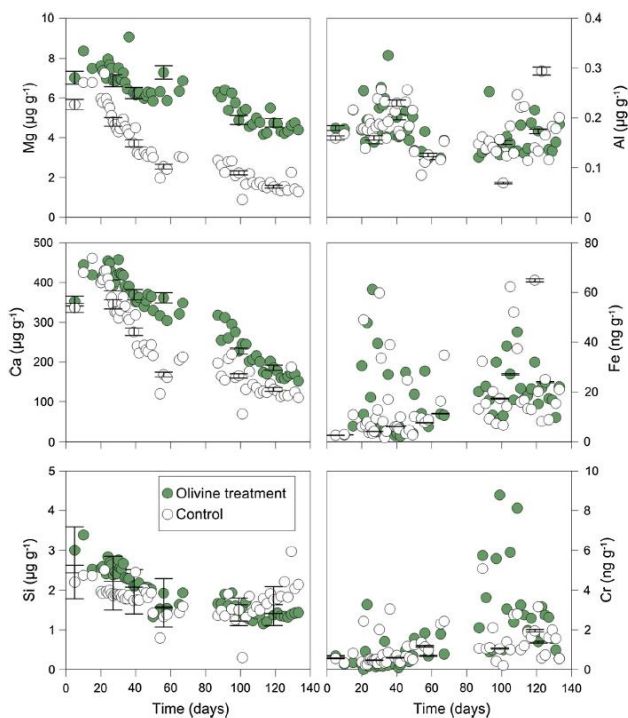


Figure 29 – Concentration of different ions in soil water extracted from olivine treated soil columns and a control system, where no olivine was added. The figure is taken from Renforth, *et al.* [25].

Amann, *et al.* [24] realized a mesocosm experiment adding olivine to an agricultural loamy sand soil, extracted from a field in Belgium. The most common crops in that area, i.e., wheat and barley, are considered in the experiment and irrigated using an irrigation system which

provides the equivalent annual rainfall amount of 800 mm. The experiment is also able to reproduce some processes that are very common in field, such as the occurrence of long dry periods, secondary mineral formation, cation exchange and the formation of preferential flow paths. The effects of olivine amendment were assessed by monitoring the chemical characteristics of soil water, particularly looking at pH, magnesium and silicates concentration and Dissolved Inorganic Carbon (DIC). The achieved weathering rates are on the order of magnitude of  $10^{-13}$  mol  $m^{-2} s^{-1}$  and the related carbon sequestration rates range from 23 and 49  $kgCO_2 ha^{-1} y^{-1}$ . Achieved weathering rates are much lower than those derived in laboratory setups [101,102] and those resulting from soil column experiments under controlled conditions [25,26], stressing the discrepancy between lab and field conditions, which is generally due to an ensemble of intrinsic and extrinsic factors, that in laboratory are not easily reproducible.

### 3.2.2 EW modeling approach

Apart from laboratory experiments conducted on soil samples extracted from fields or more advanced mesocosm experiments, as those presented above, models can play a very important role for extrapolating results of laboratory and field experiments in both time and space, as well as for quantifying the impact of hydroclimatic fluctuations on the involved biogeochemical processes. Vicca, *et al.* [29]

highlights that only a few models connecting EW dynamics with plants, climate and biogeochemical processes exist.

Some of them are reactive transport models, that simulate the interactions among plants and soil biogeochemistry, taking into account, in some cases, the EW process [30]. However, in most of these models not all these processes are considered at the same time and the demanding numerical constraints of the vertically explicit formulation may limit the time horizon of their simulations. In particular, they present many uncertain aspects and limitations. These mainly regard about establishing which, among the many occurring chemical reactions, are the most important and, therefore, need to be included in the model. Then, many of the existing reactive transport models consist of the numerical resolution of partial derivatives equations and, for this reason, the temporal scales are often small, requiring long times of simulation. Furthermore, for the sake of simplicity, they often consider homogeneous hydraulic and chemical properties of the soil, which is far from natural conditions. In any case, if the simulation time horizon is not too long, this assumption may be considered as reasonable. Lastly, they do not consider hydrologic fluctuations of rainfall, that reflect in soil moisture, often considering a constant vertical Darcy velocity of water flow. This is a strong limitation when, especially for EW, the role of hydrological processes is very important.

Taylor, *et al.* [30] provides an overview of the mostly known reactive transport models, describing their capabilities and limiting aspects, mainly due to neglecting some important processes for simulating soil dynamics. In

Table 1, taken from Taylor, *et al.* [30], the characteristics of some reactive transport models are presented, with the aim to make a comparison between the processes they simulate and the degree of complexity. It is here possible to see that EW process is only included in the *Sheffield* model and is planned to be integrated in the *ICZ* model. Other presented models, instead, are limited and focus on exploring the interactions between hydrology and soil biogeochemistry, without implementing any carbon sequestration solution, since their use is more devoted to address soil sustainability and land care practices.

The *ICZ* [104,105] is a dynamic mathematical model that is able to simulate, at a site scale, the crop growth process, greenhouse gases production, the soil organic matter and chemistry time dynamics and natural CO<sub>2</sub> consumption (i.e., the background weathering phenomenon that naturally occurs in soils). The sub-surface water flow is simulated through the Richard's equation and the weathering rates of background weathering fluxes are those resulted from laboratory experiments, that compute dissolution rates on the base of the kinetic of weathering reaction. In addition, this model considers the slowdown or acceleration of natural weathering reactions due to the presence of bacteria and fungi in the soil, that represents one of the factors bringing more uncertainty in field weathering rate estimation, and also plants nutrients uptake. The cation exchange process between the soil solution and organic and inorganic colloids is also simulated, based on Fick's diffusion law, and the exchanged species are calcium, sodium, magnesium, potassium and phosphorous.

It is hence possible to affirm that the *ICZ* model is rather complete, given the great number of simulated processes, even with a high degree of complexity, given that it evaluates the time dynamics of many variables. However, this model still does not take into account the EW of silicate minerals, hence it is not possible to make a prediction of carbon sequestration rates. Furthermore, carrying out an extensive application at the global scale is a rather difficult task, given that it works at the site scale due to its high degree of complexity. Indeed, this model is better addressed to analyze the interactions between soil, plants and local hydrology, with the aim to design sustainable agricultural management practices.

Respect to the *ICZ*, the *Sheffield* model [106] is able to simulate, at a global scale, the CO<sub>2</sub> consumption for EW and the soil chemistry dynamics, also taking into account the effects of EW on ocean acidification. However, due to the spatial scale of interest it does not consider crop growth and cation exchange processes. This is a very relevant drawback for this model since these two processes, above all cation exchange, determine a significant change in pH time dynamics, that is one of the main factors affecting weathering rate, thus resulting in a possible misinterpretation of carbon sequestration rates.

The *WITCH* model [107-109] works at a regional spatial scale, that is an intermediate condition between the *ICZ* and the *Sheffield* models. Like this last model, due to the spatial scale of interest, the crop growth, the greenhouse gases production and soil organic matter dynamics are neglected. The *WITCH* model basically evaluates the

natural CO<sub>2</sub> consumption, without considering EW process. It is also able to reproduce the temporal dynamics of the concentration of the most common ions in soil water, such as calcium, magnesium, sodium and potassium, for which the plant uptake is also simulated. The cation exchange process between the soil solution and organic and inorganic colloids is simulated, as in the *ICZ* model, by means of the Fick's diffusion law, but considering only calcium, magnesium and potassium as exchangeable species. The same consideration done for the *Sheffield* about the excessive simplification of the model is valid also for the *WITCH* model. However, since it is mainly devoted to understand soil chemistry dynamics at the catchment scale, rather than carbon sequestration purposes, many of its assumptions, such as those on greenhouse gases production and EW, may be considered as reasonable.

Regarding the *PROFILE* model [110], it is a steady state soil chemistry model that simulates, at a site or catchment scale, soil chemistry dynamics and naturally occurring weathering fluxes, without calculating CO<sub>2</sub> consumption. As reported in Table 1, there are many different phenomena that are not taken into account, hence the model is characterized by a high degree of simplicity. However, respect to the above-mentioned models, it simulates in a more realistic way the cation exchange capacity component, since it is calibrated based on site data and there is a wide pool of exchangeable species, that are base cations, such as Ca<sup>2+</sup> and Mg<sup>2+</sup>, and also H<sup>+</sup> and Al<sup>3+</sup>. Indeed, it is known that, in wet forested soils, aluminum exchange strongly prevails on the other ions exchange.

The dynamic version of this model is the *SAFE* model [111] that, as the *PROFILE*, has been widely used to simulate soil chemistry time dynamics in strongly acid forested environments. Since it is an upgrade of the *PROFILE* model, the processes simulated and neglected by the *SAFE* are almost the same. These two models, indeed, do not integrate an EW component, therefore they do not allow to simulate carbon sequestration by silicate minerals.

*MAGIC* [112] is a dynamic soil chemistry model that works at the catchment scale, simulating changes in soil chemistry including carbon and nitrogen cycles and cation exchange capacity, simulated through the Langmuir approach, including the basic cations, aluminum and sulfates as exchangeable species. Regarding weathering processes, it considers the naturally occurring background weathering, which is calibrated basing on the chemical soil composition, but EW and consequent carbon sequestration are not included.

The *APSIM* model [113], instead, simulates, at a site scale, crop growth, soil organic matter, pH time dynamics and soil water balance. However, it does not consider the cation exchange capacity and all the weathering processes of the naturally present minerals in soil. Regarding soil chemistry, the model only includes pH time dynamics, even though the model evaluates nitrogen and phosphorous cycles, since it has been developed with the aim to well estimate biophysical processes in farming systems. For this reason, EW and carbon sequestration are not fields of interest of this model.

Lastly, the *DayCent-Chem* [114], is a dynamic reactive transport model that is able to simulate crop growth, soil organic matter and chemistry time dynamics at a catchment scale. The model uses the Richard's equation to simulate sub-surface water flow and takes into account naturally occurring weathering fluxes of minerals present in the soil. This latter term requires to be calibrated, depending on chemical composition of the soil under study, as well as the cation exchange capacity term, that bases the exchangeable species on the analyzed soil characteristics. As many of the previously presented reactive transport models, the *DayCent-Chem* does not allow to simulate EW and carbon sequestration, since it is widely used for simulating greenhouse gases fluxes and changes in water chemistry of rivers in alpine catchments.

Furthermore, Lewis, *et al.* [115] presents an application of a 1-D reactive transport model to simulate EW carbon sequestration potential and the release of base cations (i.e.,  $Mg^{2+}$ ,  $Ca^{2+}$ ,  $K^+$  and  $Na^+$ ) that can be beneficial for plants. Like many other reactive transport models, a constant average infiltration rate is here assumed, thus not allowing to see the effects of rainfall seasonality on EW. The application of  $50 \text{ t ha}^{-1}$  of basalt leads to a carbon sequestration potential between 1.3 and  $8.5 \text{ tCO}_2 \text{ ha}^{-1}$  of after 15 years of amendment. These values, however, are much higher than the one resulted from the experiment of Amann, *et al.* [24], which actually represents a situation closer to the field environment. This large discrepancy emphasizes the need of joining model simulations and experimental results, for instance by calibrating model

parameters with increasingly available experimental data, to obtain more realistic carbon sequestration estimations.

*Table 1 – Characteristics of the most known reactive transport models. The table is taken from Taylor, et al. [30].*

model	IGZ	Sheffield	WITCH	PROFILE
dynamic	yes	yes	yes	no
typical scale of usage	site	global	regional or catchment	site or catchment
driven by	site data	DGVM output	DGVM output	site data
crop growth processes	yes	no	no	no
GHG production	yes	no	no	no
soil hydrology	Richard's equation	water balance	input for each layer	input for each layer
SOM dynamics calculated	yes	no	no	no
soil chemistry calculated	yes	yes	yes	yes
weathering rates	kinetics	kinetics	kinetics	kinetics
CO <sub>2</sub> consumption	yes	yes	yes	no
enhanced weathering	planned	yes	no	no

model	SAFE	MAGC	APSIM	DayCent-Chem
dynamic	yes	yes	yes	yes
typical scale of usage	site or catchment	catchment	site	catchment
driven by	site data	site data	site data	site data
crop growth processes	no	no	yes	yes
GHG production	no	no	N <sub>2</sub> O, CO <sub>2</sub>	N <sub>2</sub> O, NO <sub>x</sub> , CO <sub>2</sub>
soil hydrology	input for each layer	input for each layer	bucket or Richard	Richard's equation
SOM dynamics calculated	no	no	yes	yes
soil chemistry calculated	yes	yes	pH	yes
weathering rates	kinetics	input	none	input
CO <sub>2</sub> consumption	no	no	no	no
enhanced weathering	no	no	no	no

An attempt to quantify the carbon sequestration potentials of silicate EW and related costs at the global scale, exploring the possible contribution of different countries, has been provided by Beerling, *et al.* [116]. The study applies an integrated modeling approach (EW model joined to a costs/benefit analysis) to see the related contributions of croplands of different nations worldwide to carbon sequestration. The CDR potential is evaluated under the Business-As-Usual (BAU) and the 2 °C degree

warming scenarios. BAU considers the application of the current energy policies even in the future, while the latter focuses on energy policies aiming to limit global warming to 2 °C by 2050.

The modeling part regarding EW consists of a one-dimensional reactive transport model that considers dissolution of silicate-rich basaltic rocks under a steady state water flow. The changes in the concentration of the dissolved silicate mineral, released by the dissolution of basaltic rock, are evaluated through a transport equation, where partial derivative of the concentration of the dissolved mineral respect to the time and depth is considered, in order to take into account its variation due to the continuous dissolution of the rock and the vertical water flux. This equation is coupled with the basalt mineral mass balance, that expresses changes in the mass of original basalt rock as a function of its weathering rate, thus estimating the amount of mineral transferred from the solid phase to solution. Lastly, the total mass of basalt rock used for weathering is evaluated as the integration of the concentration of silicate minerals released from the original basalt rock, over a certain time window and the domain of interest.

The basalt minerals weathering rate is calculated as a function of soil hydrology (i.e., a constant steady state water flux), soil temperature and pH, which is assessed through a mass balance equation of  $H^+$  ions, that considers input from plants and a background dissolution of carbonate minerals. The net  $CO_2$  sequestration is computed by the model as a function of the excess of bicarbonate

( $\text{HCO}_3^-$ ) and carbonate ( $\text{CO}_3^{2-}$ ) ions produced by basalt rock dissolution. In this calculation, even  $\text{CO}_2$  emissions due to grinding of basalt rock and transporting operations are taken into account. Regarding costs estimation, the authors considered the costs of mining, processing, distribution, transport and spreading olivine on fields. They found that the greatest energy use is due to grinding operation of basalt rock, that is also the biggest source of carbon emission in the whole EW procedure.

In Figure 30, extracted from Beerling, *et al.* [116], the net CDR produced by basalt rocks EW in croplands for different nations worldwide is provided. The figure shows the net sequestered  $\text{CO}_2$  and 90 % confidence intervals under the BAU and the 2 °C degree scenarios, analyzing how the CDR potential varies with the fraction of cropland areas devoted to EW. It is clear that, as the fractional cropland area increases, there is a corresponding increase in the net sequestered  $\text{CO}_2$  that, for some nations, reaches an asymptotic value as the area fraction involved in EW technique approaches to 1. United States, China and India have the greatest CDR potential, as compared to the other countries, that can reach about  $0.75 \text{ Gt CO}_2 \text{ y}^{-1}$ . The order of magnitude of CDR for European countries is instead much less, i.e.,  $0.05 \text{ Gt CO}_2 \text{ y}^{-1}$ . These carbon sequestration rates are similar to those provided by other CDR techniques, such as afforestation and direct air capture. The curves are almost the same under both the considered energy policies scenarios for many countries. The greatest difference between the average sequestered  $\text{CO}_2$ , under the two analyzed energy scenarios, is recorded for China, since

the 2 °C scenario considers a much relevant use of low carbon technologies, leading to a significant reduction in indirect emissions.

Regarding the feasibility of EW technique, the authors found an average global cost of about 100 USD per ton of sequestered CO<sub>2</sub>, with the highest values obtained for United States, Canada, China, Poland and Spain, especially for great fraction of involved cropland area. The differences in costs depend on many factors, such as the cost of electricity for mineral grinding, transport and spreading operations. Even in this case, the authors found similar costs values of other CDR techniques, leading to consider EW as a reasonable intervention to mitigate climate change.

The CDR estimates of this reactive transport model have to be considered in the context of the relatively low degree of complexity, that allowed to make predictions at the global scale. Indeed, the same authors affirm that their results are subject to several uncertainties, mainly connected to the derivation of field weathering rates starting from laboratory ones, given the enormous number of factors that, in field conditions, contribute to slow down the dissolution process. Furthermore, the reactive transport model simulates a constant steady state water flow, that is far from natural conditions. A stochastic characterization of rainfall, hence of soil moisture, would be necessary to estimate field weathering rate variation in a more reliable way, given that, as stated above, the presence of water is one of the main factors affecting minerals dissolution.

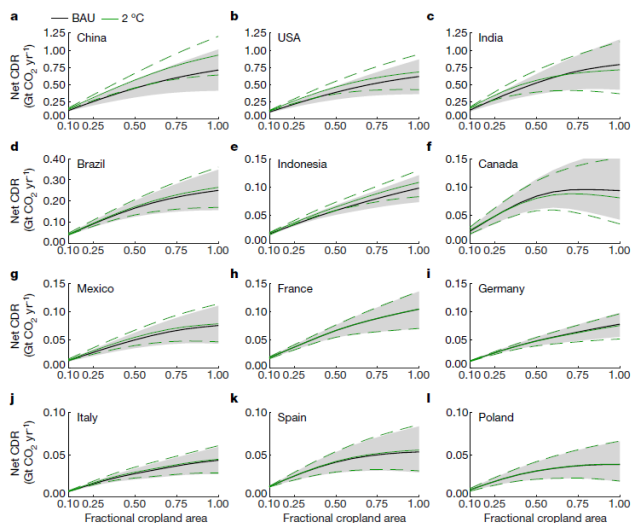


Figure 30 – Net sequestered CO<sub>2</sub> in cropland areas for different nations under the BAU (black lines and gray shaded areas) and the 2 °C (green continuous and dotted lines) scenarios. The figure is taken from Beerling, et al. [116].

### 3.3 Uncertainties of EW in field

Before thinking for large scale applications of EW in natural environments, a more in-depth knowledge of the interaction and feedbacks among the processes involving hydrology and soil biogeochemistry is necessary. Indeed, EW assessments, in field conditions, are affected by large uncertainties, originating from the feedbacks between hydrological and biogeochemical processes. These, in fact, regard multiple spatial scales, starting from the details of

the chemical reaction at the nanoscale, up to the hydrologic transport of weathering products (i.e.,  $\text{HCO}_3^-$ ) at regional to continental scales. The uncertainties may be amplified moving from a shorter timescale, for instance the daily scale where oscillations between wet and dry periods are small, to longer timescale, such as decades or centuries, where changes in precipitation patterns, thus in soil moisture, may significantly happen. For this reason, it is very important to detect all the aspects affecting EW dynamics in fields and address all the possible uncertainties, modeling them in the most reliable way, in order to avoid misinterpretation of the dissolution of the analyzed minerals, thus wrong carbon sequestration estimates. In the following subsections, two important sources of uncertainties of EW in field are discussed, i.e., the extrapolation of laboratory dissolution rates in field conditions and the destiny of the weathering products on the way to the oceans.

### 3.3.1 From laboratory to field weathering rates

The extrapolation of field weathering rates from values obtained under laboratory conditions is subjected to many sources of uncertainty, mainly due to the fact that ideal and well known conditions are set up in laboratory while, in field, there are many factors playing a relevant role in the dissolution dynamics that are difficult to predict and quantify. The different uncontrolled factors that act in field have been distinguished in two categories: extrinsic factors,

involving the environment in which the weathering reactions take place, and intrinsic factors, that are related to the properties of the mineral surface [21].

Among extrinsic parameters it is possible to list wetness, temperature and soil pH [19]. In laboratory conditions these factors are well controlled, in order to accelerate the slow dissolution process of silicate minerals and quantify the related weathering rate in reliable times. Experiments are conducted at high temperature, usually fixed at 25 °C, at low pH, i.e., 5, under saturation and far-from-equilibrium conditions [100-103]. The resulting weathering rates, under these conditions, are of the order of magnitude of  $10^{-12}$  moles  $\text{cm}^{-2} \text{s}^{-1}$ . The greatest part of existing reactive transport models tries to reduce these values by means of some corrective factors taking into account the actual pH, soil moisture and temperature, sometimes considering their temporal dynamics as well. However, the actual order of magnitude of field weathering rates is still unknown, due to the impossibility to conduct an analysis in field conditions, given the low dissolution rates and the great number of triggering factors, that spatially varies in a significant way. An attempt to overcome this issue has been conducted by some pot experiments on soil extracted from fields [25,26]. Despite some assumptions related to the laboratory setting, these experiments revealed that field weathering rates are much lower than laboratory ones and their order of magnitude varies in the range  $10^{-14}$  -  $10^{-16}$  moles  $\text{cm}^{-2} \text{s}^{-1}$ .

Another extrinsic factor can be the water flow path in the unsaturated soil in which the dissolution of mineral

particles occurs [117,118]. Indeed, the presence of preferential flow paths leads to a faster dissolution of those particles within these paths, due to a higher time of contact with water, and a slower dissolution of particles that are not involved in the water flux. This aspect must be considered along with the distribution of mineral particles diameter resulting from the grinding operation. In general, as the particle size decreases, the weathering rate tends to increase, due to the growth of the specific particles surface area [19,100]. However, the dissolution dynamics are also affected by the time and quality of contact between water and particles, thus they depend on the flow paths and the particles distribution in the soil. Basing on these considerations, a spatial distribution of the weathering rate in the unsaturated porous soil may be therefore important to be assessed since it strongly influence the overall carbon sequestration rate. Another important aspect is connected to the water quality and to the presence of bacteria and fungi in the soil [119,120]. They may accelerate or slow down the minerals dissolution rates due to their capability to alter the particles surfaces. However, despite this aspect has been recognized as one of the most important in leading to discrepancies between laboratory and field weathering rates, not many efforts have been conducted to quantify its influence on EW dynamics so far, mainly due to the difficulty in predicting the presence and concentration of bacteria and fungi in the soil. In laboratory, water quality and water/mineral contacts are well controlled, while in field their characterization is rather difficult. Further work in better estimating these extrinsic factors, from both the

experimental and modeling fronts, is needed to improve estimates of field reaction rates.

The intrinsic factors, instead, regard the dynamics and evolution of the specific surfaces of mineral particles during dissolution [19]. The specific surface area, expressed in  $\text{m}^2 \text{g}^{-1}$ , represents the surface available for reaction per gram of the mineral and is always indicated as Brunauer-Emmett-Teller (BET) surface. It is known that, the smaller the particle size, the higher the specific surface area. This fact is mainly due to the roughness of the particles surfaces and the presence of nanoporous layers that leads to more available space for the weathering reaction between minerals and dissolved  $\text{CO}_2$  in soil water [121].

Modeling the evolution of surface roughness is quite difficult in field, since there is not the possibility to directly explore the evolution of the single particle, that can dissolve in a different way than the others, due to different flow paths. In laboratory settings, this aspect is easy to monitor since well calibrated single crystals, characterized by a great specific surface area, are used under fixed and ideal conditions of wetness, temperature and pH [122]. In this way, the dissolution rates and evolution of mineral specific surface areas are overestimated, with respect to field conditions. Actual soils also present many other minerals, apart from the one under study, that can act on slowing down the dissolution of the considered mineral, due to a sort of competition among them.

Given all these uncertainties, many existing reactive transport models still follows the approach presented in

Lasaga [100], thus considering the specific surface area as equal to the geometric area of mineral particles, that are considered, for the sake of simplicity, as simple spheres. The main advantage of this approach is given by its simplicity but, at the same time, it neglects many important aspects that play a very relevant role in the dissolution of the considered mineral, such as the roughness of its surface and the presence of nanoporous layers, that contributes to enhance the available surface for the reaction with dissolved CO<sub>2</sub>. New experimental approaches, that better reproduce field conditions in laboratory, may help to quantify these aspects in a more reliable way and integrate in weathering models, to better estimate field weathering rates and carbon sequestration.

### 3.3.2 The destiny of weathering products while moving towards the oceans

Many existing reactive transport models estimate carbon sequestration rates based on the stoichiometry of the weathering reaction between silicate minerals and CO<sub>2</sub>. Focusing on olivine, this reaction leads to 1.25 grams of sequestered CO<sub>2</sub> per gram of dissolved olivine. However, this represents a theoretical limit and is always referred to a “gross” carbon sequestration rate, since it tends to overestimate the amount of sequestered carbon due to the fact that it does not consider all the processes that contribute to slow down the weathering reaction [15,25]. When olivine reacts with CO<sub>2</sub>, carbonate and bicarbonate ions are

produced in the dissolved form. As long as they remain in soil water, they could potentially react with  $H^+$  to form carbonic acid, causing an increase in pH and a consequent slowdown of the olivine dissolution rate. For this reason, the extra amount of  $HCO_3^-$  and  $CO_3^{2-}$  that is in soil water after olivine dissolution represents the  $CO_2$  that reacts with olivine. The actual carbon sequestration, instead, is more closely related to the extra  $HCO_3^-$  and  $CO_3^{2-}$  that are leached away from the soil (i.e., carbon sequestration into the oceans), or to those that precipitate forming solid carbonate minerals (i.e., carbon sequestration in soils). Figure 31 is a schematic representation of the processes involved in soil EW. Panel A displays the addition of highly reactive silicate minerals to the soil and their reaction with  $CO_2$  under the hydroclimatic force. Then, weathering products (i.e.,  $HCO_3^-$  and  $CO_3^{2-}$ ) leach to deeper soil layers, moving towards the oceans through the streams. Panel B, instead, represents more in detail the dissolution of silicate minerals and the formation of weathering products within the soil system.

However, when these ions are leached away from the soil domain, their fate on the way to the oceans is uncertain and depends on multiple factors that may cause the release of carbon within them back to the atmosphere, negatively affecting the total carbon sequestration rate [123]. For this reason, it is worth analyzing the most important aspects that may interact with these ions in their path toward oceans, in order to reliably quantify carbon sequestration. Among these, the exchange between cations dissolved in soil water and negatively charged clay and organic soil colloids

strongly affects EW yields [15]. The greater the cation exchange capacity of the soil, the greater its buffering capacity, namely its ability to offset pH changes. Olivine dissolution consumes  $H^+$  and releases  $Mg^{2+}$  ions, increasing soil water alkalinity. As soon as  $Mg^{2+}$  increases in the soil solution, there is a greater adsorbed amount of this ions on soil colloids. As a consequent effect, magnesium replaces adsorbed calcium, sodium and potassium ions, which are thus released in the solution. The calcium increase in soil water may result in a greater formation of calcium carbonate ( $CaCO_3$ ), that can be a source of  $CO_2$  release into the atmosphere, especially in presence of nitric acid ( $HNO_3$ ), that is considered as a common anthropogenic acid [15]. Therefore, the greater adsorption of EW cations, in soils having a greater cation exchange capacity, may reduce EW yields. If, while moving towards the oceans, EW products run into soils with a great cation exchange capacity that also contains nitric acid, there may be a consequent  $CO_2$  release into the atmosphere, resulting in a loss of EW efficiency.

Other mechanisms of reducing EW yields in the path from soil to the oceans are still not well known or are poorly explored. A great research effort in clarifying these aspects is needed, in order to see if EW is a powerful technology for carbon sequestration and if it is worth to be applied at a global scale.

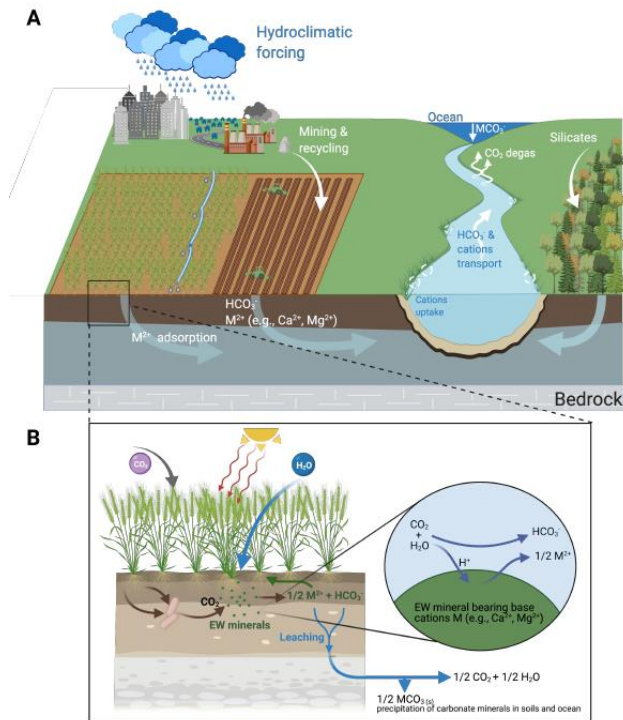


Figure 31 – Overview of the processes involved in EW in forests or cropland areas, including the travel of weathering products towards the oceans (panel A), along with a more detailed representation of the silicate minerals dissolution in the soil system (panel B).



## Chapter 4 - EW Modeling: rock-dissolution reactions coupled to plant, soil moisture and carbon dynamics

EW is recognized as one of the most effective NCS to counteract global warming and achieve the 1.5 °C climate target fixed by the Paris agreement [15,30]. However, as widely explored in the previous chapters, this technique involves many different processes in soil, such as those related to hydrology and soil biogeochemistry. Therefore, an accurate knowledge of their interaction is needed before thinking to apply it at large scales in natural environments. It is known that chemical weathering, and hence EW, is favored under hot and humid climate conditions since the presence of soil moisture is crucial to produce high mineral dissolution rates [15,98]. This process is also well affected by a high soil acidity, due to the fact that a great activity of  $H^+$  ions enhances the minerals dissolution [19]. The resulting processes thus form an interestingly intricate dynamical system defined by soil-plant conditions and forced by hydro-climatic conditions.

It has been also described that field weathering rates are generally much lower than those achieved under laboratory conditions [25,26] and, apart from some pot experiments conducted on agricultural soils and some attempts of reactive transport models, not many efforts have been carried out to extrapolate field weathering rates from

laboratory dissolution rate constants. This, in fact, is not an easy task since in fields there are many uncertainties that in laboratory are not taken into account [21] and that are difficult to be characterized. In this context, models, along with experiments, can give a great help to quantify field weathering rates, by addressing the uncertainties from which they are affected, and to define the impacts of hydroclimatic fluctuations on the biogeochemical processes.

To this regard, this chapter describes a complex mathematical model, presented in Cipolla, *et al.* [31], coupling the key ecohydrological and biogeochemical aspects of EW to predict both carbon sequestration and increased nutrient availability in soil water. The model consists of some interconnected components in terms of related differential equations describing the mass balance and the chemical reactions of the involved elements. Particular attention is paid to the soil moisture-soil pH dynamics, their connections to plant growth [124], as well as the relevance of the cation exchange process and plants uptake/release of ions on soil chemistry and weathering rate. The long-term role of hydrological processes on EW is captured by stochastic rainfall forcing which induces multiple combinations of wetting and drying phases which in time are responsible for the averaged weathering rates. The model can be forced with either actual precipitation measurements or with stochastic precipitation for long term simulations (e.g., Porporato, *et al.* [125]). The main motivation that inspired the development of this model was to understand the long-term role of hydrologic (i.e., soil

moisture) variability, coupled to plant, organic matter and cation exchange dynamics on olivine weathering. The model is an attempt to go beyond the existing reactive transport models since, in many cases, not all the processes among plants dynamics, soil biogeochemistry, fluctuations in hydrological forcing and EW, are considered at the same time and with a consistent degree of complexity. Indeed, the model tries to explicitly including the interactions between biotic and abiotic soil processes, while capturing long-term dynamics and climate scenarios uncertainties with explicit inclusion of stochastic hydroclimatic forcing within an agile and relatively parsimonious modeling framework. In the following sections, the equations that compose the model are described in detail and, after that, a reduced-order version of the model and a scheme of its resolution are provided.

## 4.1 Modeling scheme

The weathering process is strongly influenced by surface hydrological processes. To this regard, Figure 32 highlights the main interactions with reference to the main model components, where the soil moisture dynamics resulting from the interaction between rainfall, soil and vegetation, influence soil biogeochemistry (i.e. the organic matter decomposition and the dissolved ions concentration in soil water), plants dynamics (i.e. uptake/release of ions which in turn regulate pH levels in soil) and the olivine weathering rates.

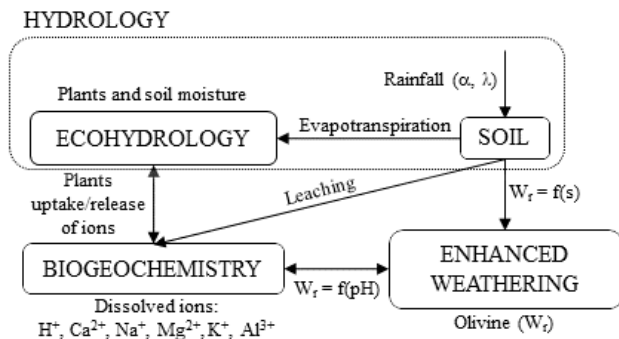


Figure 32 - General scheme of the main model components and their interactions. The figure is taken from Cipolla, et al. [31].

To account for long term hydrologic variability in present and future climates, a probabilistic rainfall description is used, where the rainfall characteristics, namely the average storm depth and frequency, are prescribed. For the sake of simplicity, the soil and vegetation parameters, such as the soil porosity, the typical water retention curve parameters, the cation exchange capacity parameters and the added litter from vegetation, are also given. A more detailed description of all the parameters of the model is provided in the next chapter, which is specifically devoted to the applications. Referring to a unit ground area of homogeneous soil comprising the root zone, the processes are resolved typically at a daily time scale. Figure 33 shows a flow chart representative of the model structure. The central role of soil moisture on the

whole system is clearly evident. Plants also play a relevant role on weathering, since the dissolved ions concentrations are regulated on the base of hydrological fluxes (i.e. leaching and evapotranspiration) and plants uptake/release of ions.

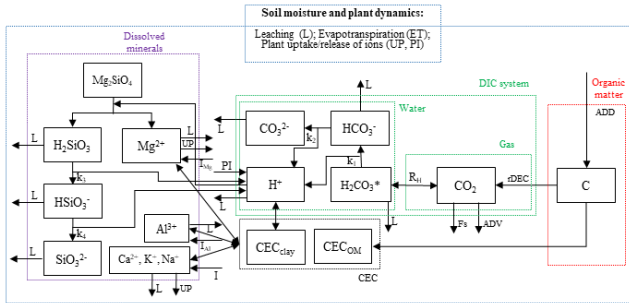


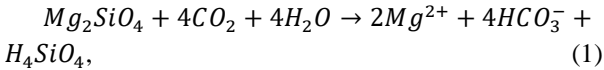
Figure 33 - Flow chart of the involved fluxes in olivine weathering process. The figure is taken from Cipolla, et al. [31].

The different components of the model are highlighted by colored boxes in Figure 33. The “organic matter” component is related to the balance of soil organic carbon, which is one of the  $CO_2$  sources in the system. The dissolved inorganic carbon (DIC) component, called “DIC system”, includes the  $CO_2$  in the gas phase and the part of it that reacts with water. The “Dissolved Minerals” component is related to all the dissolved elements which do not contain carbon, including the products of olivine dissolution (i.e. silicates and  $Mg^{2+}$ ). The cation exchange capacity (“CEC” component) describes the equilibrium

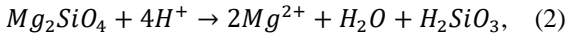
exchanges between soil organic and inorganic colloids and the dissolved ions.

#### 4.1.1 Olivine weathering reactions and balance

The olivine weathering reaction (i.e., between olivine and CO<sub>2</sub>) can be written as follows:



or, to make the dependence on pH explicit, as in [126]:



according to which one mole of olivine reacts with four moles of H<sup>+</sup> ions and results in two moles of Mg<sup>2+</sup> and one mole of silicic acid (H<sub>2</sub>SiO<sub>3</sub>).

The dissolution rate of olivine particles, expressed in number of moles of olivine per unit of reactive surface and per unit of time [21], is a function of soil moisture and pH [106,118,127],

$$W_r(s, pH) = s k_{sil} [H^+] \left( 1 - \frac{\theta}{k_{eq}} \right), \quad (3)$$

where  $k_{sil}$  is the dissolution rate constant of Forsterite [100]. To represent an average weathering rate at the Darcy scale considered here, such constant can be calibrated so as to obtain weathering rates of the same order of magnitude

as those presented by Renforth, *et al.* [25] and ten Berge, *et al.* [26] (about  $10^{-11}$  mol m<sup>-2</sup> s<sup>-1</sup>), which are related to soil samples extracted from field. The linear dependence between weathering rate and soil moisture,  $s$ , is justified by the fact that soil moisture influences the fraction of surface areas of olivine particles exposed to weathering [98]. The dependence between weathering rate and pH is also defined by the ion activity product  $\theta$ , which is the ratio between the product and reactant ions concentrations, elevated to their stoichiometric coefficients, in the chemical reaction (2). The equilibrium constant of reaction (2),  $k_{eq}$ , is from Morel and Hering [126],

$$\theta = \frac{[Mg^{2+}]^{\frac{1}{2}} [H_2SiO_3]^{\frac{1}{4}}}{[H^+]}. \quad (4)$$

Forsterite dissolution in soils strongly depends on temperature. The dissolution rate constants for various silicate minerals reported in Lasaga [100] are related to a constant and ideal temperature (i.e., 25 °C) achieved in laboratory. However, in field there is a strong seasonal variability of soil temperature that affects silicates dissolution dynamics. The temperature dependence of  $k_{sil}$  may be modeled through Arrhenius equation [100],

$$k_{sil} = Ae^{-\frac{E_{\theta}}{RT}}, \quad (5)$$

where  $E_{\theta}$ , expressed in  $kJ\ mol^{-1}$  is the activation energy of the dissolution reaction, which in the case of

Forsterite is assumed to be equal to 38 [100], and  $R$  is the universal gas constant, equal to  $8.314 \text{ J mol}^{-1}\text{K}^{-1}$ .

To account for the particle size distribution resulting from grinding operations, an effective diameter,  $\phi$ , is considered, which can be defined as the mean diameter of a particle size distribution. This is consistent with the observation that the difference between the weathering rate integrated to the particle size distribution and the one calculated by only considering a single effective diameter is very low. This happens because particles with a diameter larger than the effective diameter are characterized by a higher reactive surface area, in the hypothesis that they are perfect spheres, resulting in a higher pH increase at a certain time-step and in a lower weathering rate than the one related to the effective diameter (due to the higher pH). Since an opposite behavior characterizes those particles having a diameter lower than the effective diameter, weathering rates of higher and lower particles diameters tend to compensate, justifying the adoption of an effective diameter. The reduction of the effective diameter can be modeled as the product between the weathering rate and the molar volume of olivine  $V_M$  [100],

$$\frac{d\phi}{dt} = -W_r(s, pH)V_M. \quad (6)$$

#### 4.1.2 CO<sub>2</sub> source

The CO<sub>2</sub> that reacts with olivine comes partly from the atmosphere (see section 4.1.3) and partly from the respiration component of the soil organic matter decomposition. Furthermore, the CO<sub>2</sub> in the gas phase of soil pores comes in part from the autotrophic respiration, which is linked to the products of respiration by roots and can range between 20 and 60 % of the total respiration component [128]. The total soil respiration is connected to mass balance of organic matter as [125,129],

$$\frac{dc}{dt} = ADD - rDEC, \quad (7)$$

where (Figure 33) *ADD* is the added carbon (e.g., litterfall, organic amendment) and *rDEC* is the fraction of decomposed carbon that goes into respiration. The *ADD* term can be either constant or a time-series. The term *DEC* is assumed to linearly depend on the carbon concentration in soil, *C*, and on the carbon concentration of the microbial biomass, *C<sub>b</sub>*, here assumed constant,

$$DEC = k_{dec} f_d(s) C C_b, \quad (8)$$

where  $k_{dec}C_b$  is a first-order kinetic parameter representative of the carbon consumption and  $f_d(s)$  is a non-dimensional factor expressing the effects of soil moisture on carbon decomposition [125],

$$f_d(s) = \begin{cases} \frac{s}{s_{fc}}, & s \leq s_{fc} \\ \frac{s_{fc}}{s}, & s > s_{fc} \end{cases}. \quad (9)$$

### 4.1.3 CO<sub>2</sub> reactions and balance in water

The CO<sub>2</sub> in the gas phase quickly reaches equilibrium with the dissolved CO<sub>2</sub> in the soil water, according to Henry's law (eq. 10). In general, the total concentration of dissolved CO<sub>2</sub>, defined as [H<sub>2</sub>CO<sub>3</sub>\*], can be expressed as the product of the Henry's constant ( $K_H$ ) and the partial pressure of CO<sub>2</sub> ( $P_{CO_2}$ ). The term [H<sub>2</sub>CO<sub>3</sub>\*] was introduced since only a part of the dissolved CO<sub>2</sub> reacts with water and creates the carbonic acid (H<sub>2</sub>CO<sub>3</sub>), as it is expressed by equation (11),

$$[H_2CO_3^*] = K_H P_{CO_2}, \quad (10)$$

$$[H_2CO_3^*] = [H_2CO_3] + CO_{2,aq}. \quad (11)$$

The balance of gas plus dissolved CO<sub>2</sub> in the soil can be written as,

$$\frac{dCO_2}{dt} = rDEC - F_s - R_H - ADV. \quad (12)$$

The input of CO<sub>2</sub> in the DIC component is the output term of the organic matter component  $rDEC$ , described in section 4.1.1, assuming that it contains both heterotrophic and autotrophic respiration components. The term  $F_s$  represents the amount of CO<sub>2</sub> released to the atmosphere due to soil respiration,  $R_H$  is the mass flux of CO<sub>2</sub> due to the equilibrium of the gas-liquid phases, while  $ADV$  is the advection flux of CO<sub>2</sub>, meaning the CO<sub>2</sub> entering the soil during the drying process and out of the soil during the wetting process. According to Daly, *et al.* [130],  $F_s$  can be estimated through the Fick's law, considering a one-dimensional flow,

$$F_s = D \frac{CO_2 - CO_{2,atm}}{\frac{z_r}{2}}, \quad (13)$$

where  $D$  is the  $CO_2$  diffusivity in the soil, while  $CO_{2,atm}$  is the atmospheric  $CO_2$  concentration and  $Z_r/2$  is the average length of the diffusion path.  $D$  can be evaluated as a function of the air-filled porosity, which summed to soil moisture equals 1, and the total porosity,  $n$ , [131],

$$D = D_0 \frac{(1-s)^{\frac{10}{3}}}{n^2}, \quad (14)$$

where the term  $D_0$  is the free-air diffusion coefficient of  $CO_2$ . The term  $ADV$  can be estimated through the following equations,

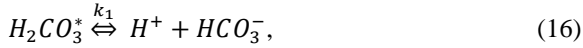
$$ADV = \begin{cases} n Z_r \frac{ds}{dt} CO_{2,atm}, & \frac{ds}{dt} < 0 \\ n Z_r \frac{ds}{dt} CO_{2,air}, & \frac{ds}{dt} > 0 \end{cases} \quad (15)$$

During soil drying, air with  $CO_{2,atm}$  enters the soil pores; during wetting, part of the soil air at  $CO_{2,air}$  concentration is pumped out the system.

#### 4.1.4 Differential balance equations of ions in water

##### 4.1.4.1 Carbonate ions and pH balance equations

The DIC component regulates the time evolution of soil pH and in turn the weathering reaction. The carbonic acid produced by the CO<sub>2</sub> dissolution rapidly dissociates in its deprotonated forms,



These two reactions are strictly connected to the weathering reaction (2) since they provide the H<sup>+</sup> ions that react with olivine. Another source of H<sup>+</sup> ions is the self-ionization of water,



Based on the chemical reactions (16), (17) and (18), the molar balance equations for the “DIC system” per unit ground area can be written as,

$$n Z_r \frac{ds[H_2CO_3^*]}{dt} = -L_{H_2CO_3^*} - R_1 + R_H, \quad (19)$$

$$n Z_r \frac{ds[HCO_3^-]}{dt} = -L_{HCO_3^-} + R_1 - R_2, \quad (20)$$

$$n Z_r \frac{ds[CO_3^{2-}]}{dt} = -L_{CO_3^{2-}} + R_2, \quad (21)$$

$$n Z_r \frac{ds[H^+]}{dt} = PI + RI - L_{H^+} + R_1 + R_2 + R_3 + R_w + 3R_{Al^{3+}} - W_{bg} - 4W_{oliv} - \frac{dx_{H_{OM}^+}}{dt} - \frac{dx_{H_{clay}^+}}{dt}, \quad (22)$$

$$n Z_r \frac{ds[OH^-]}{dt} = -L_{OH^-} + R_w. \quad (23)$$

Equation (22) is very important for the model since it is representative of pH time dynamics. The *PI* (*Plant Input*) term stands for the input concentration of  $H^+$  ions from vegetation, while the *RI* (*Rainfall Input*) term represents the input of  $H^+$  connected to the infiltration rate. The term  $W_{bg}$  is the background weathering, illustrative of the  $H^+$  losses due to naturally present soil minerals, excluding olivine, while the  $H^+$  losses due to olivine weathering are represented by the term  $W_{oliv}$ . The two time derivatives of  $x_{H_{OM}^+}$  and  $x_{H_{clay}^+}$  are related to the cation exchanges of dissolved  $H^+$  with soil organic and clay colloids. The terms  $R_j$  of equations (19-23) are the mass fluxes of the dissolved minerals due to the related chemical reactions (the subscripts of the terms  $R_j$  are the same of those of the equilibrium constants in the corresponding reactions). DIC ions are all affected by leaching, generally written as,

$$L_X = \frac{L(s)}{s n Z_r} [X], \quad (24)$$

where  $[X]$  indicates the concentration in solution of the dissolved ion of interest.

The passive uptake of macro-nutrients, such as magnesium, calcium, and potassium, and of the micro-nutrient sodium is here modeled as proportional to the transpiration rate,  $T(s)$ , [125],

$$UP_X = \frac{T(s)}{s n Z_r} [X], \quad (25)$$

Since plants tend to maintain a neutral charge [19], if they take up from the soil water more cations than anions, they release  $H^+$  ions to balance the charges. The release of plant  $H^+$  can thus be calculated based on the uptake of cations and their corresponding valence as,

$$PI = 2UP_{Mg^{2+}} + 2UP_{Ca^{2+}} + UP_{K^+} + UP_{Na^+}. \quad (26)$$

Typically, rain is characterized by a slightly acidic pH (about 5.6) because of the presence of carbonic acid due to the chemical reaction between  $CO_2$  and water in the atmosphere [132]. Therefore, the term  $RI$  can be written as proportional to the dimensionless infiltration rate,  $I(s)$ , defined by the soil water balance (see section 4.1.4), and to the  $H^+$  concentration at a pH level of 5.6,

$$RI = \frac{I(s)}{s n Z_r} 10^{-5.6}, \quad (27)$$

The weathering of all naturally present soil minerals is accounted for in equation (22) by the background

weathering,  $W_{bg}$ . The latter groups in a single sink term the consumption of  $H^+$  by the dissolution of various minerals,

$$W_{bg} = s k_{bg} [H^+] A(d_{bg}) \frac{f_{bg} \rho_b (1-n) Z_r}{\rho_{bg} V_{bg}}, \quad (28)$$

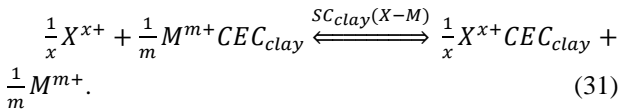
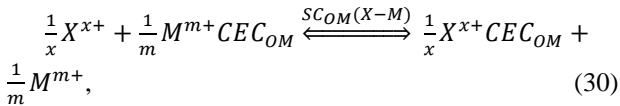
which is proportional to the reactive surface areas of the mineral particles (the product between soil moisture,  $s$ , and the geometric surface area of particles,  $A(d_{bg})$ ), the effective dissolution rate constant,  $k_{bg}$ , the  $H^+$  concentration and the mass of the minerals in the soil, which can be estimated, for the sake of simplicity, as a percentage of the total mass of the soil. The effective dissolution rate constant and the geometric surface area should take into account the composition of the soil, in particular the minerals contributing more to the consumption of  $H^+$ . For example, pedogenic carbonate minerals (i.e.,  $MgCO_3$  and  $CaCO_3$ ) can be the dominant  $H^+$  sink in very dry soils, due to the low leaching of  $CO_3^{2-}$ . In this case, the effective dissolution rate constant should reflect more the dissolution of carbonates, rather than silicates. In general,  $W_{bg}$  is a flexible term that should be calibrated based on the estimated composition of the soil under study.

The term  $W_{oliv}$ , representative of the  $H^+$  loss due to olivine dissolution, can be written as,

$$W_{oliv} = A(\phi) W_r \frac{M_{oliv}}{\rho_{oliv} V_{oliv}}. \quad (29)$$

By writing  $W_r$  as in equation (3), the product between soil moisture and the geometric surface area of olivine particles is recognized as the reactive surface area, as explained by Sverdrup and Warfvinge [98]. In eq. (22),  $W_{oliv}$  is multiplied by a coefficient equal to 4, since one mole of olivine reacts with four moles of  $H^+$ , as highlighted in the reaction (2).

The last two terms of equation (22) are related to the cation exchanges between soil colloids and solution. The CEC is a measure of the amount of moles of cations that can be adsorbed on soil colloids (due to their negatively charged surface [133]) and can be described by the following equilibrium reactions, where  $X$  and  $M$  are two generic cations that are dissolved and adsorbed, respectively. The terms  $x$  and  $m$  are the respective charges of the two cations.



The total CEC of the soil includes the organic matter ( $CEC_{OM}$ ) and the clay components ( $CEC_{clay}$ ), which represent, respectively, the exchanges occurring in organic and inorganic sites of the soil, better known as organic and clay colloids.

The first is evaluated as the product between the typical specific CEC of organic colloids [19] and the total mass of organic carbon in the soil, obtained through equation (7). Similarly, the  $CEC_{clay}$  is the product between the typical specific CEC of clay colloids and the total mass of clay in the soil, fixed as a percentage of the total mass of the soil. Here, the exchange of  $H^+$ ,  $Na^+$ ,  $Ca^{2+}$ ,  $K^+$ ,  $Al^{3+}$  and  $Mg^{2+}$  is explicitly considered because of their widespread presence in soils and because  $K^+$ ,  $Ca^{2+}$  and  $Mg^{2+}$  are the most common macro-nutrients for plants. Depending on the exchange processes and particularly on the amount of  $H^+$  adsorbed on soil colloids, there is a change in soil pH which influences the olivine weathering reaction. The amount of adsorbed ions in the soil sites is computed based on the Gapon equation [134], which considers equilibrium reactions between dissolved and adsorbed ions and assumes a fixed number of exchanges adsorption sites [135]. With reference to the binary exchange between  $H^+$  and  $Ca^{2+}$ , one can write the mass of exchanged hydrogen ions in the organic and clay colloids as,

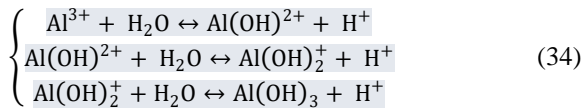
$$x_{H_{OM}^+} = \frac{CEC_{OM} - x_{Na_{OM}^+} - x_{Mg_{OM}^{2+}} - x_{K_{OM}^+} - x_{Al_{OM}^{3+}}}{1 + \frac{1}{SC_{OM}(H^+ - Ca^{2+}) \frac{[H^+]^1}{[Ca^{2+}]^2}}}, \quad (32)$$

$$x_{H_{clay}^+} = \frac{CEC_{clay} - x_{Na_{clay}^+} - x_{Mg_{clay}^{2+}} - x_{K_{clay}^+} - x_{Al_{clay}^{3+}}}{1 + \frac{1}{SC_{clay}(H^+ - Ca^{2+}) \frac{[H^+]^1}{[Ca^{2+}]^2}}}, \quad (33)$$

In equations (32, 33), the exchanged  $\text{Na}^+$ ,  $\text{K}^+$ ,  $\text{Al}^{3+}$  and  $\text{Mg}^{2+}$  are subtracted to the  $CEC_{OM}$  and  $CEC_{clay}$  since the portions of colloids occupied by these cations cannot be used for the exchange between  $\text{H}^+$  and  $\text{Ca}^{2+}$ . This aspect highlights the competition among all the dissolved ions, in this case  $\text{H}^+$ ,  $\text{Ca}^{2+}$ ,  $\text{Mg}^{2+}$ ,  $\text{K}^+$ ,  $\text{Al}^{3+}$  and  $\text{Na}^+$ , in the neutralization of the negative charges of soil colloids. The terms  $SC_{OM}(\text{H}^+ - \text{Ca}^{2+})$  and  $SC_{clay}(\text{H}^+ - \text{Ca}^{2+})$  are the binary selectivity constants between  $\text{H}^+$  and  $\text{Ca}^{2+}$ , while in square brackets there are the concentrations of dissolved  $\text{H}^+$  and  $\text{Ca}^{2+}$ .

#### 4.1.4.2 Aluminum hydrolysis and exchange

Aluminum hydrolysis represents one of the major  $\text{H}^+$  sources in acid soils [19]. The dissolution of parent materials, such as gibbsite, releases  $\text{Al}^{3+}$  ions in soil water that react as,



If combined, these reactions result in,



The balance of  $Al^{3+}$  can thus be expressed as,

$$nZ_r \frac{ds[Al^{3+}]}{dt} = I_{Al^{3+}} - L_{Al^{3+}} - R_{Al^{3+}} - \frac{dx_{Al_{OM}^{3+}}}{dt} - \frac{dx_{Al_{clay}^{3+}}}{dt}, \quad (36)$$

where  $I_{Al^{3+}}$  represents the input concentration of  $Al^{3+}$  in the system. This is related to the dissolution of parent materials and can be expressed through an expression similar to (28), i.e., as a function of the dissolution rate of the parent material. The output of  $Al^{3+}$  is related to leaching,  $L_{Al^{3+}}$ , while  $R_{Al^{3+}}$  is the mass flux due to the hydrolysis reaction (35). The last two terms of equation (36) are related to the cation exchanges with organic matter and clay colloids. The moles of exchanged  $Al^{3+}$  per unit mass of reactive soil are:

$$x_{Al_{OM}^{3+}} = \frac{CEC_{OM} - x_{H_{OM}^+} - x_{Mg_{OM}^{2+}} - x_{Ca_{OM}^{2+}} - x_{K_{OM}^+}}{\left[ 1 + \frac{1}{SC_{OM}(Al^{3+} - Na^+)^{\frac{1}{3}} [Na^+]^{\frac{1}{3}}} \right]} \quad (37)$$

$$x_{Al_{clay}^{3+}} = \frac{CEC_{clay} - x_{H_{clay}^+} - x_{Mg_{clay}^{2+}} - x_{Ca_{clay}^{2+}} - x_{K_{clay}^+}}{\left[ 1 + \frac{1}{SC_{clay}(Al^{3+} - Na^+)^{\frac{1}{3}} [Na^+]^{\frac{1}{3}}} \right]} \quad (38)$$

#### 4.1.4.3 Nutrients balance equations

The mass balance equations of  $Mg^{2+}$ ,  $Ca^{2+}$ ,  $K^+$  and  $Na^+$  can be written as,

$$nZ_r \frac{ds[Mg^{2+}]}{dt} = I_{Mg^{2+}} - L_{Mg^{2+}} - UP_{Mg^{2+}} + 2W_{oliv} - \frac{dx_{Mg_{OM}^{2+}}}{dt} - \frac{dx_{Mg_{clay}^{2+}}}{dt}, \quad (39)$$

$$nZ_r \frac{ds[Ca^{2+}]}{dt} = I_{Ca^{2+}} - L_{Ca^{2+}} - UP_{Ca^{2+}} - \frac{dx_{Ca_{OM}^{2+}}}{dt} - \frac{dx_{Ca_{clay}^{2+}}}{dt}, \quad (40)$$

$$nZ_r \frac{ds[K^+]}{dt} = I_{K^+} - L_{K^+} - UP_{K^+} - \frac{dx_{K_{OM}^+}}{dt} - \frac{dx_{K_{clay}^+}}{dt}, \quad (41)$$

$$nZ_r \frac{ds[Na^+]}{dt} = I_{Na^+} - L_{Na^+} - UP_{Na^+} - \frac{dx_{Na_{OM}^+}}{dt} - \frac{dx_{Na_{clay}^+}}{dt}, \quad (42)$$

For each of these cations, the input term,  $I$ , includes the atmospheric deposition, the return of cations from plant litter and an input from the dissolution of minerals within the soil. These three terms vary according to different time scales. For instance, the return of cations from vegetation should be linked to the decomposition of the soil litter (i.e., the term DEC), while the input from minerals should be defined based on the corresponding dissolution rates. However, because these inputs are small and the model

looks at the long-term (i.e., the scale of the olivine weathering process), they may be grouped in a single constant. Furthermore,  $Mg^{2+}$  has an additional input due to the weathering of olivine, i.e., one mole of olivine releases two moles of  $Mg^{2+}$  according to reaction (2). For all the ions, losses are represented by leaching, plant uptake and cation exchange terms. The moles of exchanged  $Mg^{2+}$ ,  $K^+$  and  $Na^+$  per unit of mass of reactive soil are related by,

$$x_{Mg_{OM}^{2+}} = \frac{CECOM^{-x} Na_{OM}^+ - x_{H_{OM}^+} - x_{K_{OM}^+} - x_{Al_{OM}^{3+}}}{\left[ 1 + \frac{1}{SC_{OM}(Mg^{2+} - Ca^{2+}) \frac{[Mg^{2+}]}{[Ca^{2+}]}} \right]}, \quad (43)$$

$$x_{Mg_{clay}^{2+}} = \frac{CEC_{clay}^{-x} Na_{clay}^+ - x_{H_{clay}^+} - x_{K_{clay}^+} - x_{Al_{clay}^{3+}}}{\left[ 1 + \frac{1}{SC_{clay}(Mg^{2+} - Ca^{2+}) \frac{[Mg^{2+}]}{[Ca^{2+}]}} \right]}, \quad (44)$$

$$x_{K_{OM}^+} = \frac{CECOM^{-x} H_{OM}^+ - x_{Mg_{OM}^{2+}} - x_{Ca_{OM}^{2+}} - x_{Al_{OM}^{3+}}}{\left[ 1 + \frac{1}{SC_{OM}(K^+ - Na^+) \frac{[K^+]}{[Na^+]}} \right]}, \quad (45)$$

$$x_{K_{clay}^+} = \frac{CEC_{clay}^{-x} H_{clay}^+ - x_{Mg_{clay}^{2+}} - x_{Ca_{clay}^{2+}} - x_{Al_{clay}^{3+}}}{\left[ 1 + \frac{1}{SC_{clay}(K^+ - Na^+) \frac{[K^+]}{[Na^+]}} \right]}, \quad (46)$$

$$x_{Na_{OM}^+} = \frac{CECOM^{-x} H_{OM}^+ - x_{Mg_{OM}^{2+}} - x_{K_{OM}^+} - x_{Al_{OM}^{3+}}}{\left[ 1 + \frac{1}{SC_{OM}(Na^+ - Ca^{2+}) \frac{[Na^+]}{[Ca^{2+}]^{\frac{1}{2}}}} \right]}, \quad (47)$$

$$x_{Na_{clay}^{2+}} = \frac{CEC_{clay} - x_{H_{clay}^+} - x_{Mg_{clay}^{2+}} - x_{K_{clay}^+} - x_{Al_{clay}^{3+}}}{\left[ 1 + \frac{1}{SC_{clay}(Na^+ - Ca^{2+}) \frac{[Na^+]}{[Ca^{2+}]^{\frac{1}{2}}}} \right]}, \quad (48)$$

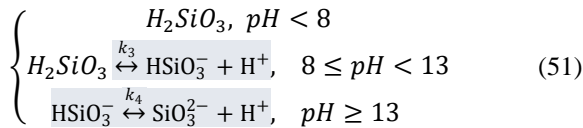
$$CEC_{OM} = x_{H_{OM}^+} + x_{Na_{OM}^+} + x_{Ca_{OM}^{2+}} + x_{Mg_{OM}^{2+}} + x_{K_{OM}^+} + x_{Al_{OM}^{3+}}, \quad (49)$$

$$CEC_{clay} = x_{H_{clay}^+} + x_{Na_{clay}^+} + x_{Ca_{clay}^{2+}} + x_{Mg_{clay}^{2+}} + x_{K_{clay}^+} + x_{Al_{clay}^{3+}}. \quad (50)$$

Equations (49) and (50) define the total CEC of organic and clay colloids as the sum between the total amount of exchanged ions taken into account in our system.

#### 4.1.4.4 Silicates balance equations

The silicic acid dissociation depends on pH. More specifically, if pH is less than 8, silicic acid remains in the form of the undissociated  $H_2SiO_3$ . If pH is within the range 8-13, silicic acid deprotonates in the form of  $HSiO_3^-$ , while if the pH is higher than 13, the second dissociation occurs and silicic acid will also be in the form of  $SiO_3^{2-}$ .



The balance of silicates can be written as,

$$nZ_r \frac{ds[H_2SiO_3]}{dt} = -L_{H_2SiO_3} + W_{oliv} - R_3, \quad (52)$$

$$nZ_r \frac{ds[HSiO_3^-]}{dt} = -L_{HSiO_3^-} + R_3 - R_4, \quad (53)$$

$$nZ_r \frac{ds[SiO_3^{2-}]}{dt} = -L_{SiO_3^{2-}} + R_4. \quad (54)$$

Apart from reaction rates and leaching losses, equation (52) presents a gain of  $H_2SiO_3$  due to the weathering of olivine. It reflects the fact that for one mole of olivine that reacts, one mole of  $H_2SiO_3$  is produced, according to the weathering reaction (2).

#### 4.1.5 Soil moisture dynamics

Soil moisture dynamics for a root zone depth  $Z_r$  is [125],

$$nZ_r \frac{ds}{dt} = I(s, t) - E(s) - T(s) - L(s). \quad (55)$$

The infiltration rate from rainfall,  $I(s, t)$ , is a function of soil moisture and time and is evaluated as the minimum value among the rainfall depth and the amount of water that can be stored in the soil at a certain soil moisture value. Rainfall can be obtained from time-series or modeled as a marked Poisson process, in which the frequency of rainfall events is represented by the parameter  $\lambda$  and the mean rainfall depth by the parameter  $\alpha$  [136]. Bare soil evaporation is  $E(s)$  and the transpiration rate,  $T(s)$ , are

evaluated as in [125]. The term  $L(s)$  is representative of the leakage losses, evaluated as a function of soil moisture, through an exponential law, which includes the hydraulic conductivity at saturation,  $K_s$ , the soil moisture at the field capacity,  $s_{fc}$ , and the pore size distribution index.

## 4.2 Reduced-order model

The equations representative of the biogeochemical, ecohydrological, and EW processes constitute a complex system of equations, which are partly differential and partly algebraic. Several of these equations can be combined to obtain a reduced-order version of the model. In particular, analyzing equations (56) and (57) one can notice that an equation for the total carbon  $C_t$  is obtained by combining equations (12), (19), (20) and (21),

$$C_{DIC} = [H_2CO_3^*] + [HCO_3^-] + [CO_3^{2-}], \quad (56)$$

$$C_t = [CO_{2,air}] + C_{DIC}, \quad (57)$$

$$\frac{dC_t}{dt} = rDEC - F_s - ADV - L_{C_{DIC}}, \quad (58)$$

which allows to simplify the equilibrium terms,  $R_j$ , and reduce four equations into only one.

The equilibrium constants of the dissolved inorganic carbon reactions can be written as [15],

$$K_{H,ad} = \frac{[H_2CO_3^*]}{[CO_{2,air}]}, \quad (59)$$

$$k_1 = \frac{[HCO_3^-][H^+]}{[H_2CO_3^*]}, \quad (60)$$

$$k_2 = \frac{[CO_3^{2-}][H^+]}{[HCO_3^-]}. \quad (61)$$

In equation (59) the ratio between the concentration of carbonic acid and the CO<sub>2</sub> concentration in the gas phase is the dimensionless Henry's constant, equal to 0.83. The equilibrium constants of the first and the second order of carbonic acid dissociation are indicated with  $k_1$  and  $k_2$ , respectively. By combining the expressions (59-61), it is possible to write each element of the dissolved inorganic carbon as a fraction of  $C_{DIC}$  [137],

$$[H_2CO_3^*] = \alpha_0 C_{DIC}, \quad (62)$$

$$[HCO_3^-] = \alpha_1 C_{DIC}, \quad (63)$$

$$[CO_3^{2-}] = \alpha_2 C_{DIC}, \quad (64)$$

where the coefficients  $\alpha_0$ ,  $\alpha_1$  and  $\alpha_2$  depend on pH, as shown by the following equations,

$$\alpha_0 = \left( 1 + \frac{k_1}{[H^+]} + \frac{k_1 k_2}{[H^+]^2} \right)^{-1}, \quad (65)$$

$$\alpha_1 = \left( \frac{[H^+]}{k_1} + 1 + \frac{k_2}{[H^+]} \right)^{-1}, \quad (66)$$

$$\alpha_2 = \left( \frac{[H^+]^2}{k_1 k_2} + \frac{[H^+]}{k_2} + 1 \right)^{-1}. \quad (67)$$

Another important parameter is the alkalinity,

$$A = [HCO_3^-] + 2[CO_3^{2-}] - [H^+] - 3[Al^{3+}] + [OH^-], \quad (68)$$

that considering equations (62-64) can be written as,

$$A = C_{DIC}(\alpha_1 + 2\alpha_2) - [H^+] - 3[Al^{3+}] + [OH^-], \quad (69)$$

Since in the mass balance differential equations related to  $H^+$  (eq. 22) and  $Al^{3+}$  (eq. 36) there are also the cation exchange capacity terms, the alkalinity expression can be modified by introducing the total  $H^+$  and  $Al^{3+}$  instead of the dissolved  $H^+$  and  $Al^{3+}$ , defined as the sum between the dissolved and adsorbed moles of  $H^+$  and  $Al^{3+}$  in soil colloids,

$$H_t^+ = H^+ + x_{H_{OM}^+} + x_{H_{clay}^+}, \quad (70)$$

$$Al_t^{3+} = Al^{3+} + x_{Al_{OM}^{3+}} + x_{Al_{clay}^{3+}}. \quad (71)$$

The expression for the total alkalinity is thus,

$$A_t = C_{DIC}(\alpha_1 + 2\alpha_2) - [H_t^+] - 3[Al_t^{3+}] + [OH^-], \quad (72)$$

whose balance equation reads:

$$\frac{dA_t}{dt} = -L_{HCO_3^-} - 2L_{CO_3^{2-}} - RI - PI + L_{H^+} - L_{OH^-} + W_{bg} + 4W_{oliv} - 3I_{Al^{3+}} + 3L_{Al^{3+}}. \quad (73)$$

Similarly, the total masses of calcium, magnesium, potassium, sodium and aluminum and the corresponding mass balance differential equations are introduced,

$$Ca_t^{2+} = Ca^{2+} + x_{Ca_{OM}^{2+}} + x_{Ca_{clay}^{2+}}, \quad (74)$$

$$Mg_t^{2+} = Mg^{2+} + x_{Mg_{OM}^{2+}} + x_{Mg_{clay}^{2+}}, \quad (75)$$

$$K_t^+ = K^+ + x_{K_{OM}^+} + x_{K_{clay}^+}, \quad (76)$$

$$Na_t^+ = Na^+ + x_{Na_{OM}^+} + x_{Na_{clay}^+}, \quad (77)$$

$$\frac{dCa_t^{2+}}{dt} = I_{Ca^{2+}} - L_{Ca^{2+}} - UP_{Ca^{2+}}, \quad (78)$$

$$\frac{dMg_t^{2+}}{dt} = I_{Mg^{2+}} - L_{Mg^{2+}} - UP_{Mg^{2+}} + 2W_{oliv}, \quad (79)$$

$$\frac{dK_t^+}{dt} = I_{K^+} - L_{K^+} - UP_{K^+}, \quad (80)$$

$$\frac{dNa_t^+}{dt} = I_{Na^+} - L_{Na^+} - UP_{Na^+}, \quad (81)$$

$$\frac{dAl_t^{3+}}{dt} = I_{Al^{3+}} - L_{Al^{3+}}. \quad (82)$$

The equations for the silicates (52-54) can be condensed into one equation, defining the total silicon in the system as the sum of all the three forms of this element,

$$Si_t = H_2SiO_3 + HSiO_3^- + SiO_3^{2-}, \quad (83)$$

$$\frac{dSi_t}{dt} = -LSi_t + W_{oliv}. \quad (84)$$

### 4.3 Model Summary and Numerical Simulations

At this point, before delving into the simulations, it is useful to take stock and present here a synopsis of the model. The time dynamics of the total carbon, the total alkalinity and the mass of the total calcium, sodium, magnesium, potassium, aluminum and silicates are described by the following mass balance differential equations.

$$\left\{ \begin{array}{l} \frac{dC_t}{dt} = rDEC - F_s - ADV - L_{CDIC} \\ \frac{dA_t}{dt} = -L_{HCO_3^-} - 2L_{CO_3^{2-}} - RI - PI + \\ \quad + L_{H^+} - L_{OH^-} + W_{bg} + \\ \quad + 4W_{oliv} - 3I_{Al^{3+}} + 3L_{Al^{3+}} \\ \frac{dCa_t^{2+}}{dt} = I_{Ca^{2+}} - L_{Ca^{2+}} - UP_{Ca^{2+}} \\ \frac{dMg_t^{2+}}{dt} = I_{Mg^{2+}} - L_{Mg^{2+}} - UP_{Mg^{2+}} + \\ \quad + 2W_{oliv} \\ \frac{dNa_t^+}{dt} = I_{Na^+} - L_{Na^+} - UP_{Na^+} \\ \frac{dK_t^+}{dt} = I_{K^+} - L_{K^+} - UP_{K^+} \\ \frac{dAl_t^{3+}}{dt} = I_{Al^{3+}} - L_{Al^{3+}} \\ \frac{dSi_t}{dt} = -L_{Si_t} + W_{oliv} \end{array} \right. \quad (85)$$

The system of equations (85) is here solved in an explicit way with a forward scheme, once the initial

conditions for  $C_t$ ,  $A_t$ ,  $Ca_t^{2+}$ ,  $Mg_t^{2+}$ ,  $Na_t^+$ ,  $K_t^+$ ,  $Al_t^{3+}$  and  $Si_t$  are fixed. The concentration of the considered dissolved ions ( $Ca^{2+}$ ,  $Na^+$ ,  $Mg^{2+}$ ,  $H^+$ ,  $K^+$ ,  $Al^{3+}$ ) and other individual variables are obtained by solving an implicit algebraic system (see section 4.3.1 for the derivation). Both systems may be solved at an hourly time-step since percolation process of the water balance module occur much faster than one day. Then, outcoming variables may be aggregated at the daily scale to look at long-term results. Another resolution way may consist of solving the only water balance module at the hourly time-step, aggregating related results at the daily scale and then solving the organic matter and the whole biogeochemical components at a daily time-step. This certainly allows carrying out long-term simulations in reasonable times.

The initial condition of the total carbon,  $C_t$ , is defined as the sum of the concentrations of  $CO_2$  in the gas phase and of the total dissolved inorganic carbon at the first step (eq. 57). According to Stumm and Morgan [137] it can be fixed equal to  $10^{-6}$  moles  $l^{-1}$ . This value is also used to assess the initial concentration of  $CO_2$  in the gas phase, through eq. (59). The total alkalinity,  $A_t$ , at the first step is defined through eq. (72), as a function of the initial condition of  $C_{DIC}$ ,  $[H^+]$ ,  $[Ca^{2+}]$ ,  $[Na^+]$ ,  $[K^+]$ ,  $[Al^{3+}]$  and  $[Mg^{2+}]$ . Equations (66) and (67) highlight that the terms  $\alpha_1$  and  $\alpha_2$  are a function of  $[H^+]$ , thus of the initial soil pH which, as a generic value can be fixed equal to 7. The amount of adsorbed moles of  $[H^+]$  on organic and clay colloids,  $x_{H_{OM}^+}$  and  $x_{H_{clay}^+}$ , at the first step, can be calculated by solving an

implicit system constituted by the algebraic equations related to the CEC component, thus by solving the system (86) excluding equations (4), (57), (59) and (72). Solving this algebraic implicit system results in the evaluation of  $x_{Ca_{OM}^{2+}}$ ,  $x_{Ca_{clay}^{2+}}$ ,  $x_{Mg_{OM}^{2+}}$ ,  $x_{Mg_{clay}^{2+}}$ ,  $x_{Na_{OM}^+}$ ,  $x_{Na_{clay}^+}$ ,  $x_{K_{OM}^+}$ ,  $x_{K_{clay}^+}$ ,  $x_{Al_{OM}^{3+}}$  and  $x_{Al_{clay}^{3+}}$  at the first step; therefore, the initial  $Al_t^{3+}$ ,  $Ca_t^{2+}$ ,  $Mg_t^{2+}$ ,  $K_t^+$  and  $Na_t^+$  may be defined on the base of equations (71, 74-77). With reference to the initial total silicon in the system, a basic value of  $10^{-11}$  moles  $l^{-1}$  may be taken into account.

A schematic representation of the numerical resolution of the model is provided in Figure 34. At each time-step, after solving the soil water balance, forced with a stochastic rainfall, the output soil moisture, infiltration, leaching and evapotranspiration rates are coupled to the organic carbon balance, to obtain the decomposition rate and organic carbon concentration. For the sake of simplicity, the characteristics of vegetation are considered fixed in time; thus, the amount of litter added to the soil (*ADD*) is assumed as constant under a certain climate scenario (fixed values of  $\alpha$  and  $\lambda$ ). The output variables of these two balances are used to solve the explicit system. Once the initial conditions are fixed, the explicit system is firstly solved and its output variables, namely  $C_t$ ,  $A_t$ ,  $Ca_t^{2+}$ ,  $Mg_t^{2+}$ ,  $Na_t^+$ ,  $K_t^+$ ,  $Al_t^{3+}$  and  $Si_t$ , can be passed to the implicit algebraic system (86). Once the implicit system is solved, some of its output variables, such as the dissolved ions concentrations, can be used to solve the explicit system at the next time-step, since it is solved with a forward scheme.

This goes on until the simulation end time is reached. It is worth recalling that the explicit system can be solved independently from the implicit one. Indeed, the resolution of the implicit part of the model can be carried out to obtain the time-series of individual variables (not combined), such as those of pH,  $[Mg^{2+}]$ ,  $[Na^+]$ ,  $[K^+]$ ,  $[Al^{3+}]$  and  $[Ca^{2+}]$ , that are very useful to see the effects of olivine on soil chemistry which could reflect on land management. The time-series of  $[HCO_3^-]$  and  $[CO_3^{2-}]$  are very relevant as well, since they can be used to calculate the mass of carbon, translated into the equivalent mass of  $CO_2$  on the base of the mass of carbon contained in a unit mass of  $CO_2$ , which is sequestered by olivine in a certain amount of time.

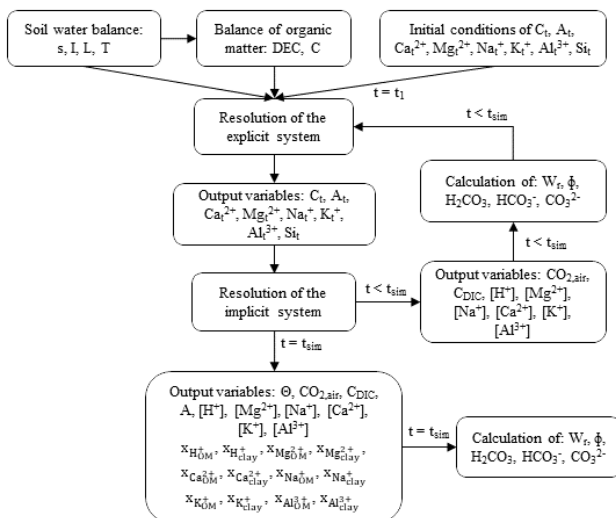


Figure 34 - Schematic representation of the numerical resolution of the model. After solving the soil water and the organic matter balances, their output variables are passed to the explicit system. The simulation ends once the simulation end time is reached. The figure is taken from Cipolla, et al. [31].

### 4.3.1 Implicit algebraic system derivation

The implicit system (86) consists of 22 equations in 22 unknown terms, namely  $\theta$ ,  $CO_{2,air}$ ,  $C_{DIC}$ ,  $A$ ,  $[H^+]$ ,  $[Mg^{2+}]$ ,  $[Na^+]$ ,  $[K^+]$ ,  $[Al^{3+}]$ ,  $[Ca^{2+}]$ ,  $x_{H_{OM}^+}$ ,  $x_{H_{clay}^+}$ ,  $x_{Mg_{OM}^{2+}}$ ,  $x_{Mg_{clay}^{2+}}$ ,  $x_{Ca_{OM}^{2+}}$ ,  $x_{Ca_{clay}^{2+}}$ ,  $x_{Na_{OM}^+}$ ,  $x_{Na_{clay}^+}$ ,  $x_{K_{OM}^+}$ ,  $x_{K_{clay}^+}$ ,  $x_{Al_{OM}^{3+}}$  and  $x_{Al_{clay}^{3+}}$ . It has been derived by putting together

many of the model equations and, for the sake of a better readability, is presented as,

$$\left\{ \begin{array}{l}
 \theta = \frac{[Mg^{2+}]^{\frac{1}{2}} [H_2SiO_3]^{\frac{1}{4}}}{[H^+]} \\
 C_t = [CO_{2,air}] + C_{DIC} \\
 K_{H,ad} = \frac{[H_2CO_3^*]}{[CO_{2,air}]} \\
 A_t = C_{DIC}(\alpha_1 + 2\alpha_2) - [H_t^+] - 3[Al_t^{3+}] + [OH^-] \\
 H_t^+ = H^+ + x_{H_{OM}^+} + x_{H_{clay}^+} \\
 Ca_t^{2+} = Ca^{2+} + x_{Ca_{OM}^{2+}} + x_{Ca_{clay}^{2+}} \\
 Mg_t^{2+} = Mg^{2+} + x_{Mg_{OM}^{2+}} + x_{Mg_{clay}^{2+}} \\
 Na_t^+ = Na^+ + x_{Na_{OM}^+} + x_{Na_{clay}^+} \\
 K_t^+ = K^+ + x_{K_{OM}^+} + x_{K_{clay}^+} \\
 Al_t^{3+} = Al^{3+} + x_{Al_{OM}^{3+}} + x_{Al_{clay}^{3+}} \\
 x_{H_{OM}^+} = \frac{CEC_{OM} - x_{Na_{OM}^+} - x_{Mg_{OM}^{2+}} - x_{K_{OM}^+} - x_{Al_{OM}^{3+}}}{\left[ 1 + \frac{1}{SC_{OM}(H^+ - Ca^{2+}) \frac{[H^+]}{[Ca^{2+}]^{\frac{1}{2}}}} \right]} \\
 x_{H_{clay}^+} = \frac{CEC_{clay} - x_{Na_{clay}^+} - x_{Mg_{clay}^{2+}} - x_{K_{clay}^+} - x_{Al_{clay}^{3+}}}{\left[ 1 + \frac{1}{SC_{clay}(H^+ - Ca^{2+}) \frac{[H^+]}{[Ca^{2+}]^{\frac{1}{2}}}} \right]}
 \end{array} \right.$$

$$\left\{ \begin{array}{l}
 x_{Mg_{OM}^{2+}} = \frac{CEC_{OM} - x_{Na_{OM}^+} - x_{H_{OM}^+} - x_{K_{OM}^+} - x_{Al_{OM}^{3+}}}{\left[ 1 + \frac{1}{SC_{OM}(Mg^{2+} - Ca^{2+})} \frac{[Mg^{2+}]}{[Ca^{2+}]} \right]} \\
 x_{Mg_{clay}^{2+}} = \frac{CEC_{clay} - x_{Na_{clay}^+} - x_{H_{clay}^+} - x_{K_{clay}^+} - x_{Al_{clay}^{3+}}}{\left[ 1 + \frac{1}{SC_{clay}(Mg^{2+} - Ca^{2+})} \frac{[Mg^{2+}]}{[Ca^{2+}]} \right]} \\
 x_{Na_{OM}^+} = \frac{CEC_{OM} - x_{H_{OM}^+} - x_{Mg_{OM}^{2+}} - x_{K_{OM}^+} - x_{Al_{OM}^{3+}}}{\left[ 1 + \frac{1}{SC_{OM}(Na^+ - Ca^{2+})} \frac{[Na^+]}{[Ca^{2+}]^{\frac{1}{2}}} \right]} \\
 x_{Na_{clay}^{2+}} = \frac{CEC_{clay} - x_{H_{clay}^+} - x_{Mg_{clay}^{2+}} - x_{K_{clay}^+} - x_{Al_{clay}^{3+}}}{\left[ 1 + \frac{1}{SC_{clay}(Na^+ - Ca^{2+})} \frac{[Na^+]}{[Ca^{2+}]^{\frac{1}{2}}} \right]} \\
 x_{K_{OM}^+} = \frac{CEC_{OM} - x_{H_{OM}^+} - x_{Mg_{OM}^{2+}} - x_{Na_{OM}^+} - x_{Al_{OM}^{3+}}}{\left[ 1 + \frac{1}{SC_{OM}(K^+ - Ca^{2+})} \frac{[K^+]}{[Ca^{2+}]^{\frac{1}{2}}} \right]}
 \end{array} \right.$$

$$\left. \begin{aligned}
 x_{K_{clay}^+} &= \frac{CEC_{clay} - x_{H_{clay}^+} - x_{Mg_{clay}^{2+}} - x_{Na_{clay}^+} - x_{Al_{clay}^{3+}}}{\left[ 1 + \frac{1}{SC_{clay}(K^+ - Ca^{2+}) \frac{[K^+]}{[Ca^{2+}]^{\frac{1}{2}}}} \right]} \\
 x_{Al_{OM}^{3+}} &= \frac{CEC_{OM} - x_{H_{OM}^+} - x_{Mg_{OM}^{2+}} - x_{Na_{OM}^+} - x_{K_{OM}^+}}{\left[ 1 + \frac{1}{SC_{OM}(Al^{3+} - Ca^{2+}) \frac{[Al^{3+}]^{\frac{1}{3}}}{[Ca^{2+}]^{\frac{1}{2}}}} \right]} \\
 x_{Al_{clay}^{3+}} &= \frac{CEC_{clay} - x_{H_{clay}^+} - x_{Mg_{clay}^{2+}} - x_{Na_{clay}^+} - x_{K_{clay}^+}}{\left[ 1 + \frac{1}{SC_{clay}(Al^{3+} - Ca^{2+}) \frac{[Al^{3+}]^{\frac{1}{3}}}{[Ca^{2+}]^{\frac{1}{2}}}} \right]} \\
 CEC_{OM} &= x_{H_{OM}^+} + x_{Na_{OM}^+} + x_{Ca_{OM}^{2+}} + x_{Mg_{OM}^{2+}} + \\
 &\quad + x_{K_{OM}^+} + x_{Al_{OM}^{3+}} \\
 CEC_{clay} &= x_{H_{clay}^+} + x_{Na_{clay}^+} + x_{Ca_{clay}^{2+}} + x_{Mg_{clay}^{2+}} + \\
 &\quad + x_{K_{clay}^+} + x_{Al_{clay}^{3+}}
 \end{aligned} \right\} \quad (86)$$

### 4.3.2 The role of wetness on weathering rate

To shed light on the importance of soil moisture, plants and CEC, on weathering, some timeseries resulting from numerical solutions of the model were analyzed. In this and the following two sections, some general characteristics of the model are analyzed, with the aim to quantify the role of some key parameters on EW. More detailed simulations are presented, instead, in Chapter 5.

A first important result, shown in Figure 35, is that the relationship between olivine weathering rate and soil moisture is not single-valued. This is due to the nonlinearities in the relationship between soil moisture and soil biogeochemistry, i.e., the soil water balance and the implicit system of equations (86). The non-linear relationship between weathering rate and soil moisture (Fig. 31) reflects a typical hysteretic behavior. Figure 35a displays a time-series of soil moisture, and figure 35b the corresponding time-series of pH. Figure 35c shows the related olivine weathering rate, while the pattern of weathering rate with soil moisture with some grey arrows representative of the trajectories is plotted in figure 35d.

The hysteretic pattern of weathering rate with soil moisture highlights that the process maintains a memory of past events, such as the drying and wetting events. For a single soil moisture value there are two or more different weathering rate values, the lower ones related to the wetting period and the higher ones related to the drying one. This confirms that wetness is one of the most relevant factors

controlling soil biogeochemistry and, in turn, weathering rate [138,139].

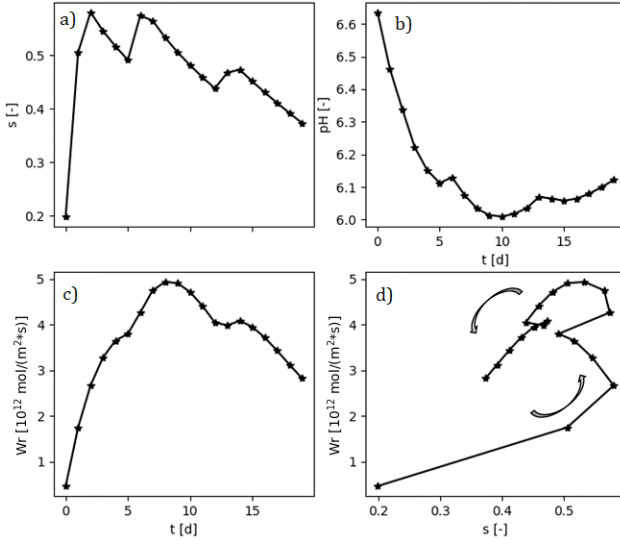


Figure 35 - Time-series of soil moisture (a), pH (b), weathering rate (c) and pattern of weathering rate with soil moisture (d) with the grey arrows indicating the trajectories. The figure is taken from Cipolla, et al. [31].

### 4.3.3 The role of cation exchange processes on EW

As it can be seen from the previous sections, the cation exchange plays an important role in the model. Depending

on the equilibrium reactions regulating the exchanges between the dissolved ions in soil water and those adsorbed on soil colloids (eqs. 30, 31), significant variations in soil pH can be expected, in turn impacting the olivine weathering rate. To understand the role of the cation exchange process on EW, it is instructive to look at the one-year time-series of soil water pH, of the sum of  $Ca^{2+}$ ,  $Mg^{2+}$ ,  $Na^+$  and  $K^+$  concentrations, indicated for brevity as nutrients, and of weathering rate for three different cation exchange capacity levels. The first one, indicated as “No CEC”, represents the condition in which CEC effects are negligible, the other one represents a typical cation exchange value (see, e.g., Weil and Brady [19]), indicated as “CEC”, and the last one, named as “Double CEC”, represents an exceptionally high cation exchange capacity. In this last case, the CEC parameters values are the double of those presented in Weil and Brady [19], related to the “CEC” scenario.

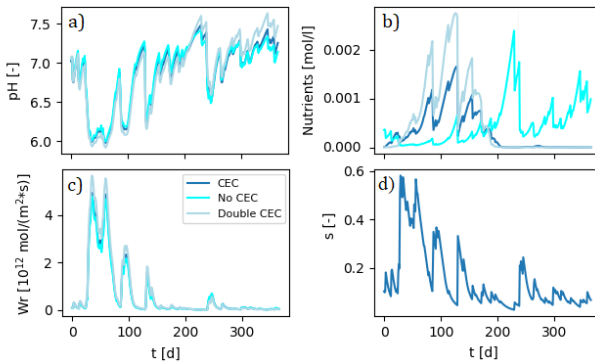


Figure 36 - Time-series of soil water pH (a), of nutrients concentration in soil water (b) and of olivine weathering rate (c) under three different CEC levels. Forcing soil moisture time-series is presented in panel (d). The figure is taken from Cipolla, et al. [31].

As seen in figure 36b, in correspondence of the high values of the nutrients concentration in soil water under the “No CEC” level, approximately from day 200 to 365, there is a strong adsorption process as long as the cation exchange process is included, which becomes more relevant as the cation exchange capacity level increases. This happens because the cation exchanges are regulated by equilibrium reactions, thus if the concentration of dissolved ions is high, the adsorption process will be strong. On the other hand, in correspondence of the low values of the dissolved ions concentration under the “No CEC” level, there is a weak adsorption of cations on soil colloids, resulting in a higher concentration in soil water. The same aspect can be found for the pH time-series (figure 36a). The pH variations due to different CEC levels reflect on

weathering rate (figure 36c). Indeed, especially in correspondence of minimum pH values (e.g., approximately from day 30 to 90), a greater CEC results in a pH reduction, hence in a more accentuated peak of weathering rate.

All these aspects show the importance of a dynamical model which explicitly takes into account the cation exchange processes. The effects of these exchanges, regulated by equilibrium reactions, on soil biogeochemistry and, in turn, on EW dynamics could become prominent over long time-scales, as they may sometimes enhance due to the nonlinearities.

#### 4.3.4 The role of plants on soil biogeochemistry affecting EW

Plants take up magnesium, calcium, potassium and sodium from soil water as common, important nutrients. In order to maintain a neutral balance, the excess of cation uptake is counteracted by a release of hydrogen ions in soil water, increasing soil water pH. To highlight the importance of this process in soil biogeochemical dynamics, a comparison of pH, weathering rate and nutrients concentration time-series with and without plants uptake/release of ions is provided in figure 37.

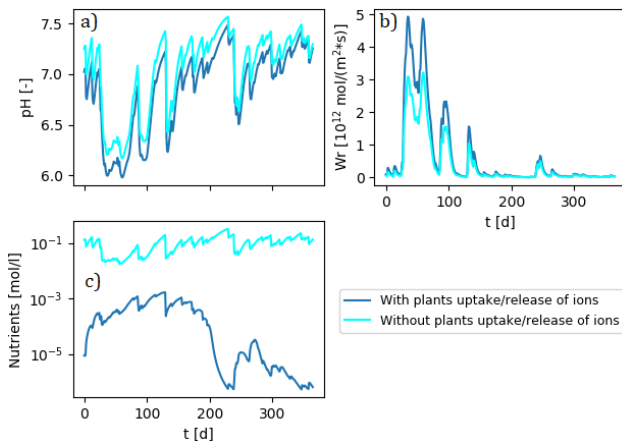


Figure 37 - Time-series of soil pH (a), olivine weathering rate (b) and nutrients concentration in soil water (c) with and without the plants uptake/release of ions process. The figure is taken from Cipolla, et al. [31].

Without plants uptake, the sum of nutrients concentrations in soil water is generally higher and less variable than in the case where the nutrients uptake is taken into account. In the latter case, the greater variability can be explained by the fact that the uptake is proportional to the transpiration rate, whose variability is inherited from rainfall. Consequently, without the release of hydrogen ions, soil pH is generally higher. This affects olivine weathering rate, since higher pH values correspond to lower weathering rates. These aspects clearly demonstrate the importance of correctly capturing the plants uptake/release of ions when modeling EW applications.

## Chapter 5 – The role of hydrology on EW: from hydroclimatic scenarios to carbon-sequestration efficiencies

The model presented in Chapter 4 couples soil biogeochemical processes (pH, CO<sub>2</sub>, cation exchange) and ecohydrological dynamics (soil moisture, plants) to the dissolution of olivine in the soil root zone. The model allows to explore the role of precipitation (hereafter named “climate effect”) and its intermittency, plants and other ecohydrological processes, as well as biogeochemistry on EW dynamics.

In this chapter, some model simulations, described in detail in Cipolla, *et al.* [32], are presented to understand which climates, hence areas of the world, are more suitable to EW and to quantify the actual rates of CO<sub>2</sub> sequestration resulting from olivine dissolution for given climate and land use conditions, including the presence of soil organic matter.

The simulations presented in this chapter may help to quantify the role of hydrological processes on EW dynamics. Indeed, characterizing various climate conditions with respect to EW could help decision makers to define the parts of the globe more suitable for amending soil with reactive minerals, in perspective to put EW into practice. Indeed, the actual rates of CO<sub>2</sub> sequestration due to olivine dissolution in the field are not well defined so far, as many studies [15,25,26] base their estimates on the

theoretical limit of 1.25 grams of CO<sub>2</sub> per gram of dissolved olivine. To this regard, the model allows to better characterize the actual rates of CO<sub>2</sub> sequestration, considering the dynamics of bicarbonate (HCO<sub>3</sub><sup>-</sup>) and carbonate (CO<sub>3</sub><sup>2-</sup>) ions in soil water resulting from olivine dissolution. A possible improvement of EW yields, by amending soil with organic matter is also explored, since this can lead to a change in soil chemistry (i.e., cation exchange and pH), and, in turn, weathering rates, apart from effects related to water holding capacity and nutrient retention. Another goal is related to quantify the increase of nutrients availability and pH, as also noted by Weil and Brady [19] and Renforth, *et al.* [25], due to olivine dissolution since, in some cases, these aspects can enhance plants productivity [140]. In the following sections, a description of some simulations scenarios and the corresponding parameters is provided. After that, results are deeply analyzed and discussed.

## 5.1 EW scenarios and parametrizations

### 5.1.1 Climate scenarios description

To assess the role of climate on EW and explore solutions aimed to enhance weathering rates and carbon sequestration, the dissolution of olivine under different mean annual precipitation (MAP) scenarios is analyzed. In particular, five scenarios, labeled S1 to S5, characterized by the same average rainfall depth ( $\alpha$ ) but different storm

frequencies ( $\lambda$ ), resulting in MAP ranging from about 900 to 3000 mm (details in table 2), are taken into account. This specific precipitation range is selected because, for MAP lower than 900 mm, the environment is too dry for EW applications [19], while only a limited area of the globe has MAP higher than 3000 mm. Since the interest is devoted in the role of climate on EW, soil and vegetation properties are maintained constant. For the sake of simplicity, analyses are not carried out with reference to a forested soil, in order to neglect the presence of aluminum in the system that, as explained in Chapter 4, would represent one of the major  $H^+$  sources for this strong acid soil. For the background weathering, the dissolution rate constant of anorthite is used. In all scenarios, the addition of  $10 \text{ kg m}^{-2}$  of olivine, after the soil biogeochemistry (time-series of C, and of dissolved and adsorbed  $Ca^{2+}$ ,  $Mg^{2+}$ ,  $Na^+$  and  $K^+$ ) reached a statistically stationary regime, consistent with the given climate, is taken into account. The effects of olivine dissolution on soil chemistry and carbon sequestration are then analyzed after a simulated period of five years, in order to look at the short-middle term effects of olivine dissolution. The long term effects of olivine dissolution are here omitted since they are not consistent with the short-middle term goals of carbon sequestration, in order to counteract the greenhouse effect. In any case, the analyses may be extended to any time horizon.

Table 2 - List of parameters varying among the different climate scenarios. The table is taken from Cipolla, et al. [32].

Parameter	Value				
	<i>S1</i>	<i>S2</i>	<i>S3</i>	<i>S4</i>	<i>S5</i>
<i>Scenario</i>	<i>S1</i>	<i>S2</i>	<i>S3</i>	<i>S4</i>	<i>S5</i>
$\lambda$ [d <sup>-1</sup> ]	0.2	0.33	0.5	0.63	0.75
MAP [mm]	920	1325	2010	2530	3010
ADD [gC m <sup>-2</sup> d <sup>-1</sup> ]	1.5	1.8	2.2	2.5	2.7
T <sub>max</sub> [mm d <sup>-1</sup> ]	4.5	5.1	6	6.8	7.3
I <sub>Ca<sup>2+</sup></sub> [μmol m <sup>-2</sup> d <sup>-1</sup> ]	100	200	300	400	500
I <sub>Mg<sup>2+</sup></sub> [kg ha <sup>-1</sup> y <sup>-1</sup> ]	1.1	1.36	1.78	2.1	2.4
I <sub>K<sup>+</sup></sub> [kg ha <sup>-1</sup> y <sup>-1</sup> ]	0.5	1	1.5	2	2.5
I <sub>Na<sup>+</sup></sub> [mg m <sup>-2</sup> d <sup>-1</sup> ]	3	4.6	7	9	10

To understand to what extent organic matter amendments (e.g., compost) would increase weathering rates and carbon sequestration, some simulations with an increased soil carbon input are also presented. In particular, at all scenarios, the ADD term in Table 2 is increased by 0.2 gC m<sup>-2</sup> d<sup>-1</sup>, or equivalently 73 gC m<sup>-2</sup> y<sup>-1</sup>. On the basis of the amount of extractable organic carbon of grass cuttings (i.e., about 40 % of organic carbon with respect to the total dry weight of compost), this amount would correspond to about 2 t<sub>compost</sub> ha<sup>-1</sup> y<sup>-1</sup>, which is the typical average amount of compost used to amend an agricultural soil. For each scenario, the effect of organic amendment is assessed by maintaining the same time-series of soil moisture as for the base scenarios without amendment to better isolate the changes in soil chemistry and carbon sequestration due to the additional organic matter.

As an example, a typical model simulation, carried out with the parameters related to the S1 scenario, presented in table 2, is here reported. Figure 38 shows the time-series of the most representative variables of the model (i.e., (a) soil moisture, (b) organic matter concentration, (c) CO<sub>2</sub> concentration in the gas phase, (d) alkalinity, (e) total dissolved inorganic carbon concentration, (f) Mg<sup>2+</sup>, Ca<sup>2+</sup> and the sum of Na<sup>+</sup> and K<sup>+</sup> concentrations, (g) pH, (h) weathering rate and (i) the reduction of olivine particles diameter) related to a time interval of about three years after olivine addition. As soil moisture increases, there is a stronger decomposition of organic matter, a lower pH and a greater weathering rate.

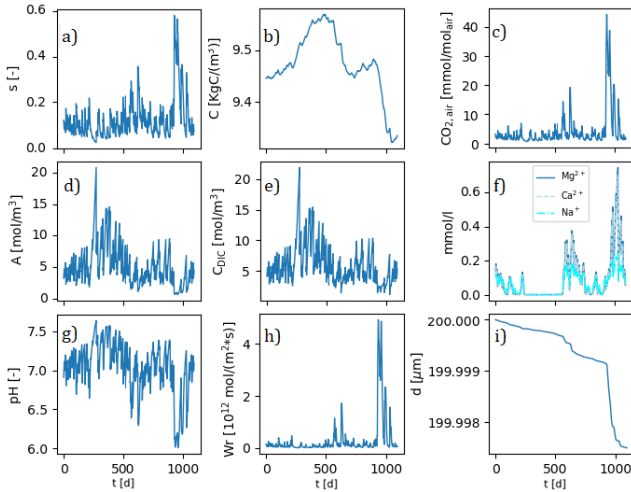


Figure 38 - Time series of the most representative variables of the model after running a generic simulation of the model by means of the parameters of the S1 scenario, listed in table 2. Panels display the time-series of: (a) soil moisture, (b) organic matter concentration, (c)  $\text{CO}_2$  concentration in the gas phase, (d) alkalinity, (e) total dissolved inorganic carbon concentration, (f)  $\text{Mg}^{2+}$ ,  $\text{Ca}^{2+}$  and the sum of  $\text{Na}^+$  and  $\text{K}^+$  concentrations, (g) pH, (h) weathering rate and (i) the reduction of olivine particles diameter. The figure is taken from Cipolla, et al. [32].

### 5.1.2 Parameters and data

The values for the parameters related to climate, soil, and vegetation are listed in Table 3. In order to better highlight the role of climate on EW, without confounding factors deriving from different soil properties, a sandy soil for all scenarios is considered. The specific CEC of organic

matter and clay colloids are extracted from Weil and Brady [19], while the selectivity constants, related to the CEC, from Suarez and Šimůnek [134]. The values of *ADD*, the maximum transpiration rate and the input of calcium, magnesium, potassium and sodium for the five considered climate scenarios are reported in table 2. Typical levels of input of calcium, magnesium, potassium and sodium provided by Pulido-Villena, *et al.* [141], Groshans, *et al.* [142], Mikhailova, *et al.* [143] and Suweis, *et al.* [144] are used, which scale according to MAP, based on the observation that deposition increases with MAP [141-143]. The mass fraction of anorthite is representative of all the minerals within the soil, different than olivine, consuming  $H^+$  due to their weathering processes. This parameter is fixed equal to 1%, but it could be modified in order to increase or decrease the term related to these weathering processes. The diameter of the anorthite particles is assumed to be equal to that of the olivine particles. The background weathering is fundamental to characterize the initial soil pH, consistently with the given climate. Indeed, this strongly affects olivine dissolution dynamics. In these applications, anyway, the background weathering characteristics (i.e., the mass fraction and diameter of anorthite particles) are considered constant among the five analyzed climate scenarios, mainly due to the fact that the main goal is to explore the climate effects on EW. Therefore, in order to isolate these effects, all the soil and vegetation parameters do not have to vary with respect to MAP. It is however worth noticing that for real case-study applications the background weathering parameters should be defined based on the soil properties

under analysis. Olivine amendment is set to  $10 \text{ kg}_{\text{olivine}} \text{ m}^{-2}$ , approximately equal to the amount used in the pot experiment by Renforth, *et al.* [25]. (the authors used 100 g of olivine for a cylindrical soil sample of diameter 0.1 m and height 1 m, corresponding to about  $12 \text{ kg}_{\text{olivine}} \text{ m}^{-2}$ ).

*Table 3 - List of parameters of soil, vegetation, climate and weathering in the model. The table is taken from Cipolla, et al. [32].*

	Symbol	Value	Reference
<b>Soil parameters</b>			
Porosity	n	0.4	Assumed
Soil depth	$Z_r$ [m]	0.8	Assumed
Field capacity	$s_{fc}$	0.3	Assumed
Hygroscopic point	$s_h$	0.02	Assumed
Saturation hydraulic conductivity	$K_s$ [ $\text{m d}^{-1}$ ]	1.1	Assumed
Pore size distribution index	b	4	<a href="#">[145]</a>

Initial carbon concentration in the soil	$C_{in}$ [gC m <sup>-3</sup> ]	10000	Assumed
Initial carbon concentration in the biomass	$C_b$ [gC m <sup>-3</sup> ]	100	Assumed
Bulk density	$\rho_b$ [kg m <sup>-3</sup> ]	1600	<a href="#">[146]</a>
Specific CEC <sub>OM</sub>	CEC <sub>OM, s</sub> [cmol kg <sub>OM</sub> <sup>-1</sup> ]	200	<a href="#">[19]</a>
Specific CEC <sub>clay</sub>	CEC <sub>clay, s</sub> [cmol kg <sub>clay</sub> <sup>-1</sup> ]	80	<a href="#">[19]</a>
Mass fraction of clay	$f_{clay}$	0.1	<a href="#">[146]</a>

Selectivity  
constant  $\text{Ca}^{2+}$  -  $\text{Mg}^{2+}$  for OM     $\text{SC}_{\text{OM}} (\text{Ca}^{2+} - \text{Mg}^{2+})$     4.65    [\[134\]](#)

Selectivity  
constant  $\text{Ca}^{2+}$  -  $\text{Mg}^{2+}$  for clay     $\text{SC}_{\text{clay}} (\text{Ca}^{2+} - \text{Mg}^{2+})$     1.1    [\[134\]](#)

Selectivity  
constant  $\text{Na}^{+}$  -  $\text{Ca}^{2+}$  for OM     $\text{SC}_{\text{OM}} (\text{Na}^{+} - \text{Ca}^{2+})$     10    [\[134\]](#)

Selectivity  
constant  $\text{Na}^{+}$  -  $\text{Ca}^{2+}$  for clay     $\text{SC}_{\text{clay}} (\text{Na}^{+} - \text{Ca}^{2+})$     1.96    [\[134\]](#)

---

**Soil-vegetation parameters**

Point of incipient stress	$s^*$	0.17	Assumed
---------------------------	-------	------	---------

Permanent wilting point	$s_w$	0.065	Assumed
-------------------------	-------	-------	---------

---

### Vegetation parameters

Evaporation at the wilting point	$E_w$ [mm d <sup>-1</sup> ]	1	Assumed
----------------------------------	-----------------------------	---	---------

---

### Carbon decomposition parameters

Decomposition constant	$k_{dec}$ [m <sup>3</sup> d <sup>-1</sup> gC <sup>-1</sup> ]	$6.5 \times 10^{-6}$	Assumed
------------------------	--	----------------------	---------

Carbon respiration fraction	$r$	0.7	<a href="#">[125]</a>
-----------------------------	-----	-----	-----------------------

---

### Rainfall parameters

Average storm depth	$\alpha$ [mm]	11	Assumed
---------------------	---------------	----	---------

---

### CO<sub>2</sub> parameters

Atmospheric CO <sub>2</sub> concentration	CO <sub>2, atm</sub> [ppm]	412	Assumed
---	----------------------------	-----	---------

Free-air diffusion coefficient of CO <sub>2</sub>	$D_0$ [m <sup>2</sup> s <sup>-1</sup> ]	$1.6 \times 10^{-5}$	<a href="#">[131]</a>
--	---	----------------------	-----------------------

---

### Background weathering parameters

Specific dissolution rate of anorthite	$k_{bg}$ [mol m <sup>-2</sup> s <sup>-1</sup> ]	$5.6 \times 10^{-9}$	<a href="#">[100]</a>
Diameter of anorthite particles	$d_{bg}$ [μm]	200	Assumed
Mass fraction of anorthite	$f_{bg}$	0.01	Assumed
Density of anorthite	$\rho_{bg}$ [g cm <sup>-3</sup> ]	2.75	<a href="#">[147]</a>

---

### Olivine weathering parameters

Specific dissolution rate	$k_{sil}$ [mol m <sup>-2</sup> s <sup>-1</sup> ]	$1 \times 10^{-10}$	[25,100]
Dissolution constant	Log( $k_{eq}$ )	7.11	<a href="#">[126]</a>

Molar volume	$V_M$ [ $\text{cm}^3 \text{mol}^{-1}$ ]	44.08	<a href="#">[26]</a>
Effective diameter of particles	$\phi$ [ $\mu\text{m}$ ]	200	<a href="#">[25]</a>
Density	$\rho_{\text{oliv}}$ [ $\text{g cm}^{-3}$ ]	3.275	<a href="#">[148]</a>
Mass of added olivine	$M_{\text{oliv}}$ [ $\text{kg}_{\text{olivine}} \text{m}^{-2}$ ]	10	<a href="#">[25]</a>

---

Plant biomass productivity is positively correlated to MAP, especially when this is higher than 600 mm [145]. To take this aspect into account, the input of organic matter from plant litter (*ADD*) is rescaled according to the annual plant productivity of the given climate [125]. The increase of the MAP and plant biomass productivity also leads to a higher transpiration rate. Generally transpiration rate is linearly related to the canopy cover [146], which likely increases as the plant biomass productivity grows. The maximum transpiration rate is thus rescaled according to MAP, also based on typical values of potential evapotranspiration at the global scale [147].

## 5.2 Climate effects on EW

Climate mainly affects the dissolution of olivine and CO<sub>2</sub> sequestration through its control on the soil moisture dynamics. The latter in fact affects organic carbon decomposition, soil pH, and in turn olivine dissolution and leaching of dissolution products. In the next section a comparison between the dynamics under a dry (S1) and a wet (S5) scenarios is carried out; after that, results provided by all five scenarios are analyzed.

### 5.2.1 Temporal dynamics of soil moisture and organic carbon

The time series of soil moisture and organic carbon for the S1 and S5 scenarios (see table 2) are presented in figure 39a and 39b, respectively, along with the probability distribution functions (pdfs) of soil moisture. As expected, while the soil water content under the S5 is on average higher than that of S1 (an average of 0.26 in S5 and 0.11 in S1), the figure also shows that in the former there is higher variability, as evident from the standard deviation (0.13 in S5 and 0.06 in S1) and more in general from the pdfs shape. The propagation of soil-moisture variability to the organic carbon depends on the inertia of the organic matter pool, represented by the decomposition constant,  $k_{dec}$ , and the carbon concentration in the biomass pool,  $C_b$ , as described

in Porporato, *et al.* [125] and D’Odorico, *et al.* [129]. Overall, although the carbon input is higher in wetter climates (table 2), the organic carbon mean concentration is higher in scenario S1 ( $9.4 \text{ kgC m}^{-3}$ ) than S5 ( $8.8 \text{ kgC m}^{-3}$ ), as the effect of faster decomposition prevails; indeed, wet environments are generally more suitable for the biomass to decompose the organic matter, since microbial activity and consequently the decomposition rates are higher [129]. Scenario S1 also has higher standard deviation, which is explained by the inverse proportionality between decomposition and soil moisture when the latter is above field capacity.

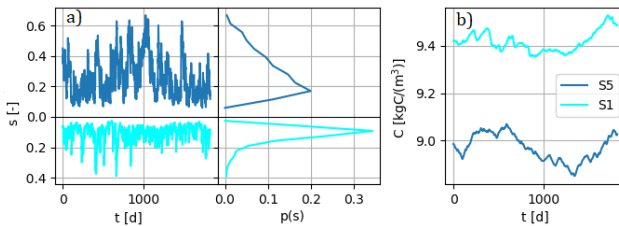


Figure 39 - Time series of soil moisture (a) and organic carbon (b) in the S1 and S5 scenarios. In figure 39a the empirical pdfs of soil moisture under the S1 and S5 scenarios are also displayed. Panel (a) presents a reflected axis, thus the values in the lower half are positive. The figure is taken from Cipolla, *et al.* [32].

## 5.2.2 pH-soil moisture relation

Since in both simulations the same soil properties are considered, the differences in pH dynamics are only due to a different soil water content and a different organic matter concentration, which depends on the carbon input and decomposition rate. In agreement with observations, which report that, at a global scale, soils are more acidic in humid climates [148,149], in the presented scenarios soil pH is generally higher in S1 (6.6 on average) than in S5 (5.9 on average), as shown in Figure 40a. These pH levels are also in line with typical pH values found in wet and dry environments, respectively (see Fig. 3a in Slessarev, *et al.* [148] or Merry [149]). This tendency originates from multiple factors; one is related to the amount of  $H^+$  in rainfall. In fact, because of slight acidity of normal rain, soils in regions with higher MAP receive more  $H^+$ . Furthermore, as plants uptake nutrients from soil water, such as  $Ca^{2+}$ ,  $Mg^{2+}$ ,  $K^+$  and  $Na^+$ , that are positively charged, they release  $H^+$  ions to balance the extra-uptake of positively charged ions and maintain a neutral charge. This is favored in wetter climates with higher plant water and nutrient uptake rates. Lastly, due to the low leaching, dry soils tend to accumulate alkaline ions, such as carbonate and bicarbonate ions, mainly generated from the organic matter decomposition, that can react with  $H^+$  and help maintain higher soil pH.

Looking at the probability density functions (pdfs) it is also evident that scenario S5 presents a slightly higher variability, as confirmed by the standard deviation values

(0.32 in S5 and 0.30 in S1). By looking at its pdf, it is possible to notice the presence of a double peak that, especially when the pH is high, tends to remain at this level for a certain amount of time before decreasing. A high pH is associated to low soil moisture values (see figure 40b) and, consequently, given the low decomposition rate, to high concentrations of organic carbon. This leads to a high organic CEC, and thus to a strong buffering capacity and resistance to pH variations. Therefore, in these conditions, the CEC tends to keep the pH high, until soil moisture and decomposition rate of organic matter increase in a significant way, resulting in a reduction of CEC and therefore in a lowering of pH. The repeating occurrence of such phenomena leads to the presence of a peak in the pdf even at higher pH (specifically at pH of about 6.3), apart from the most probable pH in S5 scenario, which is about 5.8. This aspect is not visible in the S1 scenario, since it is characterized by a lower pH and smaller soil moisture variability, and hence there are no abrupt changes in the soil buffering capacity and pH, which tends to be concentrated around the most probable value (equal to about 6.7).

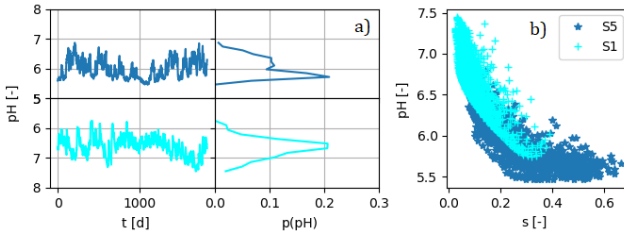


Figure 40 - Time series of soil pH (a) and soil pH vs soil moisture (b) in the S1 and S5 scenarios. In figure 40a the empirical pdfs of pH under the S1 and S5 scenarios are also displayed. The visualization scheme is the same to that in Figure 39. The figure is taken from Cipolla, et al. [32].

### 5.2.3 Olivine dissolution dynamics

The effect of climate on olivine-dissolution dynamics can be clearly seen on the different temporal evolution of the weathering rate (figure 41a), the latter being one order of magnitude higher in scenario S5 (wetter) than S1. In particular, the mean weathering rate is  $4.3 \times 10^{-12} \text{ mol m}^{-2} \text{ s}^{-1}$  in S5 and  $4.6 \times 10^{-13} \text{ mol m}^{-2} \text{ s}^{-1}$  in S1. This is not a surprising result, since previous studies already observed that higher soil water content leads to higher reactive surface areas of olivine particles and, in turn, to higher dissolution rates [15,19,98].

The relation between weathering rate and soil moisture reflects the number of interactions involved in the olivine dissolution dynamics. As it clearly appears from figure 42a, even if the direct influence of soil moisture on weathering rate is assumed linear (linear soil moisture - mineral surface

area relation), the effective relationship, that also takes into account the indirect influence of soil moisture, results in a non-linear and non-unique relationship. Indirect effects include for instance the role of soil moisture variability on pH, which, in turn, is another important variable affecting the weathering rate [15,19]. Figure 41a also highlights that weathering rate and soil moisture exhibit interesting hysteresis cycles, with lower weathering rates during the wetting process and higher ones during the drying phase.

Although olivine has one of the highest dissolution rates compared to other minerals [15], the dissolution times are relatively long, regardless of soil moisture and pH conditions. Indeed, according to Lasaga [100], the mean lifetime of a 1 mm diameter olivine particle is equal to about 600,000 years. This is confirmed in figure 41b where, even at high MAP, five years after the addition of olivine, the diameter reduction is very low (e.g., about 0.06% for the S5 scenario). In any case, the effect of different climates in the reduction of the diameter of olivine particles is evident since, under the S5 scenario, it is greater than that of the S1 scenario, due to the generally higher weathering rate.

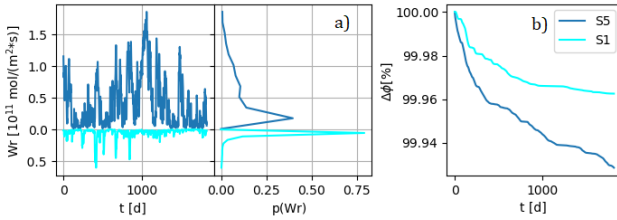


Figure 41 - Time series of olivine weathering rates and their empirical pdfs (a); variation of the particles diameter over time under the S1 and S5 scenarios (b). The visualization scheme is the same to that in Figure 39. The figure is taken from Cipolla, et al. [32].

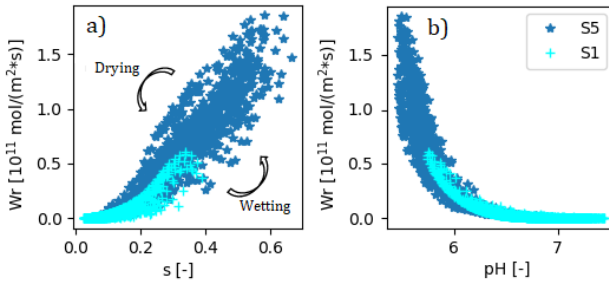


Figure 42 - Pattern of olivine weathering rate with soil moisture (a) and with soil pH (b) under the S1 and S5 scenarios. The figure is taken from Cipolla, et al. [32].

### 5.3 The role of organic matter on EW

As seen above, the olivine weathering rate increases as soil water becomes more acidic. To this regard, it is interesting to explore whether increasing the organic matter

content by means of soil amendment can increase the availability of  $H^+$  for olivine dissolution and, in turn, increase weathering rate. Figure 43 compares, in a box-plot form, the organic carbon concentration (figure 43a), soil pH (figure 43b) and olivine weathering rate (figure 43c) achieved with and without carbon amendment. The boxes are delineated from the 25<sup>th</sup> to the 75<sup>th</sup> percentile of the considered variable and the whiskers are used to indicate the variability outside the upper and lower quartiles. The effects of organic matter amendment are evaluated for a period of 5 years after the addition of olivine for all climatic scenarios.

The changes in the organic carbon concentration mainly depend on how much the decomposition term grows relative to the addition itself. The decomposition rate is linearly related to the organic carbon concentration, which is generally expected to grow if the carbon input is higher. Results show that, due to a higher decomposition rate, the organic carbon tends to decrease with MAP, especially when it exceeds 1300 mm. A similar pattern is visible under the scenario with carbon amendment, even though, as expected, with higher values of carbon concentration. While this relation may appear to contradict global scale observations of soil organic carbon, it is worth to emphasize that the maximum variation of organic matter between the driest and the wettest scenario is very small (only about  $2 \text{ kg}_C \text{ m}^{-3}$ ). In the analysis, constant soil properties and composition are considered, a fact that may considerably affect organic matter decomposition dynamics.

The pH tends to decrease with MAP under both the carbon input scenarios. This extends the result reported in figure 40a to all the considered climate scenarios. It is also relevant to see that, as MAP increases, the soil pH at the scenario with carbon amendment progressively gets close to the one related to the base carbon input in table 2 until, in very humid conditions, which are provided by a MAP greater than 2000 mm, the higher carbon input leads to a slight reduction of soil pH (at least with reference to median values). With reference to the pH variability, there seems to be no pattern with MAP and, under the amendment scenario, the interquartile range is almost the same as in the case where the increase of organic matter is not considered. It is hence possible to conclude that organic matter amendment is effective under very humid climates, where it leads to a pH reduction, although small at least with reference to the case studies presented.

In general, the response of pH to the increase of organic matter depends on a balance between two contrasting effects: the increase of soil buffering capacity and the greater decomposition of carbonate and bicarbonate ions along with the greater input of  $H^+$  due to infiltration and plants action. On the one hand, in dry conditions, a greater pH is recorded under higher organic matter addition, because the increase in the organic CEC, and thus of the soil buffering capacity, prevails over the plant and rainfall input of  $H^+$ . On the other hand, in wet conditions, the input of  $H^+$  due to infiltration and plants action tends to become more relevant than the increase in soil buffering capacity, leading to a reduction in soil pH. Furthermore, the faster

decomposition of organic matter in wet climates leads to a greater increase of the carbonic acid and bicarbonate ion concentration in the soil water, which rapidly dissociate releasing  $H^+$  and lowering soil pH.

The variation of soil pH due to the different climate and organic matter addition scenarios affects olivine weathering rate. Whether soils are organically amended or not, there is a significant increase of the weathering rate with MAP (figure 43c) and its interquartile range, which is representative of the weathering rate variability. However, adding organic matter is effective only when MAP exceeds 2000 mm since, in correspondence of the carbon amendment scenario, the weathering rate is slightly greater than in the case achieved with the carbon input values presented in table 2 (i.e., in figure 43c, at the “Amendment” scenario, the median weathering rate is slightly higher than the one achieved at the “ADD” scenario). This is a natural consequence of the pH reduction which, under the greater carbon input, only occurs when MAP exceeds 2000 mm.

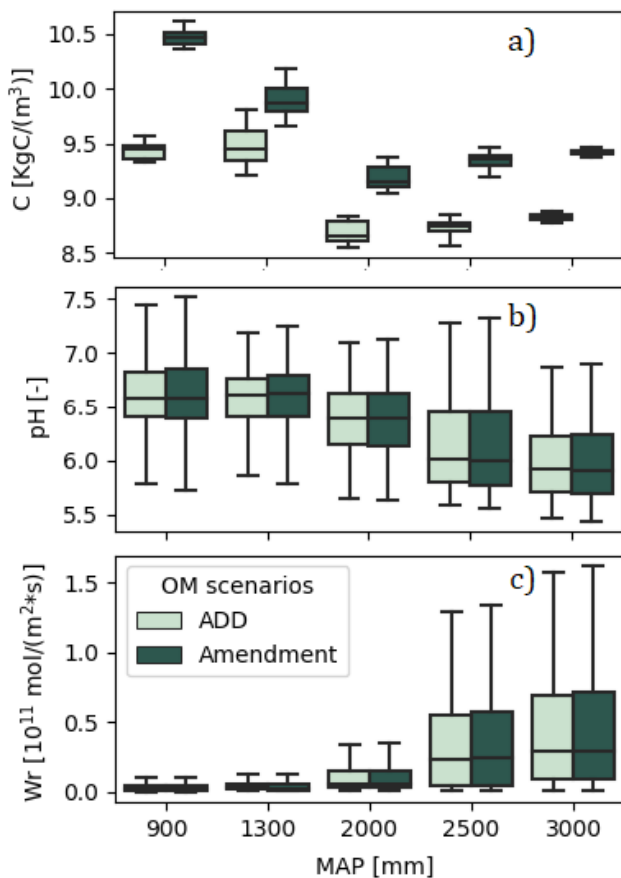


Figure 43 - Box plots for the organic carbon concentration (a), soil pH (b) and olivine weathering rate (c) under all the considered climate scenarios and two different inputs of organic matter. The figure is taken from Cipolla, et al. [32].

## 5.4 Analysis of EW benefits

Several studies have shown that using olivine for EW applications leads to carbon sequestration and increase of nutrients availability [15,25]. Estimates of carbon sequestration [15,25,26], however, are generally based on the theoretical limit of  $1.25 \text{ gCO}_2/\text{g}_{\text{oliv}}$ , although it is acknowledged that the actual sequestration can be considerably lower and time varying. To this regard, the model here presented allows to estimate carbon sequestration in a more reliable way, for example by taking into account the effect of extra amount of bicarbonate ( $\text{HCO}_3^-$ ) and carbonate ( $\text{CO}_3^{2-}$ ) ions in soil water originating from olivine dissolution and in relation to whether they are transported away to groundwater and to stream through soil water percolation.

This distinction is particularly important since  $\text{HCO}_3^-$  and  $\text{CO}_3^{2-}$  ions in soil water due to the weathering of olivine could potentially react with  $\text{H}^+$  to form carbonic acid, causing an increase in pH and a consequent slowdown of the olivine dissolution rate. On the contrary, actual carbon sequestration is more closely related to the extra  $\text{HCO}_3^-$  and  $\text{CO}_3^{2-}$  ions that are leached away from the soil. The actual sequestered carbon due to EW can be estimated as the leached mass of the extra  $\text{HCO}_3^-$  and  $\text{CO}_3^{2-}$  produced by olivine dissolution, at each time step.

Apart from carbon sequestration, olivine application leads to other effects related to the changes in soil chemistry. For instance, by reacting with  $\text{H}^+$  it leads to an

increase of soil pH. In many cases, this is beneficial to plant productivity [19,140], which may be further enhanced by the release of nutrients upon olivine dissolution [25]. It is worth noting that a nutrient increase in soil water is not necessarily beneficial for vegetation (in the following section only the increase of nutrients in soil water as a common effect of olivine dissolution is shown). For example, an excess of  $Mg^{2+}$  in soil water may be the cause of reduced soil fertility, which depends on the Ca:Mg ratio at the exchange sites [150].

### 5.4.1 Carbon sequestration

Olivine reacts with  $CO_2$  drawing it into solution to form  $HCO_3^-$  and  $CO_3^{2-}$  ions. However, due to the reasons described before, the actual sequestered  $CO_2$  is better connected to the leached mass of these ions. In figure 44a the equivalent mass of  $CO_2$ , called  $CO_{2,sw}$ , assessed on the base of the carbon contained in the mass of  $HCO_3^-$  and  $CO_3^{2-}$  ions produced from olivine dissolution is plotted, while figure 44b displays a box plot of the sequestered  $CO_2$ , evaluated as a function of the leached mass of  $HCO_3^-$  and  $CO_3^{2-}$ .

The  $CO_{2,sw}$  increases with MAP only up to 2000 mm (figure 44a), mainly due to the rapid increase in weathering rate under this MAP threshold. However, at MAP greater than 2000 mm, there is a decrease of the  $CO_{2,sw}$ , in spite of the weathering rate increase. This fact could be connected

to the methodology used in its evaluation, which does not take into account the outputs of  $\text{HCO}_3^-$  and  $\text{CO}_3^{2-}$  ions. For instance, some  $\text{HCO}_3^-$  and  $\text{CO}_3^{2-}$  react with  $\text{H}^+$  and form the carbonic acid. Comparing the plots related to the different carbon input scenarios, it is worth noticing that, adding organic matter seems to be effective, especially for MAP above 2000 mm, since there is a general increase of  $\text{CO}_{2,\text{sw}}$ .

The sequestered  $\text{CO}_2$ , instead, increases with MAP for two reasons: i) higher weathering rates imply greater concentrations of  $\text{HCO}_3^-$  and  $\text{CO}_3^{2-}$  in soil water and ii) higher MAP increasing the percolation rates. The combination of these two factors leads to an increased sequestered  $\text{CO}_2$  with MAP at a rate which is faster than the increase in weathering rate itself. The small mass of sequestered  $\text{CO}_2$  under all climate scenarios is due to the short time interval used in the box plots generation (i.e., five years), which does not allow to see significant effects from the leaching component. Indeed, according to Hartmann, *et al.* [15], at longer time scales of decades or centuries, the cations resulting from olivine dissolution (i.e.,  $\text{HCO}_3^-$  and  $\text{CO}_3^{2-}$ ) tend to remain in solution, thus leading to carbon sequestration in aqueous form. To see significant amounts of sequestered  $\text{CO}_2$ , due to the leaching of bicarbonate and carbonate ions, much longer time scales would be necessary, especially in the condition where MAP and leaching rate are low.

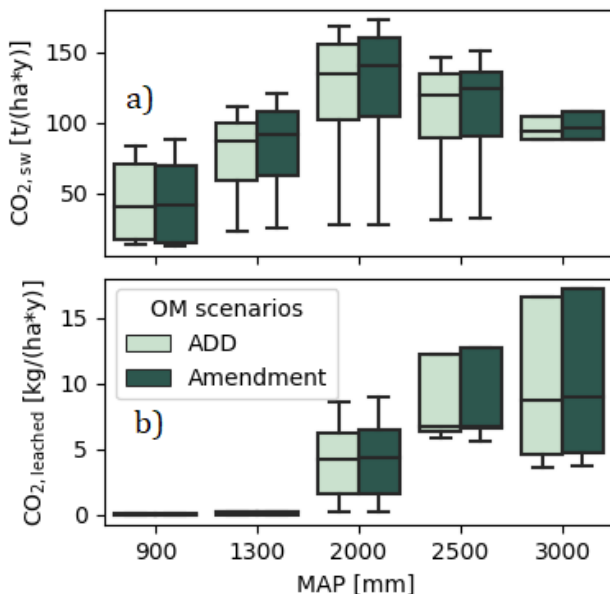


Figure 44 - Box plots of the annual mass of CO<sub>2</sub> that reacts with olivine and is dissolved in soil water in the form of HCO<sub>3</sub><sup>-</sup> and CO<sub>3</sub><sup>2-</sup> (a) and of the annual mass of sequestered CO<sub>2</sub> by leaching (b). The plots are related to all the considered climate scenarios and different inputs of organic matter. The figure is taken from Cipolla, et al. [32].

## 5.4.2 Increase of nutrients availability

In general, olivine dissolution leads to an increase of nutrients availability in soil water [25]. Figures 45a, 45b, 45c and 45d show the annual increase of dissolved calcium, magnesium, potassium and sodium, respectively, for all

climate scenarios. As MAP increases, in line with the increase in weathering rate (figure 43c), the additional availability of nutrients becomes more pronounced above 2000 mm. Even if olivine releases only magnesium from dissolution, the results show an increase of the mass of all the considered nutrients in soil water. This is related to the fact that larger magnesium concentrations in the soil solution lead to greater adsorbed amounts of this mineral on soil colloids, since the adsorption process is regulated by equilibrium reactions. As a result, magnesium replaces adsorbed calcium, sodium and potassium ions, which are thus released in the solution. In the S2 and S3 scenarios, however, there is a slight reduction of magnesium in soil water, which is due to the higher soil organic matter content and CEC, such that magnesium released by olivine dissolution ends up almost entirely adsorbed. The same behavior is observed for calcium since it has the same valence of magnesium. Due to their low adsorption processes, potassium and sodium instead tend to remain in solution.

The increase of these nutrient concentration in soil water, in response to carbon amendment, is given by two contrasting effects on soil pH: an increase in cation exchange capacity, and a greater decomposition of carbonate and bicarbonate ions along with a higher  $H^+$  input due to infiltration and plants action. By determining which of the two effects prevails, climate plays a very relevant role, with a more pronounced increase in nutrients only above a MAP of 2000 mm. Note that, in the long-term, olivine dissolution causes a general loss of exchangeable

calcium, potassium, and sodium, since these ions are replaced by magnesium (which is continuously released from olivine dissolution). As olivine dissolves, this loss becomes progressively more relevant due to the reduction of olivine particles diameter and the corresponding increase of the weathering rate (i.e., a greater input of magnesium).

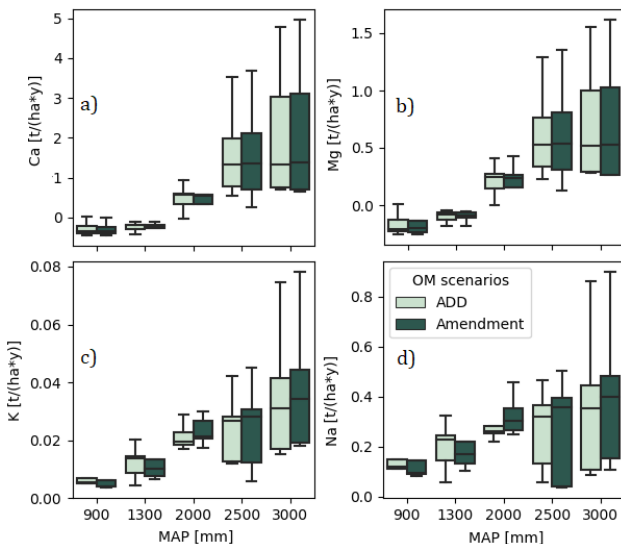


Figure 45 - Box plots related to the annual increase of calcium (a) magnesium (b), potassium (c) and sodium (d) under the considered climate scenarios and different inputs of organic matter. The figure is taken from Cipolla, et al. [32].

## Chapter 6 – Effect of seasonal variability of precipitation and vegetation cycle on enhanced weathering dynamics: an application for Italy and USA

The assumptions made for the applications presented in Chapter 5 may be applied to understand the influence of stationary precipitation with different MAPs on EW. However, these are not valid if carrying out some case-study applications of the EW model. Indeed, it would rather be important to characterize the effect of the seasonal variation of the meteorological force, soil type and crop cycle on EW dynamics.

In this chapter, the model presented in Cipolla, *et al.* [31] is applied to four hypothetical case studies (i.e., agricultural applications of EW), two of them in Italy (i.e., Sicily, in the south, and the Padan plain, in the north) and two in the USA (i.e., California, in the south-west, and Iowa, in the north-central area). The four places under study are characterized by very similar MAP values but much different rainfall seasonality. They also present similar soils and different crop types. Vegetation cycles are worth to be characterized in case-study EW applications, given that crops contribute in the water balance through evapotranspiration losses differently during the year, depending on the crop stage, and in the carbon balance

since they release organic matter (i.e., litter [125,129] and root exudation [151,152]) to the soil. Furthermore, differences among the selected places in terms of cation exchange capacity and background weathering flux (i.e., due to different local parent materials) are taken into account, given that these factors strongly affect soil pH before olivine amendment [31,32]. The main goal of these simulations is therefore to understand which of the considered factors (i.e., rainfall seasonality, soil type and composition and crop cycle) is mostly connected to changes in EW time dynamics. Moreover, they allow to define the most suitable combined characteristics of climate, soil and vegetation to host an EW intervention. The chapter presents different sections. Firstly, a description of the adopted methodology and of the four places under study, along with the estimation of the parameters related to the above-mentioned factors, is provided. Here, an in-depth discussion of the differences in terms of rainfall seasonality, soil and vegetation types is reported. After that, EW dynamics at the four considered sites are presented and discussed, highlighting the role of each of the considered factors on EW. It is worth to specify that, to estimate in an accurate way the weathering and carbon sequestration rate for the whole regions under study, it is necessary to carry out a spatial application of the model, given the strong spatial variability of rainfall, soil properties and crop type. Therefore, results are related to the specific combination of the analyzed factors and cannot be generalized for the whole region under study.

## 6.1 Materials and methods

### 6.1.1 Methodology

The case studies presented in the following sections aim, apart from analyzing the EW and carbon sequestration dynamics in the places under study, to understand which of the factors among rainfall seasonality, soil type and composition, and crop cycle exerts the greatest influence on EW dynamics. A flow chart of the whole procedure here employed is presented in Figure 46. Starting from the definition of the case studies, a very important aspect consists of extracting all the parameters that control the above-mentioned factors. The forcing of the EW model is rainfall, whose seasonality is characterized by how the average depth and frequency of rainfall events vary during the year. These have been defined on the base of daily rainfall data records related to the selected locations. Soil type and vegetation parameters have been characterized by using spatially distributed variables (i.e., the sand, silt and clay content, organic matter, cation exchange capacity, soil pH, crop type and cycle). The procedure involving parameters extraction is better explained in section 6.1.2, which is also devoted to the identification of the areas under study. To figure out which of the considered factor prevails in leading to the greatest differences in EW dynamics, an outline of simulations has been set up, consisting of varying one of them while keeping the remaining two constant, and seeing the effects on the various model outcomes, such as soil moisture, pH and weathering rate. In Table 4 the

simulation setup is presented. Here, all the possible combinations of the considered factors are listed along with the corresponding sections in which the results are discussed. First, some less realistic combinations of rainfall seasonality, soil type and crop cycle are taken into account, with the aim of exploring the role of each of them on EW dynamics. The last four simulations presented in Section 6.2.4 are related to the analysis of EW dynamics at the four selected locations, selecting the most likely combination of soil type and crop cycle with rainfall seasonality for each considered place.

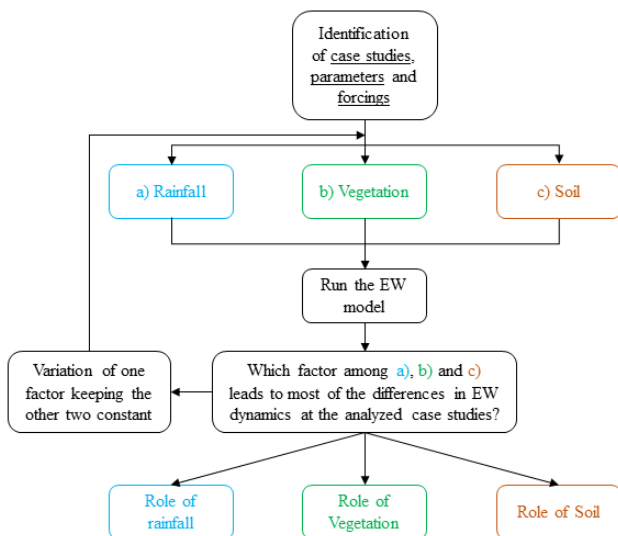


Figure 46 - Flow chart of the employed procedure for the case study of the EW model described in Cipolla, et al. [31].

Table 4 - Simulation outline with all the explored combinations of the analyzed factors.

	Simulations	Crop	Soil	Location	Output (Heatmaps)
Rainfall seasonality (Section 6.2.1)	1	Corn	Clay loam	Sicily (California)	Padan plain/Sicily and Iowa/California
	2			Padan plain (Iowa)	
	3		Silty clay loam	Sicily (California)	Padan plain/Sicily and Iowa/California
	4			Padan plain (Iowa)	
	5	Wheat	Silty clay loam	Sicily (California)	Padan plain/Sicily and Iowa/California
	6			Padan plain (Iowa)	
	7		Clay loam	Sicily (California)	Padan plain/Sicily and Iowa/California
	8			Padan plain (Iowa)	
		Location	Crop	Soil	Output (Heatmaps)
Soil type (Section 6.2.2)	9	Sicily	Wheat	Clay loam	Clay loam/Silty clay loam
	10			Silty clay loam	
	11	Padan plain	Corn	Clay loam	Clay loam/Silty clay loam
	12			Silty clay loam	
	13	Iowa	Corn	Clay loam	Clay loam/Silty clay loam
	14			Silty clay loam	
	15	California	Wheat	Clay loam	Clay loam/Silty clay loam
16	Silty clay loam				
		Location	Soil	Crop	Output (Heatmaps)
Crop cycle (Section 6.2.3)	17	Sicily	Clay loam	Wheat	Corn/Wheat
	18			Corn	
	19	Padan plain	Silty clay loam	Wheat	Corn/Wheat
	20			Corn	
	21	Iowa	Silty clay loam	Wheat	Corn/Wheat
	22			Corn	
	23	California	Clay loam	Wheat	Corn/Wheat
24	Corn				
		Location	Soil	Crop	Output (Heatmaps)
Most frequent scenarios (Section 6.2.4)	25	Sicily	Clay loam	Wheat	Output (Heatmaps)
	26	Padan plain	Silty clay loam	Corn	
	27	Iowa	Silty clay loam	Corn	
	28	California	Clay loam	Wheat	

## 6.1.2 Study area and data

The real case studies here taken into account involve two different locations in Italy (i.e., Sicily, in the south, and the Padan plain, in the north) and two more in the USA (i.e., California, in the south-west, and Iowa, in the north-central area). Figure 47 shows the areas possibly devoted to olive amendment, that is the one indicated as “cropland” within the Copernicus land cover maps [153]. Especially for Iowa and the Padan plain, the cropland area takes up most of the entire study area. This is a positive aspect in perspective of

a real EW application, given that this strategy requires large land areas to result in significant carbon sequestration amounts [116]. The most common crops for these croplands according to the USDA crop production maps ([https://ipad.fas.usda.gov/rssiw/ai/global\\_cropprod.aspx](https://ipad.fas.usda.gov/rssiw/ai/global_cropprod.aspx)), namely the wheat crop for Sicily and California and the corn crop for Padan plain and Iowa, are here considered. As in Cipolla, *et al.* [31], all simulations are related to a unit ground area of homogeneous soil, vegetation and rainfall characteristics, delimited by the active root zone depth of the involved crop. The next subsections are devoted to the extraction of the parameters related to the investigated factors needed to carry out the simulation outline.

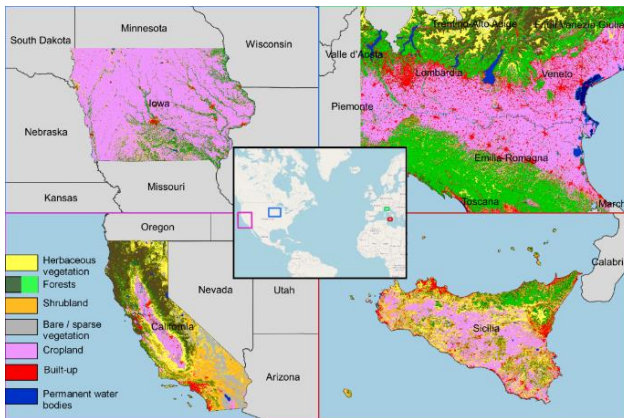


Figure 47 - Locations of the areas possibly devoted to olivine amendment in the places under study within the Copernicus land cover maps. In particular, cropland areas in the panels of Padan plain and Iowa are related to corn crop, while those in the panels of Sicily and California

to the wheat crop. The central box showing the locations of all the four sites contains the OpenStreetMap as background.

### 6.1.2.1 Rainfall seasonality

Rainfall is the forcing of the EW model and its seasonality is one of the investigated factors for the applications presented in this study since it directly affects soil moisture dynamics, strongly connected to EW [31,32]. Rainfall is here modeled as a marked Poisson process, where the average depth and the frequency of events are defined by the parameters  $\alpha$  and  $\lambda$ , respectively, whose product (if expressed in per year) provides the MAP [136]. The former,  $\alpha$ , represents the average rainfall depth of occurred daily rainy events, while  $\lambda$  is the ratio between the number of rainy days and the total number of days. These parameters have been estimated at a monthly scale from daily rainfall data recorded from 2000 to 2020 by the SIAS (*Servizio Informativo Agrometeorologico Siciliano*) rain gauge network for Sicily, the Eraclito dataset of *ARPA Emilia Romagna* for the Padan plain and the USGS (United States Geological Survey) in the states of Iowa and California. Given the point scale application of the EW model, data collected by a single rain gauge representative of the area under study have been considered for the analyses. Rainfall parameters  $\alpha$  and  $\lambda$  have been obtained at monthly scale, providing their seasonal variation within the year (see Figure 48). In particular, Sicily (panel a) and California (panel b) are characterized by similar pattern of

$\alpha$  and  $\lambda$ , since they both reach a minimum during summer months, which are usually rainless, and a peak in winter months, especially between November and January [75]. Regarding the Padan plain (panel c) and the state of Iowa (panel d), rainfall seasonality is less evident than in the other locations, especially in the case of the Padan plain. In this latter, in fact, the two parameters are not perfectly in phase since there is a shift of about two months. For the Iowa state, instead, the highest values of both  $\alpha$  and  $\lambda$  occur during spring and summer months. This different rainfall seasonality, respect to the cases of Sicily and California, has a relevant effect on EW dynamics, especially when considered along with crop phenology. Considering that there is a not too great MAP difference between the sites under study (i.e., MAP equal to about 600 mm for Sicily and California and to about 750 mm for the Padan plain and Iowa), it is important to focus on the different rainfall seasonality, since it may lead to particular dynamics of soil pH, olivine weathering rate and, in turn, carbon sequestration.

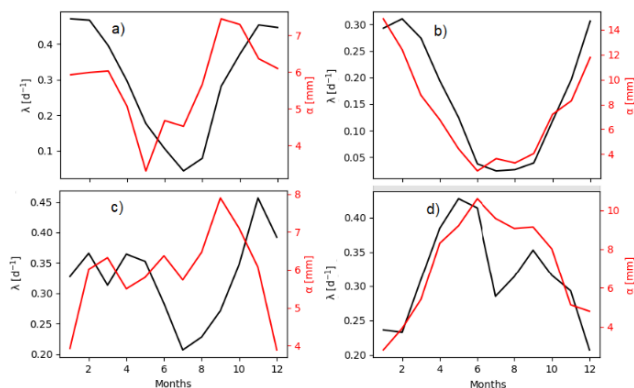


Figure 48 - Values of  $\alpha$  and  $\lambda$  rainfall parameters from January (i.e., month indicated with 1) to December (i.e., month indicated with 12) for a) Sicily, b) California, c) Padan plain and d) Iowa.

### 6.1.2.2 Soil type and composition

The soil type for the four sites under study has been derived from the USDA soil texture triangle, that requires as input the silt, sand and clay fractions. These have been extracted from the *Soil Grids* project maps [154] considering the areas covered by croplands and reaching a depth equal to the active root zone of 40 and 60 cm for the corn and wheat crops, respectively [155]. Then, the QGIS plugin *Soil Texture* has been used to derive the soil type in the USDA soil texture triangle. The most frequent soil types for the four considered sites have been here considered. These are the clay loam soil for Sicily and California and the silty clay

loam soil for the Iowa state and the Padan plain. Following previous studies [156,157], the main properties of these two soil types, such as porosity, the soil moisture values characteristic of the soil water retention curve, the hydraulic conductivity at saturation and the bulk density have been extracted and presented in Table 5. It is worth to specify that, for the calculation of the soil moisture at hygroscopic point, the wilting point and at incipient stress, the soil water retention curve formulation defined by Clapp and Hornberger [156] has been used, supposing soil water potentials of -10 MPa, -3 MPa and -0.03 MPa respectively, as done in Laio, *et al.* [157].

*Table 5 - Properties of the clay loam and silty clay loam soils used in the model.*

		<b>Clay Loam</b>	<b>Silty Clay Loam</b>
Soil porosity	<b>n [-]</b>	0.476	0.477
Soil moisture at hygroscopic point	<b>s<sub>h</sub> [-]</b>	0.394	0.319
Soil moisture at wilting point	<b>s<sub>w</sub> [-]</b>	0.453	0.373
Soil moisture at incipient stress	<b>s* [-]</b>	0.64	0.56

Soil moisture at field capacity	$s_{fc}$ [-]	0.821	0.75
Saturation hydraulic conductivity	$K_s$ [ $m\ d^{-1}$ ]	0.212	0.146 <sub>9</sub>
Pore size distribution index	$b$ [-]	8.52	7.75
Bulk density of soil	$\rho_b$ [ $kg\ m^{-3}$ ]	1450	1500

Regarding the soil organic carbon content, the Global Soil Organic Carbon map (GSOCmap) of the Food and Agriculture Organization of the United Nations (FAO) (<http://54.229.242.119/GSOCmap/>) [158] has been used, representing a global spatial distribution of the organic carbon content, expressed in  $ton\ ha^{-1}$ , of the first 30 cm soil layer. This could be assimilated as the steady state carbon concentration in the litter and humus pools reached by the carbon module of the model, assuming in a simplified way the same carbon distribution over the whole active root zone depth, given that soil organic carbon is not homogeneously distributed.

Since cation exchanges between the dissolved ions and soil colloids play a pivotal role in pH time dynamics, the total cation exchange capacity (CEC) per unit mass of the soil has been set based on site specific values reported in the CEC maps of Ballabio, *et al.* [159] for the two sites in Italy and by the United States Department of Agriculture

(USDA) data for Iowa and California [160,161]. In particular, a total CEC equal to 50 cmol kg<sup>-1</sup> for Sicily and the Padan plain and to 35 and 25 cmol kg<sup>-1</sup> for Iowa and California has been considered.

The background weathering flux represents the losses of hydrogen ions due to the chemical weathering process of all the minerals that are naturally present in the soil. In general, locations with the same soil type, vegetation and climate characteristics may lead to different weathering rates according to the minerals within the soil that, with different rates, consumes H<sup>+</sup> ions available in soil water. This weathering flux can be estimated on the base of the mineral composition of the soil and of the type of the existing bedrocks. This last information has been extracted from the lithological map presented in Hartmann and Moosdorf [162], representing the nature of bedrock at the global scale. The exploration of the lithological information in correspondence of the cropland areas for the four considered sites, highlights that Sicily and the Padan plain are generally characterized by carbonate sedimentary rocks (e.g., calcite), although alluvial deposits occupy a great part of the Padan plain, while the other two sites in the USA mainly present siliciclastic sedimentary rocks (e.g., quartz). This results in a very different background weathering rate between places in the two continents, since carbonate rocks have a much faster dissolution rate constant than siliciclastic rocks. Indeed, considering Lasaga [100] and Plummer, *et al.* [163], at 25°C and pH equal to 5, calcite and quartz minerals are characterized by a dissolution rate constant of about 10<sup>-5</sup> and 10<sup>-13</sup> mol m<sup>-2</sup> s<sup>-1</sup>, respectively.

This factor certainly has a relevant effect on olivine dissolution dynamics since it affects soil pH dynamics before olivine amendment. However, soil pH may depend on other factors that are not considered in the EW model (i.e., the presence of fertilizers, the action of microorganism, such as fungi and bacteria, or the action of other minerals that may release or take up  $H^+$  ions).

To sum up these aspects in a single term, i.e., the background weathering flux, the above-mentioned dissolution rate constants have been modified in order to achieve steady state soil pH values typical of the four sites under study. These are reported in Ballabio, *et al.* [159] for Sicily and the Padan plain (i.e., a value ranging from 7.2 to 8.8) and provided by the USDA [160,161] for California (i.e., a value around 7) and Iowa (i.e., a value around 6). This operation ended up with three values of background weathering flux, a faster one for the case studies in Italy (dissolution rate constant of  $10^{-5} \text{ mol m}^{-2} \text{ s}^{-1}$ ), a lower value for California (dissolution rate constant of  $10^{-6} \text{ mol m}^{-2} \text{ s}^{-1}$ ) and an even slower one for Iowa (dissolution rate constant set to  $10^{-8} \text{ mol m}^{-2} \text{ s}^{-1}$ ). Such an in-depth characterization of the background weathering flux, based on real measurements, allows to have a realistic starting conditions of the soil before olivine amendment and, in turn, to get a more accurate estimation of olivine weathering rate and carbon sequestration.

### 6.1.2.3 Crop cycle

In order to investigate the role of crop cycle on the EW dynamics, the monthly variation of the crop coefficient ( $K_c$ ) has been considered in the modeling framework. In particular, for each of the development stage, a single crop coefficient, for each crop type and climatic area, has been extracted from FAO guidelines, thus deriving its variability across the year (i.e., solid lines in Figure 49). Regarding the considered crops, the wheat plant date is in November for Sicily, December for California and October for Padan plain and Iowa. The total crop stage lasts 240, 180 and 335 days respectively. Corn is usually planted in April and the total crop stage is composed of 170 days, both in Padan plain and Iowa. Regarding Sicily and California, the corn crop cycle is the same to that of Padan plain and Iowa, except for the end-of-season stage that lasts 30 days instead of 50 and, therefore, the total cropping season lasts for 150 days.

This seasonal pattern of the crop coefficient inevitably affects the transpiration water losses that are computed as:

$$T(s) = \begin{cases} 0, & 0 \leq s < s_w \\ \frac{s-s_w}{s^*-s_w} fET_0(t), & s_w \leq s < s^* \\ fET_0(t), & s^* \leq s \leq 1 \end{cases} \quad (87)$$

where  $ET_0(t)$  is the reference evapotranspiration, which is computed using the Penman-Monteith equation for a reference crop. The annual pattern of this variable, for

the four selected locations, has been extracted from the high-resolution database provided by Singer, *et al.* [164]. This allows to take into account the role of seasonal variations in transpiration and evaporation rates in well-watered conditions, also including the effects of different air temperature among the selected case studies. The term  $f$  of equation (87) represents the rate of canopy cover over the entire study area, that is complementary to the area covered by bare soil. We here assume it as the ratio between the crop coefficient, at a certain time, and the maximum crop coefficient, which is reached at the mid-season stage. The bare soil evaporation is evaluated as follows:

$$E(s) = \begin{cases} 0, & 0 \leq s < s_h \\ \frac{s-s_h}{s_{fc}-s_h} (1 - f(t))ET_0(t), & s_h \leq s < s_{fc}, \\ (1 - f(t))ET_0(t), & s_{fc} \leq s \leq 1 \end{cases} \quad (88)$$

The total evapotranspiration water losses are therefore computed as the sum between bare soil evaporation and crop transpiration. The crop coefficient variation across the year, represented in Figure 49, is determined as:

$$K_c(t) = \begin{cases} K_{c,ini}, & t \leq f_i \\ \frac{K_{c,max}-K_{c,ini}}{f_d-f_{ini}}(t-f_i) + K_{c,ini}, & f_i < t \leq f_d \\ K_{c,max}, & f_d < t \leq f_{ms}, \\ \frac{K_{c,ls}-K_{c,max}}{f_{ls}-f_{ms}}(t-f_{ms}) + K_{c,max}, & f_{ms} < t \leq f_{ls} \\ K_{c,ls}, & t = f_{ls} \end{cases} \quad (89)$$

where  $f_i$ ,  $f_d$ ,  $f_{ms}$  and  $f_{ls}$  are the time period related to the different crop stages (i.e., initial, development, maturity and late seasons, respectively), while  $K_{c,ini}$ ,  $K_{c,max}$  and  $K_{c,ls}$  are the corresponding crop coefficient values, according to FAO guidelines.

Regarding the added carbon to the soil from vegetation (ADD), the byproducts released as root exudates and the input of litter after crop harvest, that depends on the adopted agricultural practice, have been considered. Since root exudation products are connected to the vegetation cycle, because they consist of carbon-based compounds deriving from plant metabolic activity that are released from living roots [151], their contribution to the carbon input to the soil can be modeled as a slight linear increase from the background ADD (i.e., the starting point of the ADD axis in Figure 49) to a minimum ADD value during the initial growing stage (i.e., from November, 1<sup>st</sup> for 30 days for wheat in Sicily, from December, 1<sup>st</sup> for 20 days for wheat in California, from October 1<sup>st</sup> for 160 days for wheat in Padan plain and Iowa and from April 1<sup>st</sup> for 30 days for corn in all four locations) and with a more relevant growth

in the development phase (i.e., from December, 1<sup>st</sup> for 140 days for wheat in Sicily, from December, 20<sup>th</sup> for 60 days for wheat in California, from March 9<sup>st</sup> for 75 days for wheat in Padan plain and Iowa and from May 1<sup>st</sup> for 40 days for corn in all four locations), until reaching a maximum ADD value at which this carbon input remains stable during the maturity period (i.e., from April, 19<sup>th</sup> for 40 days for wheat in Sicily, from February, 17<sup>th</sup> for 70 days for wheat in California, from May 23<sup>th</sup> for 75 days for wheat in Padan plain and Iowa and from June 9<sup>th</sup> for 50 days for corn in all four locations). Lastly, a linear decrease towards the background ADD value has been assumed at the end-of-season stage for vegetation (i.e., from May, 29<sup>th</sup> for 30 days for wheat in Sicily, from April, 28<sup>th</sup> for 30 days for wheat in California, from August 6<sup>th</sup> for 25 days for wheat in Padan plain and Iowa, from July 29<sup>th</sup> for 50 days for corn in the Padan plain and Iowa and from July 29<sup>th</sup> for 30 days for corn in Sicily and California). After the end of season, in correspondence of crop harvest, the soil is amended with plant litter, leading to a sudden increase in the carbon input, as it is visible in the dashed lines of Figure 49. This carbon input, then, linearly decreases until reaching the background ADD value at the beginning of the next crop stage, since litter is progressively degraded by the biomass. The constant background ADD is considered in order to take into account eventual other amendments (e.g., manure) or carbon residues (e.g., death roots or stems) from previous cycles. The ADD values shown in Figure 49, typical of root exudation and added litter, have been defined with the aim to achieve the typical carbon concentration in

the soils under study (see Table 6) from the organic matter balance module of the EW model and also looking at the typical carbon input from plants residues presented in Bruni, *et al.* [165].

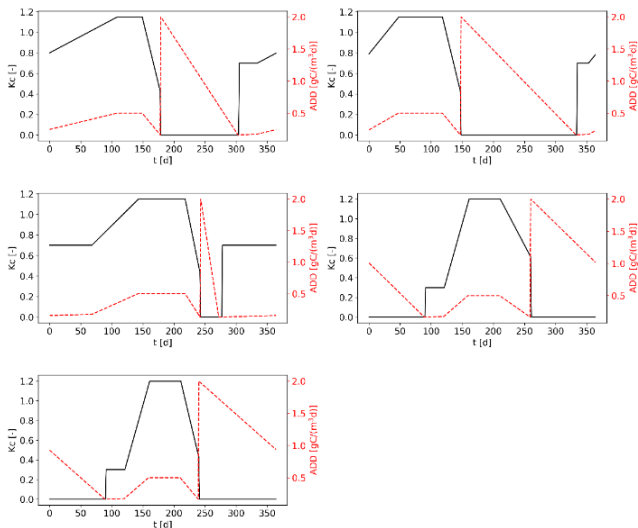


Figure 49 - Seasonal variability of the crop coefficient and the added carbon from vegetation for a) wheat crop in Sicily, b) wheat crop in California, c) wheat crop in the Padan plain and Iowa, d) corn crop in Padan plain and Iowa and e) corn crop in Sicily and California.

### 6.1.2.4 Temperature

Since the case studies are situated in different places of the world, it is important to consider the effect of different air and soil temperature on EW. Regarding air temperature, its effect is included in the definition of potential evapotranspiration rate, as explained in Section 6.1.2.3. Soil temperature, instead, affects olivine weathering rate, given that it leads to the variation of the dissolution rate constant (see Section 4.1.1 for more details). This aspect has been here included by considering the global gridded monthly average soil temperature database [166] at 1 km resolution for two different soil layers (i.e., 0-5 and 5-15 cm). Once derived the average temperature with respect to depth at a monthly scale, the seasonal variability of the olivine dissolution rate constant has been achieved by means of the Arrhenius law. This certainly affects the derivation of the weathering rate, which varies as a function of temperature, soil moisture and pH.

Figure 50 displays the seasonal variability of the average soil temperature and olivine dissolution rate constant for the four considered case studies. It is here possible to observe that all sites present minimum temperatures in the early and late part of the year and a peak during summer months. However, as expected, Sicily and California are characterized by higher monthly mean temperatures with respect to the Padan plain and Iowa, respectively. This translates in a greater average dissolution rate constant of olivine, which assumes values higher than

$1 \times 10^{-10} \text{ mol m}^{-2} \text{ s}^{-1}$  only when soil temperature is greater than  $25^\circ\text{C}$ .

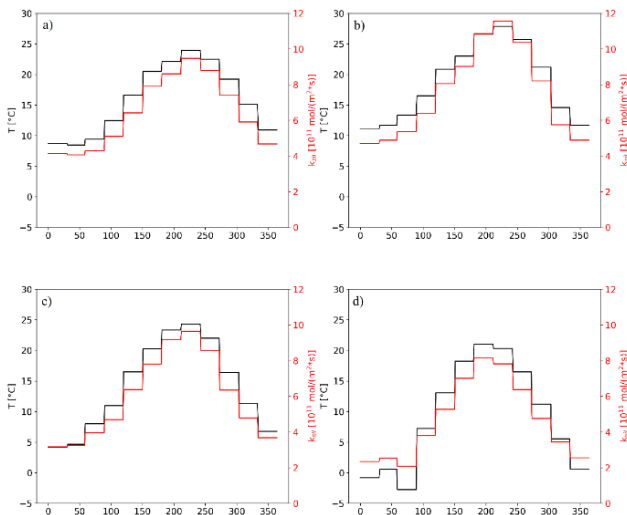


Figure 50 – Seasonal variability of the average soil temperature and olivine dissolution rate constant for a) Sicily, b) California, c) Padan plain and d) Iowa.

### 6.1.2.5 Irrigation

Since corn is planted in April and concentrates the reproductive and maturity phases during the driest periods in the Mediterranean climate (i.e., Sicily and California), it is here assumed that an irrigation contribution would be necessary to avoid stress conditions for plants, that would

badly affect productivity. Following previous studies [167,168], a stress-avoidance irrigation, a scheme designed to avoid stress conditions for vegetation, has been imposed, activating it when soil moisture becomes less than the point of incipient stress. According to this scheme, an irrigation volume is released to the crop only when crop coefficient is different than zero and when soil moisture becomes less or equal to the point of incipient stress. The provided irrigation volume  $\Delta s$  (i.e., the soil moisture gap) is equal to 0.2, but with the condition that soil moisture remains under the value at field capacity, in order to avoid wasting water due to percolation through deep soils. Figure 51 displays a typical stress-avoidance irrigation scheme for corn crop planted in a silty clay loam soil in California and the resulting yearly soil moisture and pH time-series with and without the irrigation contribution. Here, 15 irrigation interventions, over the 150 days of the vegetation cycle, are needed to bring soil moisture above the point of incipient stress, when there is a lack of rainfall and transpiration losses are significant. In the case of Figure 51, the total annual volume of supplied water is almost equal to 550 mm, to compensate the annual transpiration loss of the crop equal to about 500 mm. The effects of irrigation are clearly visible in the soil moisture time-series (panel c of Figure 51), since it ranges between the value at incipient stress and the field capacity in the days ranging from about 100 to almost 250 (i.e., when the crop reproductive and mid-season phases are concentrated). In panel d) it is visible that irrigation results in a significant reduction of soil pH during

all the vegetative phases, compared with the case in which no irrigation is provided.

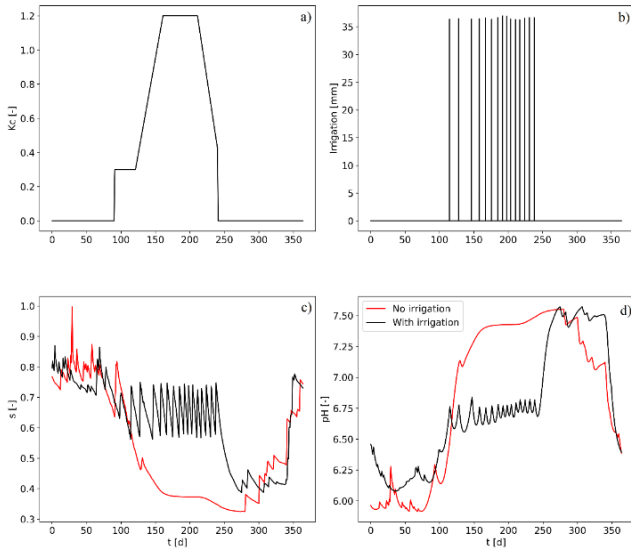


Figure 51 - Stress-avoidance irrigation procedure for corn crop planted in a silty clay loam soil in California. Panel a) represents the crop coefficient, b) the yearly soil moisture time-series with and without irrigation, c) the specific volume of water added by irrigation and d) the yearly pH time-series with and without irrigation.

## 6.2 Results

This section is related to a comparison of EW dynamics in the four sites, thus recognizing the role of the specific

factor, among rainfall seasonality, soil type and composition and crop phenology, that most affects EW dynamics. This analysis will inform on the best combination of rainfall seasonality, soil and vegetation type, and soil composition that is most suitable to olivine amendments; the location having the greatest carbon sequestration potential, among the four analyzed, can also be defined. All results are presented in the form of heatmaps, allowing to observe the seasonal variability of the presented variables, year by year until 10 years after olivine amendment.

### 6.2.1 The role of rainfall seasonality on EW dynamics

This section is devoted to explore the role of rainfall seasonality on EW. To this regard, some pairwise comparisons of EW dynamics achieved for the case studies in Italy and those in the USA, given the different rainfall seasonality between Sicily and the Padan plain and California and Iowa, are presented. Simulations, whose analyzed scenarios can be consulted from Table 4, have been carried out by fixing the soil and the vegetation type and varying the location of the considered case study.

In the following, heatmaps of the ratios between soil properties (soil moisture, pH, or weathering rate) in two different locations (i.e., Padan plain (PP) and Sicily (SI) in

Figure 52 and Iowa (IA) and California (CA) in Figure 53) are presented. In both figures, the panels in the first row are related to the corn crop (C) planted in a clay loam (CL) soil, those in the second row to the corn (C) crop within the silty clay loam (SCL) soil, panels in the third row to wheat crop (W) planted in a silty clay loam soil (SCL) and, lastly, those displayed in the last row to wheat (W) crop within a clay loam (CL) soil. The panels in the last row of the figure, instead, display the average daily ratios of the three considered variables of the model. From Figure 52, particularly the cases when corn crop is considered, the soil moisture ratio presents values lower than 1 during the summer season (i.e., Julian day between 150 to about 250) meaning that, in those days, soil moisture is higher in Sicily than in the Padan plain. In the rest of the year, by contrast, soil in Padan plain is as wet as in Sicily, except for some days around the Julian day 300, meaning that the ratio maintains to values equal to about 1. The effects of multiple irrigation interventions are also visible in the pH ratio heatmaps related to corn crop in Figure 52 since, during the irrigation period, it is higher than 1, corresponding to a more acidic soil in Sicily than in the Padan plain. These considerations about soil moisture and pH affect weathering rate dynamics, which is higher in Sicily, especially during summer, due to irrigation. The average daily weathering rate ratio, in fact, assumes values higher than one only for a short period around the 300th Julian day.

Regarding the wheat, soil moisture is higher in the Padan plain respect to Sicily during summer, given the near absence of rainfall in Sicily in this period. Therefore, soil

tends to be more acidic and weathering rate tends to be higher (e.g., average daily weathering rate ratio higher than 1). In the rest of the year, values of the ratio of the weathering rate between the two places, tend to be slightly less than 1, translating in similar olivine dissolution dynamics, even though more favorable in Sicily. It is hence worth to notice that, at least for the two places under study in Italy, rainfall seasonality alone does not produce significant changes in EW dynamics (i.e., weathering rate average daily ratio not too far from 1), if one considers the same vegetation and soil type and composition. However, irrigation in Sicily during the summer period leads to significantly more favorable conditions of olivine dissolution.

For the case studies in the USA, for instance looking at the wheat crop, Iowa seems to provide significantly wetter and more acidic soil conditions, resulting in greater weathering rates that, around the Julian day 300, may reach values twenty times higher than those achieved in the case of California. Comparing rainfall seasonality in these two countries (panels b and d of Figure 48), it is worth to notice that there are higher values of precipitation distribution (i.e.,  $\alpha$  and  $\lambda$  parameters) for Iowa with respect to California, leading to higher soil water content also given by the low transpiration losses of the crop, that in the above-mentioned days is in the initial growing stage (see panel c of Figure 49). On average, over the considered 10 years, weathering rates derived for Iowa are about seven times higher than those in California under the two considered

soil types, resulting from an average soil moisture/pH ratio slightly greater/less than 1. Regarding the corn crop, the same considerations made for the Italian case studies may be done here, since as in Sicily it requires to be irrigated during summer in California, given the scarcity of precipitation. Indeed, during this season, the soil moisture/pH average daily ratio is lower/higher than 1, leading to a slightly faster dissolution rate in California. In the last part of the year, Iowa provides wetter and more acidic conditions, given the higher precipitation distribution (i.e., similar  $\alpha$  but more than double  $\lambda$  around the Julian day 300).

It is thus possible to affirm that, considering the same soil and vegetation, for the Italian case-study applications, rainfall seasonality leads to small differences in EW dynamics. In the US selected locations, instead, olivine dissolution is significantly faster in Iowa, given the significantly higher values of precipitation distribution. It is hence valuable to affirm that, despite the similar MAP of the four analyzed case studies, rainfall seasonality is fundamental to characterize olivine dissolution dynamics, especially when looking at its interaction with crop phenology. Moreover, more relevant differences in terms of MAP would result in very different EW dynamics [32], and may also contribute to emphasize the effect of rainfall seasonality on olivine dissolution, thus the relevant role of climatic condition on EW.

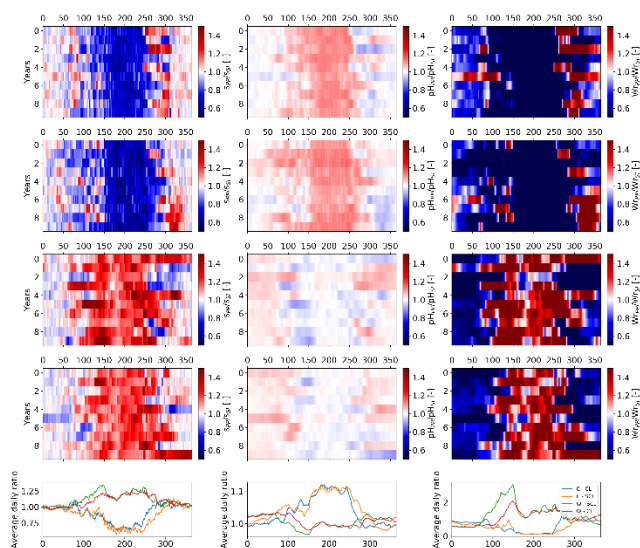


Figure 52 - Time-series heatmaps of the ratio between soil properties (soil moisture, pH, or weathering rate) in two different locations (i.e., Padan plain (PP) and Sicily (SI)) computed within 10 years after olive addition. These are related to corn planted in a clay loam soil (panels in the first row of the figure), corn crop planted in a silty clay loam soil (panels in the second row of the figure), wheat crop planted in a silty clay loam soil (panels in the third row of the figure) and wheat crop planted in a clay loam soil (panels in the fourth row of the figure). The average daily ratios of the three considered variables are shown in the last panel of the figure.

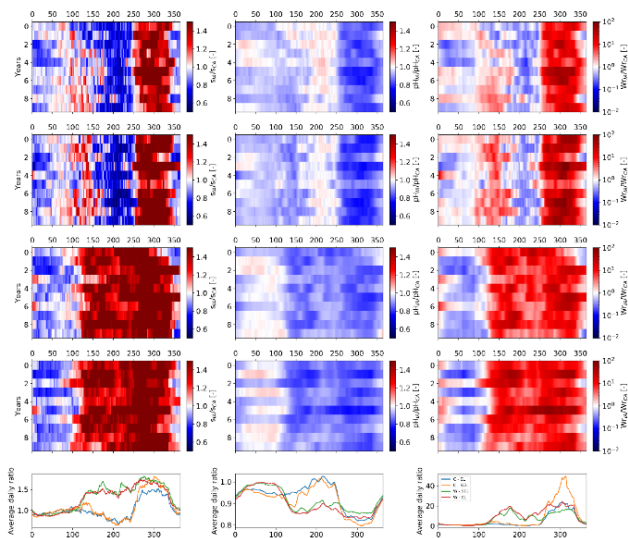


Figure 53 - Time-series heatmaps of the ratio between soil properties (soil moisture, pH, or weathering rate) in two different locations (i.e., Iowa (IA) and California (CA)) computed within 10 years after olive addition. These are related to corn planted in a clay loam soil (panels in the first row of the figure), corn crop planted in a silty clay loam soil (panels in the second row of the figure), wheat crop planted in a silty clay loam soil (panels in the third row of the figure) and wheat crop planted in a clay loam soil (panels in the fourth row of the figure). The average daily ratios of the three considered variables are shown in the last panel of the figure.

## 6.2.2 The role of soil type on EW dynamics

In this section the role of different soil types on EW dynamics is explored through some analyses carried out considering the same location and vegetation type and varying the two different soils considered in this study (clay loam soil and silty clay loam). These two soils have been compared, despite they have very similar characteristics, since they are the most frequent in the four sites. Figure 54 displays heatmaps of the ratio between soil moisture, pH and weathering rate achieved considering the clay loam soil and those obtained with the silty clay loam one. Panels in the first row of the figure are related to Sicily and the wheat crop, those in the second row concern the Padan plain with the corn crop, those in the third row the case of Iowa and the corn crop and, lastly, in the fourth row results related to California and the wheat crop are plotted. The average daily ratios are presented in the last row of the figure. Results highlight that the clay loam soil leads to a larger soil water content in most of the cases as compared to the silty clay loam. This is due to the fact that the latter soil type is characterized by lower soil moisture at the hygroscopic and wilting point respect to the former one and, for this reason, evapotranspiration losses are higher, as these values are exceeded most frequently. Similar conclusions can be drawn for the soil moisture value at the field capacity that involves water losses for leaching. This aspect is translated in a more acidic soil and a faster olivine dissolution under the clay loam soil. Apart from some spikes, occurring in

some specific days, weathering rates obtained with the clay loam soil tends to be about twice as high as those obtained with the silty clay loam soil at all four locations. This small difference is certainly due to the very similar characteristics of the clay loam and silty clay loam soils (see Table 5 for more details), that result in similar hydrological fluxes (e.g., infiltration and leaching rates), water balance and all the derived variables (i.e., pH and dissolution rate).

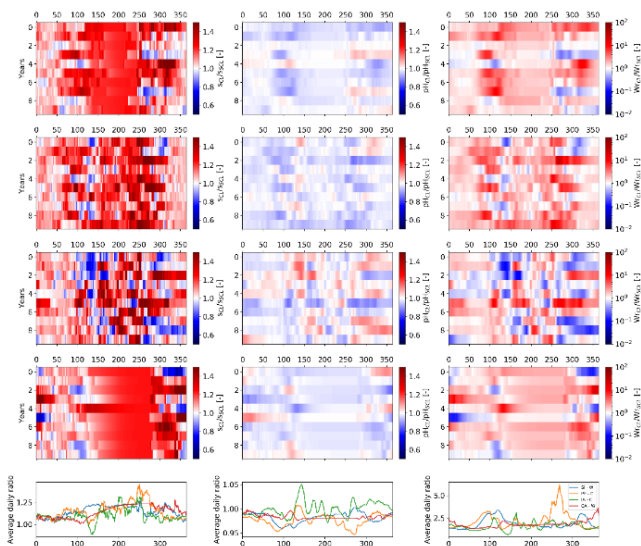


Figure 54 - Time-series heatmaps of the ratio between soil moisture, pH and weathering rate achieved considering the clay loam soil and those related to the silty clay loam soil. The heatmaps are related to a time period of 10 years after olive addition. These are related to Sicily with wheat crop (panels in the first row of the figure), Padan plain with corn crop (panels in the second row of the figure), Iowa with corn crop (panels

*in the third row of the figure) and California with wheat crop (panels in the fourth row of the figure). The average daily ratios of the three considered variables are shown in the last panel of the figure.*

### 6.2.3 The role of vegetation on EW dynamics

Vegetation in general plays a significant role on EW dynamics, due to its acidifying effect given by the displacement of  $H^+$  to balance the cations taken from soil water as nutrients [19] and also because it provides the organic matter that, once decomposed, is one of the  $CO_2$  source in the system [125]. The type of vegetation, therefore, influences the time dynamics of soil moisture, pH and weathering rate given that the different crop phenology determines different dynamics of transpiration and added carbon.

Heatmaps in the same form of Sections 6.2.1 and 6.2.2 are presented in Figure 55. One can notice that, for the four considered locations and related soil types, corn and wheat crops lead to different EW dynamics. Looking at panels related to weathering rate ratio, corn crop leads to a weathering rate on average about four times higher than the one achieved for wheat crop when they are planted on a clay loam soil in Sicily and California (first and fourth row of the figure), while olivine dissolution dynamics are about the same comparing the two crops planted in a silty clay loam soil in the Padan plain and Iowa (second and third row of the figure), even though providing a slightly more favorable condition when corn crop is considered (annual average weathering rate daily ratio equal to about 1.5). The

greatest weathering rate considering the corn crop in Sicily and California are obtained during summer and are certainly due to the irrigation contributions. In the rest of the year, or in the cases of Padan plain and Iowa, where irrigation is not considered, crop phenology does not lead to significant differences in EW dynamics. Indeed, as one can notice from Figure 56, when any of the two crops is in the rest phase, apart from leaching, there are water losses due to bare soil evaporation, that are similar in magnitude to transpiration. It therefore happens that, when corn is in the rest phase and at the same time wheat is in its initial or mid-season stage, in the first case water losses are mainly governed by bare soil evaporation, while in the other one by crop transpiration. Since they have a similar magnitude, the fact that wheat and corn cycles are not in phase does not affect much water balance and, in turn, pH and weathering rate dynamics. The only one difference for which corn leads to a slightly faster olivine dissolution may be attributed to the smaller active root zone depth (i.e., 0.4 and 0.6 m for corn and wheat crop, respectively) that causes the soil to reach saturation more easily.

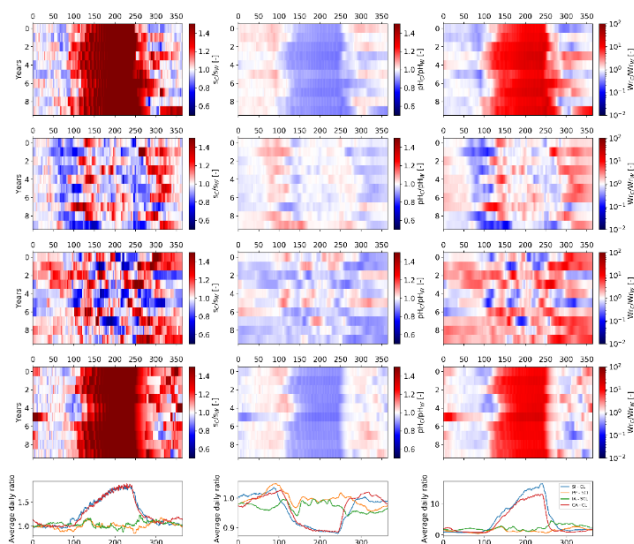


Figure 55 - Time-series heatmaps of the ratio between soil moisture, pH and weathering rate achieved considering the corn crop and those related to wheat. The heatmaps are related to a time period of 10 years after olivine addition. These are related to Sicily with clay loam (panels in the first row of the figure), Padan plain with silty clay loam (panels in the second row of the figure), Iowa with silty clay loam (panels in the third row of the figure) and California with clay loam soil (panels in the fourth row of the figure). The average daily ratios of the three considered variables are shown in the last panel of the figure.

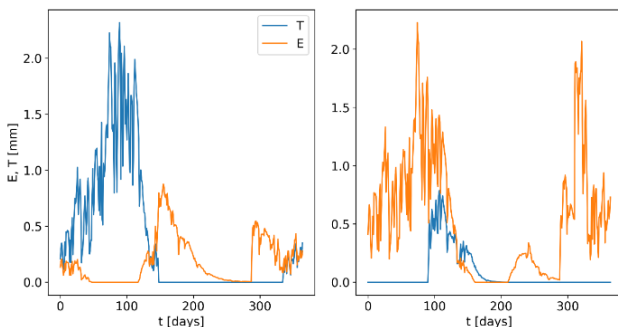


Figure 56 - Annual time-series for bare soil evaporation and crop transpiration in the case of a) wheat and b) corn planted in a clay loam in California. Corn is not irrigated in this case.

## 6.2.4 EW dynamics in Italy and USA

The time dynamics of soil moisture, pH and weathering rate in the selected sites in Italy and USA are shown in Figures 57 and 58, respectively. In all scenarios, the application of  $10 \text{ kg m}^{-2}$  of olivine, which is equivalent to the application of  $100 \text{ t ha}^{-2}$ , has been considered. Sicily and the Padan plain are characterized by a slightly different signal in the seasonality of soil moisture, pH and, in turn, weathering rate. The highest soil moisture values for Sicily occur usually in the first (i.e., before the Julian day 100) and in the last (i.e., from the Julian day 300 onwards) part of the year since those days are characterized by the greatest part of the total annual rainfall. Soil moisture assumes low values from the Julian day 100 to about 250 mainly due to

the scarcity of rainfall during the summer period [76]. On those days when soil moisture is high, pH and weathering rate reach their minimum and maximum values, respectively, as compared to the rest of the year, confirming the fact that weathering reactions are favored by wet and acid conditions [15,31,32,139].

For the Padan plain, the period with a generally higher soil moisture covers all winter and part of the autumn and spring months while, during summer, despite a relevant presence of rainfall (Figure 48), soil water content presents low values due to the high transpiration losses, given the occurrence of the corn crop mid-season (i.e., a peak of the crop coefficient). Comparing the annual average values of the analyzed variables in these two locations, one can observe as Sicily is characterized by a slightly faster olivine dissolution (an annual average weathering rate of  $4.14 \times 10^{-13} \text{ mol m}^{-2} \text{ s}^{-1}$  against the value of  $2.2 \times 10^{-13} \text{ mol m}^{-2} \text{ s}^{-1}$  achieved for the Padan plain), due to a lower annual average pH (7.26 in Sicily and 7.39 in the Padan plain) and higher mean annual soil moisture (0.62 in Sicily and 0.59 in the Padan plain).

A similar situation can be observed from the comparison between California and Iowa (Figure 58). Because of the similar rainfall seasonality and, of course, the same soil type and vegetation, it is thus possible to make a comparative analysis between Sicily and California and between Padan plain and Iowa regarding the time dynamics of soil moisture, pH and weathering rate. The greatest difference between Italian and US case studies can be observed in the achieved soil pH and olivine weathering

rate. Indeed, the two sites in USA are characterized by a lower annual average pH (6.11 in Iowa and 6.82 in California) and higher weathering rate ( $2.66 \times 10^{-12} \text{ mol m}^{-2} \text{ s}^{-1}$  in Iowa and  $1.53 \times 10^{-12} \text{ mol m}^{-2} \text{ s}^{-1}$  in California) with respect to the two sites in Italy. This is mainly due to the different lithological properties of the bedrocks and the mineral composition of the soil that lead to a more significant background weathering flux, hence  $\text{H}^+$  consumption and less acidic soil, in the sites in Italy than those in the USA, before olivine amendment [159-161]. The achieved order of magnitude of weathering rate reflects the values presented in the mesocosm experiment of Amann, *et al.* [24], which presents a condition very similar to the field environment. This aspect stresses the importance of a profitable calibration of the background weathering flux, cation exchange capacity and other components of the EW model, allowing to obtain realistic estimates of olivine dissolution dynamics.

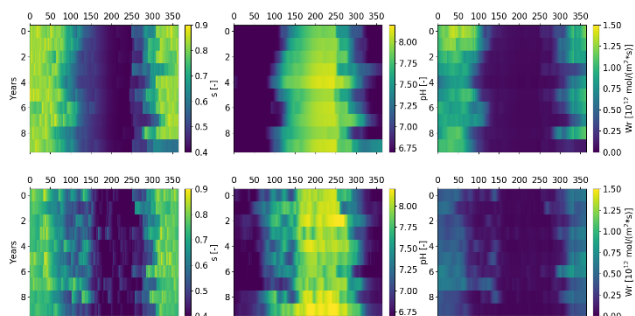


Figure 57 - Time-series heatmaps of soil moisture, pH and weathering rate computed within 10 years after olivine addition. These are related to wheat crop planted in clay loam soil for Sicily (panels in the first row of the figure) and corn crop in a silty clay loam soil for the Padan plain (panels in the second row of the figure).

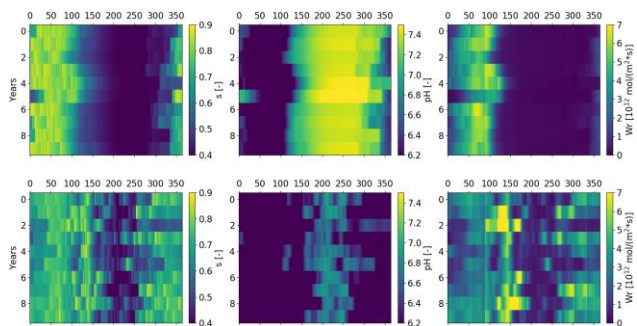


Figure 58 - Time-series heatmaps of soil moisture, pH and weathering rate computed within 10 years after olivine addition. These are related to wheat crop planted in clay loam soil for California (panels in the first row of the figure) and corn crop in a silty clay loam soil for the Iowa (panels in the second row of the figure).

The seasonal variability of the sequestered CO<sub>2</sub> related to the four sites under study is presented in Figure 59. This is calculated, as in Cipolla, *et al.* [32], as the leaching of the extra HCO<sub>3</sub><sup>-</sup> and CO<sub>3</sub><sup>2-</sup> produced by olivine dissolution, considering a time window of 10 years after olivine amendment. In general, the low monthly values of sequestered CO<sub>2</sub> for all case-studies are due to the generally low leaching rate, which is provided by low MAP values for all the considered sites. The annual average sequestered CO<sub>2</sub> resulted equal to 0.49 kg ha<sup>-1</sup> y<sup>-1</sup> for Sicily, 0.28 kg ha<sup>-1</sup> y<sup>-1</sup> for the Padan plain, 2.12 kg ha<sup>-1</sup> y<sup>-1</sup> for California and 5.21 kg ha<sup>-1</sup> y<sup>-1</sup> for Iowa. The values achieved for the US locations are lower but still comparable with those of Amann, *et al.* [24], that derived a sequestered CO<sub>2</sub> within the range 23-49 kg ha<sup>-1</sup> y<sup>-1</sup>, amending more than the double of olivine respect to our study (i.e., 22 kg m<sup>-2</sup>) in his mesocosm experiment and having similar conditions to the field environment. Taking into account the case of Iowa, which resulted in the highest carbon sequestration rate and is characterized by a cropland area covered by corn of about 56,000 km<sup>2</sup>, the annual average sequestered CO<sub>2</sub> could reach the value of about 0.03 Mt y<sup>-1</sup>, if the whole cropland area were amended with olivine. The case study in Sicily, instead, may sequester on average a mass of 0.00013 Mt y<sup>-1</sup>, if amending the total cropland area cultivated with wheat of about 265,000 ha. It is worth to specify that extending results achieved for a unit ground area to the whole region under study is just to provide an order of magnitude of sequestered CO<sub>2</sub>, given the great spatial heterogeneity of rainfall, soil properties and crop type.

As affirmed by Amann, *et al.* [24], extending the here achieved carbon sequestration rates at the global scale leads to a low carbon sequestration potential of the EW strategy, if compared with the annual global CO<sub>2</sub> emissions by fossil fuels. It is clear that, as demonstrated in our simulations, an accurate estimation of EW carbon sequestration potential requires an in-depth analysis at the global scale, in order to take the strong spatial variability of the process into account. This would also allow to explore EW dynamics in places of the world characterized by a higher MAP, thus with a greatest capability to sequester carbon. The rates of carbon sequestration presented in Beerling, *et al.* [116] at the global scale are about three order of magnitude higher respect to those achieved in this study. However, these are derived by means of a one-dimensional vertical reactive transport model that considers the CO<sub>2</sub> captured by EW as the dissolved inorganic carbon due to olivine dissolution (apart from the CO<sub>2</sub> emissions due to logistic operation), which is similar to the one that we called CO<sub>2,sw</sub> in Cipolla, *et al.* [169]. In effect, even in this our previous work we obtained about a three order of magnitude difference between the CO<sub>2,sw</sub> and the CO<sub>2,leached</sub>, but we believe that this latter is better connected to the actually sequestered CO<sub>2</sub>, given that some HCO<sub>3</sub><sup>-</sup> and CO<sub>3</sub><sup>2-</sup> dissolved in soil water due to olivine dissolution may react with H<sup>+</sup> forming the carbonic acid, thus potentially releasing CO<sub>2</sub> to the atmosphere.

The seasonal pattern of the sequestered CO<sub>2</sub> is very similar to the one of rainfall (Figure 48), highlighting the fact that hydrological processes play the most relevant role

in characterizing EW dynamics. On the other hand, seasonality of sequestered  $\text{CO}_2$  is not in phase with crop phenology. In fact, a great amount of rainfall, contextually occurring to low transpiration losses, leads to high soil water content, resulting in a high weathering rate, with a correspondence increase of  $\text{HCO}_3^-$  and  $\text{CO}_3^{2-}$  concentration produced by olivine reaction with  $\text{CO}_2$ , and a high leaching rate. Apart from that, the order of magnitude of sequestered  $\text{CO}_2$  depends a lot on the achieved weathering rates, which are strongly connected to soil pH before olivine amendment. In the case studies here presented, this effect is given by the background weathering flux, which provides more acidic conditions within California and Iowa respect to Sicily and the Padan plain.

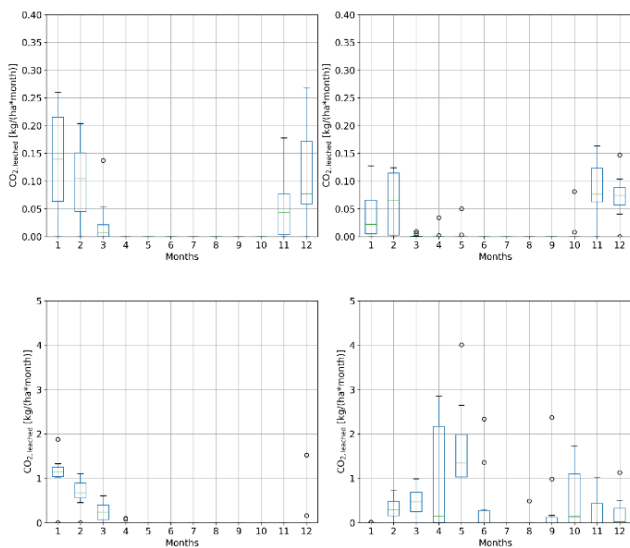


Figure 59 - Box plots representing the seasonality of the CO<sub>2</sub> sequestered by leaching of extra HCO<sub>3</sub><sup>-</sup> and CO<sub>3</sub><sup>2-</sup> produced by olivine dissolution, computed over the 10 years after olivine amendment. The plots are related to a) Sicily, b) Padan plain, c) California and d) Iowa.



## Conclusions

Since climate change is a current and relevant aspect, that is negatively affecting human society, there is a need to establish the causes and, above all, act on them to mitigate its consequences. It is known that anthropogenic activities, especially those that have been occurring during the industrial era, have led to a significant and rapid growth of greenhouse gases concentration in the atmosphere and, in turn, to the rise of the global surface temperature, aspect widely known as global warming. The climate alteration caused by human activities is thus defined by the scientific community as “anthropogenic climate change”. In the first chapter of this thesis a description of the most well-known effects caused by climate change is provided. These include expansion of dry areas, ice melting and sea level rise, the growing occurrence of weather extremes (i.e., drought and heavy rainfall events) and wildfires and also the global warming effect on food security.

In general, the anthropogenic global warming has been significantly contributing to the expansion of dry areas, hence to the loss of ecosystems and a worldwide increase of areas experimenting desertification [44]. This is not a positive aspect since desertification and water scarcity affects agriculture sector, with significant losses in crop production, and also forest cover losses. The increase in global surface temperature has also been leading to ice melting and consequent rise of sea level [68,70]. While the loss of permafrost can result in damages for living

ecosystems in the Arctic land, it is easy to imagine that sea level rise globally leads to an increasing extent of areas, especially coastal cities, vulnerable to floods. Another relevant aspect connected to climate change is the increase of different types of extremes, regarding in particular drought and heavy rainfall events [51,75,76]. Many studies, considering both local and global spatial scales, indeed, have shown that climate change has resulted in an increase of drought and short-duration and high-intensity rainfall events, due to an increase in the atmospheric instability, that possibly result in loss of human lives and damages for cities and infrastructures. Similar consideration can be done for wildfires [58] and food security [65]. For the first aspect, the increasing frequency and intensity of heatwaves has caused the risk of wildfires especially in forested areas, that are the most vulnerable ones. Regarding food security, instead, the global temperature and precipitation patterns, obtained under the most severe climate projections, are expected to lead to reduction of food production which can exacerbate the food security problems also because of a significant projected global population increase.

The second chapter of this work provided a distinction of the different climate mitigation measures in two categories, i.e., the SRM and the CDR techniques. The first are devoted to reduce the incoming solar radiation flux or the portion of it adsorbed by the Earth, resulting in the reduction of the global temperature rise due to the greenhouse effect. In this thesis, the most studied SRM technologies, namely the terrestrial albedo increases [9], the stratospheric aerosol injection [10] and the marine

cloud brightening increase [11], have been analyzed, taking into account their advantages and possible side effects. The CDR techniques, instead, act on sequestering the atmospheric CO<sub>2</sub> and store the carbon within it into oceans, vegetation or other terrestrial environments, thus attempting to lead the climate to a similar pre-industrial condition. In this chapter, some studies regarding afforestation and direct air capture have been described, despite the greatest part of the thesis is devoted to EW, one of the most promising CDR, also recognized as a NCS since it leads to sequester carbon by enhancing biochemical reaction rates that naturally happen in soils, by means of spreading highly reactive minerals, for instance silicates. In particular, Forsterite, better known as olivine, is able, especially under hot and humid conditions, to react with CO<sub>2</sub>, sequestering carbon in the form of carbonate and bicarbonate ions, that are in part leached away from the reference domain. EW is a fast growing area of research, therefore few studies are present in scientific literature about both experimental and modeling approaches.

To address this aspect, chapter 4 of this thesis describes a complex mathematical model, here developed, that connects biogeochemistry and ecohydrology to predict EW dynamics in soils [31,32]. The inclusion of soil moisture, plant and soil organic matter-nutrient interactions in a biogeochemical-EW model provides a novel perspective on the key processes controlling the dissolution dynamics of olivine in field conditions. The analyzed EW model, constituted by an explicit system of eight mass balance differential equations and an implicit algebraic system

consisting of twenty-two equations, simultaneously considers stochasticity in soil moisture, time dynamics in organic matter decomposition and soil chemistry, soil cation exchange capacity, olivine dissolution and CO<sub>2</sub> consumption. To highlight the fundamental interactions between water, soil chemistry and plants, EW was investigated in somewhat idealized conditions. Simplifying assumptions related to constant properties of rainfall, soil and vegetation could be easily relaxed. Running the EW model under varying MAP scenarios and considering a stationary precipitation and constant soil and vegetation parameters, resulted in the fact that hydrological processes are the most important factors leading to changes in EW dynamics; indeed, for MAP higher than 2000 mm weathering and leaching rates substantially increase, leading to great carbon sequestration rates and also increase of nutrients availability in soil water that, in turn, may affect plant productivity. Furthermore, the organic amendment was found to be effective only for very humid conditions since it resulted in a lower pH and higher weathering rate and carbon sequestration respect to the condition in which soil is not amended. This effect is instead negligible at MAP lower than 2000 mm.

These simulations are useful to isolate the role of different climatic, in this case rainfall, conditions on olivine dissolution and carbon sequestration dynamics, but however they do not reflect real case studies. In fact, introduction of rainfall seasonality and crop phenology, in addition to soil properties and composition, is fundamental to characterize EW dynamics in specific cropland areas of

the world. In chapter 6 of this thesis, some applications of the EW model related to two sites in Italy (i.e., Sicily in the south and the Padan plain in the north) and two in the USA (i.e., California in the West and Iowa in the North-Centre) are presented. Specific rainfall, soil and vegetation characteristics of the places under study have been extracted from several databases and a calibration of relevant parameters, i.e., the background weathering and cation exchange, with pH and cation exchange capacity data has been carried out. The main goal of the study was to understand how rainfall seasonality interacts with soil, vegetation types, and phenology and affects soil moisture, pH, and olivine weathering rate.

Analyzing the interactions among rain and crop properties was a great help for increasing the knowledge of EW process and its carbon sequestration potential. From the case-study applications presented in chapter 6, it is shown that a fundamental role in EW dynamics is played by rainfall distribution. Comparing EW yields in the case of a wheat crop planted in a clay loam soil for Sicily and California and a corn crop in a silty clay loam of the Padan plain and Iowa, we found that Sicily in the former case and Iowa in the latter are the most favorable for a possible EW intervention. Especially in these latter case studies, the sequestered  $\text{CO}_2$  is perfectly in phase with rainfall distribution. A great amount of rainfall, contextually occurring to low transpiration losses given that the sequestered  $\text{CO}_2$  is not in phase with crop phenology, leads to high soil water content, resulting in a high weathering rate, with a correspondence increase of  $\text{HCO}_3^-$  and  $\text{CO}_3^{2-}$

concentration produced by olivine reaction with CO<sub>2</sub>, and a high leaching rate, according to with these ions are taken away from the reference domain. Comparing EW dynamics at the four analyzed locations, Iowa is characterized by the greatest carbon sequestration potential, which results, apart from the interaction between rainfall seasonality and crop phenology, from the low background weathering flux, that leads to a more acidic soil before olivine amendment. However, as in the mesocosm experiment of Amann, *et al.* [24], low carbon sequestration rates have been achieved comparing to the annual global CO<sub>2</sub> emissions produced by the use of fossil fuels. To see if EW may significantly contribute to reach the goals fixed by the Paris Agreement, a detailed global scale analysis is required, so as to take into account places of the world with more suitable conditions to host this technique (i.e., warm and humid areas) than those presented in this study. Extending the carbon sequestration rates here achieved at the global scale, indeed, provides a very uncertain estimation, given the strong spatial variability of the EW process, due to great spatial variation of rainfall, soil properties and crops.

The EW model here developed can be extended in several directions. Indeed, it currently considers the most common macro-nutrients for plants, namely Ca<sup>2+</sup>, Mg<sup>2+</sup> and K<sup>+</sup> and also the micro-nutrient Na<sup>+</sup>; however, the model can be expanded to include the nitrogen and phosphorous cycles (e.g., Porporato, *et al.* [125] and D'Odorico, *et al.* [129]). In fact, a significant percentage of the global natural land area is nitrogen and phosphorous limited [170] and the demand of nitrogen and phosphorous is generally

considered to be high on a stoichiometric basis. The carbon module of the model assumes a simple balance between an input of carbon from vegetation and a first-order decomposition term, with constant carbon concentration in the biomass pool. More detailed carbon models can be analyzed and considered. For example, the recent non-linear “microbial models” may be used to couple microbial biomass, extracellular enzymes, and carbon substrate pools and take into account variations in the microbial carbon use efficiency in response to environmental conditions [171]. However, even if non-linear decomposition models may be more detailed over short time-scales, simple linear parametrizations may be more suitable when considering long time-scales [172]. One important source of uncertainty that affects the estimation of field weathering rate is connected to the distribution of olivine particles diameter, resulting from the grinding operation. In the EW model here presented, a single effective diameter has been considered, mainly for the sake of simplicity. In fact, tracking the actual evolution of particle size distributions would considerably increase the complexity and computational cost of the model. In general, as the particle size decreases, the weathering rate tends to increase at a quadratic rate, due to its quadratic relationship with the specific surface area. While it is tempting to use small particles, one should bear in mind that reducing particle size leads to higher grinding costs and CO<sub>2</sub> emissions (i.e., greater amount of energy needed to grind particles to a smaller size). In view of practical EW applications, a balance between these factors is fundamental to ensure that

the carbon sink of EW more than compensates for the CO<sub>2</sub> emissions and that the intervention is cost-effective.

The case-study applications of EW in croplands, presented in chapter 6 of this thesis, can be further improved by taking into account some processes that, at least at the moment, are neglected. For instance, the competition between fertilizers, composed of nitrates and phosphates, and olivine in the use of H<sup>+</sup> ions could be an important aspect to be characterized given that it may alter the olivine weathering reaction rate and, in turn, carbon sequestration. These, indeed, can be added to the soil to enhance soil fertility and plant productivity, given that many areas of the world present limitation in nitrogen and phosphorous [170]. Regarding nitrogen fertilization, Hao, *et al.* [173] carried out a field experiment to understand its impact on soil acidification on a silty clay loam soil in China, adopting a wheat-maize crop rotation system. A pH decrease due to the application of nitrogen fertilizer can be due essentially to three factors, i.e., nitrate leaching, plant uptake of cations and the leaching of bicarbonate ions. The authors derived the contribution on soil pH of each of these three factors, finding out that the greater plant nutrients uptake, due to the increase in soil fertility, is the main factor that leads to pH decrease, given their displacement of H<sup>+</sup> action for maintaining the charge balance [19]. Furthermore, the high clay fraction of the soil under study resulted in a low leaching of nitrogen products (e.g., NO<sub>3</sub><sup>-</sup>), causing consequent high N losses in the air due to a great denitrification rate. Despite this acidification may be beneficial for olivine EW, nitrogen fertilizer application

may lead to the presence of nitric acid (i.e.,  $\text{HNO}_3$ ) in soil water that, reacting with carbonate rocks (e.g., calcite), which in this case represent the nature of bedrock in Sicily and Padan plain, releases  $\text{CO}_2$  to the atmosphere [15], thus reducing carbon sequestration potential. Another relevant aspect to characterize in planning an EW intervention regards its commercial feasibility. In this purpose, carbon sequestration potentials have to be compared with costs, in order to find the better compromise between these factors such that the country adopting this strategy may afford it without a great economic effort. Beerling, *et al.* [116], after quantifying the CDR potential for several countries of the world, set up a cost analysis for each nation, to see if the countries with the highest carbon sequestration potential also present the lowest costs. The authors found an average global cost of about 100 USD per ton of sequestered  $\text{CO}_2$ , with the highest values obtained for United States, Canada, China, Poland and Spain, especially for great fraction of involved cropland area. These costs are however similar to other CDR techniques, such as direct air capture and biochar, leading to consider EW as a reasonable intervention to mitigate climate change. The main differences in costs depend on many factors, such as the cost of electricity for mineral grinding, transport and spreading operations. This evaluation has been carried out by means of a spatial analysis considering various cost sources, such as mining, processing, distribution, transport and spreading of the silicate mineral (basalt rock) in croplands. The spatial analysis consisted of creating a map of global transports, identifying the most convenient path,

once locating the sites where silicate minerals are abundant [162]. Then, different grinding strategies have been considered, in order to reduce the energy consumption and the corresponding CO<sub>2</sub> emissions and, at the same time, having basalt rock particles small enough to result in a high weathering rate.

An in-depth cost analysis is therefore necessary with the aim to identify those countries providing simultaneously the highest carbon sequestration potential minimizing the related costs. At this moment the EW model is subject of further enhancement aimed to apply the EW model at the global scale, deriving a global spatial distribution of CO<sub>2</sub> sequestration and costs and providing a tool to decision makers for an actual future application of the EW strategy.

## Appendix A – List of abbreviations

s	Soil moisture	
$S_{fc}$	Soil moisture at field capacity	
$W_r$	Weathering rate	$\text{mol m}^{-2} \text{s}^{-1}$
pH	Soil pH	
$k_{sil}$	Dissolution rate constant of forsterite	$\text{mol m}^{-2} \text{s}^{-1}$
$\Theta$	Ion activity product	
$k_{eq}$	Olivine dissolution constant	
$\phi$	Effective diameter of olivine particles	$\mu\text{m}$
$V_M$	Molar volume of olivine	$\text{cm}^3 \text{mol}^{-1}$

---

C	Organic carbon concentration	$\text{gC m}^{-3}$
ADD	Average added litter	$\text{gC m}^{-2} \text{d}^{-1}$
r	Fraction of decomposed carbon to respiration	
DEC	Decomposed organic carbon	$\text{gC m}^{-2} \text{d}^{-1}$
$k_{\text{DEC}}$	Carbon decomposition constant	$\text{m}^3 \text{d}^{-1} \text{gC}^{-1}$
$C_b$	Carbon concentration in the biomass pool	$\text{gC m}^{-3}$
D	$\text{CO}_2$ diffusivity in the soil	$\text{m}^2 \text{s}^{-1}$
$D_0$	Free-air diffusion coefficient of	$\text{m}^2 \text{s}^{-1}$

---

$Z_r$	Soil depth	m
n	Soil porosity	
$CO_{2, atm}$	Atmospheric $CO_2$ concentration	ppm
$k_1$	First dissociation constant of carbonic acid	
$k_2$	Second dissociation constant of carbonic acid	
$k_w$	Self-ionization constant of water	
PI	Input of $H^+$ from plants	$mol_H^+ l^{-1}$
RI	Input of $H^+$ from rainfall	$mol_H^+ l^{-1}$
$W_{bg}$	Background weathering term	$mol_H^+$

$W_{\text{oliv}}$	Olivine weathering term	$\text{mol}_H^+$
$x_{M_{OM}}^{m+}$	Mass of adsorbed of a generic ion on organic colloids	$\text{mol}_M^+$
$x_{M_{\text{clay}}}^{m+}$	Mass of adsorbed of a generic ion on clay colloids	$\text{mol}_M^+$
$UP_M$	Plant uptake of a generic ion	$\text{mol}_M^+ \text{ l}^{-1}$
$k_{\text{bg}}$	Specific dissolution rate of background minerals	$\text{mol m}^{-2} \text{ s}^{-1}$

---

$d_{bg}$	Diameter of background minerals particles	$\mu\text{m}$
$f_{bg}$	Mass fraction of background minerals	
$\rho_b$	Soil bulk density	$\text{kg m}^{-3}$
$\rho_{bg}$	Density of background minerals	$\text{g cm}^{-3}$
$V_{bg}$	Volume of a particle of background minerals	$\text{cm}^3$
$M_{oliv}$	Mass of added olivine	$\text{g m}^{-2}$
$\rho_{oliv}$	Density of olivine	$\text{g cm}^{-3}$
$V_{oliv}$	Volume of a particle of olivine	$\text{cm}^3$

---

$CEC_{OM}$	Organic component of the soil cation exchange capacity	mol
$CEC_{clay}$	Clay component of the soil cation exchange capacity	mol
$SC_{OM}(X-M)$	Selectivity constant for a generic exchange on organic colloids	
$SC_{clay}(X-M)$	Selectivity constant for a generic exchange on clay colloids	
$C_{DIC}$	Total dissolved inorganic carbon	mol l <sup>-1</sup>

---

$C_t$	Total carbon	$\text{mol l}^{-1}$
$K_{H, \text{ad}}$	Adimensional Henry's constant	
A	Alkalinity	$\text{mol l}^{-1}$
$A_t$	Total alkalinity	$\text{mol l}^{-1}$
$H_t^+$	Moles of total $H^+$	mol
$Ca_t^{2+}$	Moles of total $Ca^{2+}$	mol
$Mg_t^{2+}$	Moles of total $Mg^{2+}$	mol
$Na_t^+$	Moles of total $Na^+$	mol
$K_t^+$	Moles of total $K^+$	mol
$Al_t^{3+}$	Moles of total $Al^{3+}$	mol



## References

1. Ghil, M. Natural climate variability. In *Encyclopedia of Global Environmental Change*, MacCracken, M., Perry, J., Eds. Wiley & Sons, Chichester/New York: 2002; Vol. 1, pp. 544–549.
2. Jia, G.; E. Shevliakova; P. Artaxo; N. De Noblet-Ducoudré; R. Houghton; J. House; K. Kitajima; C. Lennard; A. Popp; A. Sirin, et al. *Land–climate interactions*. In: *Climate Change and Land: an IPCC special report on climate change, desertification, land degradation, sustainable land management, food security, and greenhouse gas fluxes in terrestrial ecosystems* [P.R. Shukla, J. Skea, E. Calvo Buendia, V. Masson-Delmotte, H.-O. Pörtner, D.C. Roberts, P. Zhai, R. Slade, S. Connors, R. van Diemen, M. Ferrat, E. Haughey, S. Luz, S. Neogi, M. Pathak, J. Petzold, J. Portugal Pereira, P. Vyas, E. Huntley, K. Kissick, M. Belkacemi, J. Malley, (eds.)]. In press.; 2019.
3. Tang, Q. Global change hydrology: Terrestrial water cycle and global change. *Science China Earth Sciences* **2020**, *63*, 459-462, doi:10.1007/s11430-019-9559-9.
4. Allen, M.R.; O.P. Dube; W. Solecki; F. Aragón-Durand; W. Cramer; S. Humphreys; M. Kainuma; J. Kala; N. Mahowald; Y. Mulugetta, et al. *Framing and Context*. In: *Global Warming of 1.5°C. An IPCC Special Report on the impacts of global warming of 1.5°C above pre-industrial*

- levels and related global greenhouse gas emission pathways, in the context of strengthening the global response to the threat of climate change, sustainable development, and efforts to eradicate poverty [Masson-Delmotte, V., P. Zhai, H.-O. Pörtner, D. Roberts, J. Skea, P.R. Shukla, A. Pirani, W. Moufouma-Okia, C. Péan, R. Pidcock, S. Connors, J.B.R. Matthews, Y. Chen, X. Zhou, M.I. Gomis, E. Lonnoy, T. Maycock, M. Tignor, and T. Waterfield (eds.)]. In Press.; 2018.*
5. Shepherd, A.; Ivins, E.; Rignot, E.; Smith, B.; van den Broeke, M.; Velicogna, I.; Whitehouse, P.; Briggs, K.; Joughin, I.; Krinner, G., et al. Mass balance of the Antarctic Ice Sheet from 1992 to 2017. *Nature* **2018**, *558*, 219-222, doi:10.1038/s41586-018-0179-y.
  6. Rogelj, J.; Fricko, O.; Meinshausen, M.; Krey, V.; Zilliacus, J.J.J.; Riahi, K. Understanding the origin of Paris Agreement emission uncertainties. *Nature Communications* **2017**, *8*, 15748, doi:10.1038/ncomms15748.
  7. Solomon, S.; Plattner, G.-K.; Knutti, R.; Friedlingstein, P. Irreversible climate change due to carbon dioxide emissions. *Proceedings of the National Academy of Sciences* **2009**, *106*, 1704-1709, doi:10.1073/pnas.0812721106.
  8. Joshi, M.; Hawkins, E.; Sutton, R.; Lowe, J.; Frame, D. Projections of when temperature change will exceed 2 °C above pre-industrial

- levels. *Nature Climate Change* **2011**, *1*, 407-412, doi:10.1038/nclimate1261.
9. Seidel, D.J.; Feingold, G.; Jacobson, A.R.; Loeb, N. Detection limits of albedo changes induced by climate engineering. *Nature Climate Change* **2014**, *4*, 93-98, doi:10.1038/nclimate2076.
  10. Sun, W.; Wang, B.; Chen, D.; Gao, C.; Lu, G.; Liu, J. Global monsoon response to tropical and Arctic stratospheric aerosol injection. *Climate Dynamics* **2020**, *55*, 2107-2121, doi:10.1007/s00382-020-05371-7.
  11. Stjern, C.W.; Muri, H.; Ahlm, L.; Boucher, O.; Cole, J.N.S.; Ji, D.; Jones, A.; Haywood, J.; Kravitz, B.; Lenton, A., et al. Response to marine cloud brightening in a multi-model ensemble. *Atmos. Chem. Phys.* **2018**, *18*, 621-634, doi:10.5194/acp-18-621-2018.
  12. Russell, L.M.; Rasch, P.J.; Mace, G.M.; Jackson, R.B.; Shepherd, J.; Liss, P.; Leinen, M.; Schimel, D.; Vaughan, N.E.; Janetos, A.C., et al. Ecosystem Impacts of Geoengineering: A Review for Developing a Science Plan. *AMBIO* **2012**, *41*, 350-369, doi:10.1007/s13280-012-0258-5.
  13. Hou, G.; Delang, C.O.; Lu, X.; Gao, L. Grouping tree species to estimate afforestation-driven soil organic carbon sequestration. *Plant and Soil* **2020**, *455*, 507-518, doi:10.1007/s11104-020-04685-z.
  14. Deutz, S.; Bardow, A. Life-cycle assessment of an industrial direct air capture process based on temperature–vacuum swing adsorption. *Nature*

- Energy* **2021**, *6*, 203-213, doi:10.1038/s41560-020-00771-9.
15. Hartmann, J.; West, A.J.; Renforth, P.; Köhler, P.; De La Rocha, C.L.; Wolf-Gladrow, D.A.; Dürr, H.H.; Scheffran, J. Enhanced chemical weathering as a geoengineering strategy to reduce atmospheric carbon dioxide, supply nutrients, and mitigate ocean acidification. *Reviews of Geophysics* **2013**, *51*, 113-149, doi:<https://doi.org/10.1002/rog.20004>.
16. Gomez-Casanovas, N.; Blanc-Betes, E.; Moore, C.E.; Bernacchi, C.J.; Kantola, I.; DeLucia, E.H. A review of transformative strategies for climate mitigation by grasslands. *Science of The Total Environment* **2021**, *799*, 149466, doi:<https://doi.org/10.1016/j.scitotenv.2021.149466>.
17. Ramos, C.G.; Hower, J.C.; Blanco, E.; Oliveira, M.L.S.; Theodoro, S.H. Possibilities of using silicate rock powder: An overview. *Geoscience Frontiers* **2021**, doi:<https://doi.org/10.1016/j.gsf.2021.101185>, 101185, doi:<https://doi.org/10.1016/j.gsf.2021.101185>.
18. Lal, R.; Monger, C.; Nave, L.; Smith, P. The role of soil in regulation of climate. *Philosophical Transactions of the Royal Society B: Biological Sciences* **2021**, *376*, 20210084, doi:[doi:10.1098/rstb.2021.0084](https://doi.org/10.1098/rstb.2021.0084).

19. Weil, R.; Brady, N. *The Nature and Properties of Soils. 15th edition*; 2017.
20. Asibor, J.O.; Clough, P.T.; Nabavi, S.A.; Manovic, V. Assessment of optimal conditions for the performance of greenhouse gas removal methods. *Journal of Environmental Management* **2021**, *294*, 113039, doi:<https://doi.org/10.1016/j.jenvman.2021.113039>.
21. White, A.F.; Brantley, S.L. The effect of time on the weathering of silicate minerals: why do weathering rates differ in the laboratory and field? *Chemical Geology* **2003**, *202*, 479-506, doi:<https://doi.org/10.1016/j.chemgeo.2003.03.001>.
22. Hellmann, R.; Tisserand, D. Dissolution kinetics as a function of the Gibbs free energy of reaction: An experimental study based on albite feldspar. *Geochimica et Cosmochimica Acta* **2006**, *70*, 364-383, doi:<https://doi.org/10.1016/j.gca.2005.10.007>.
23. Köhler, S.J.; Dufaud, F.; Oelkers, E.H. An experimental study of illite dissolution kinetics as a function of pH from 1.4 to 12.4 and temperature from 5 to 50°C. *Geochimica et Cosmochimica Acta* **2003**, *67*, 3583-3594, doi:[https://doi.org/10.1016/S0016-7037\(03\)00163-7](https://doi.org/10.1016/S0016-7037(03)00163-7).
24. Amann, T.; Hartmann, J.; Struyf, E.; de Oliveira Garcia, W.; Fischer, E.K.; Janssens, I.; Meire, P.;

- Schoelynck, J. Enhanced Weathering and related element fluxes – a cropland mesocosm approach. *Biogeosciences* **2020**, *17*, 103-119, doi:10.5194/bg-17-103-2020.
25. Renforth, P.; Pogge von Strandmann, P.A.E.; Henderson, G.M. The dissolution of olivine added to soil: Implications for enhanced weathering. *Applied Geochemistry* **2015**, *61*, 109-118, doi:<https://doi.org/10.1016/j.apgeochem.2015.05.016>.
26. ten Berge, H.F.M.; van der Meer, H.G.; Steenhuizen, J.W.; Goedhart, P.W.; Knops, P.; Verhagen, J. Olivine weathering in soil, and its effects on growth and nutrient uptake in Ryegrass (*Lolium perenne* L.): a pot experiment. *PLoS One* **2012**, *7*, e42098-e42098, doi:10.1371/journal.pone.0042098.
27. Kelland, M.E.; Wade, P.W.; Lewis, A.L.; Taylor, L.L.; Sarkar, B.; Andrews, M.G.; Lomas, M.R.; Cotton, T.E.A.; Kemp, S.J.; James, R.H., et al. Increased yield and CO<sub>2</sub> sequestration potential with the C<sub>4</sub> cereal *Sorghum bicolor* cultivated in basaltic rock dust-amended agricultural soil. *Global Change Biology* **2020**, *26*, 3658-3676, doi:<https://doi.org/10.1111/gcb.15089>.
28. Dietzen, C.; Harrison, R.; Michelsen-Correa, S. Effectiveness of enhanced mineral weathering as a carbon sequestration tool and alternative to agricultural lime: An incubation experiment. *International Journal of Greenhouse Gas Control*

- 2018, 74, 251-258,  
doi:<https://doi.org/10.1016/j.ijggc.2018.05.007>.
29. Vicca, S.; Goll, D.S.; Hagens, M.; Hartmann, J.; Janssens, I.A.; Neubeck, A.; Peñuelas, J.; Poblador, S.; Rijnders, J.; Sardans, J., et al. Is the climate change mitigation effect of enhanced silicate weathering governed by biological processes? *Global Change Biology* n/a, doi:<https://doi.org/10.1111/gcb.15993>.
30. Taylor, L.L.; Beerling, D.J.; Quegan, S.; Banwart, S.A. Simulating carbon capture by enhanced weathering with croplands: an overview of key processes highlighting areas of future model development. *Biology Letters* **2017**, *13*, 20160868, doi:[doi:10.1098/rsbl.2016.0868](https://doi.org/10.1098/rsbl.2016.0868).
31. Cipolla, G.; Calabrese, S.; Noto, L.V.; Porporato, A. The role of hydrology on enhanced weathering for carbon sequestration I. Modeling rock-dissolution reactions coupled to plant, soil moisture, and carbon dynamics. *Advances in Water Resources* **2021**, <https://doi.org/10.1016/j.advwatres.2021.103934>, 103934, doi:<https://doi.org/10.1016/j.advwatres.2021.103934>.
32. Cipolla, G.; Calabrese, S.; Noto, L.V.; Porporato, A. The role of hydrology on enhanced weathering for carbon sequestration II. From hydroclimatic scenarios to carbon-sequestration efficiencies. *Advances in Water Resources* **2021**,

- <https://doi.org/10.1016/j.advwatres.2021.103949>,  
103949,  
[doi:https://doi.org/10.1016/j.advwatres.2021.103949](https://doi.org/10.1016/j.advwatres.2021.103949).
33. Martel, J.-L.; Mailhot, A.; Brissette, F.; Caya, D. Role of Natural Climate Variability in the Detection of Anthropogenic Climate Change Signal for Mean and Extreme Precipitation at Local and Regional Scales. *Journal of Climate* **2018**, *31*, 4241-4263, doi:10.1175/jcli-d-17-0282.1.
34. Hulme, M.; Barrow, E.M.; Arnell, N.W.; Harrison, P.A.; Johns, T.C.; Downing, T.E. Relative impacts of human-induced climate change and natural climate variability. *Nature* **1999**, *397*, 688-691, doi:10.1038/17789.
35. Stephens, G.L.; Li, J.; Wild, M.; Clayson, C.A.; Loeb, N.; Kato, S.; L'Ecuyer, T.; Stackhouse, P.W.; Lebsock, M.; Andrews, T. An update on Earth's energy balance in light of the latest global observations. *Nature Geoscience* **2012**, *5*, 691-696, doi:10.1038/ngeo1580.
36. Murphy, D.M.; Solomon, S.; Portmann, R.W.; Rosenlof, K.H.; Forster, P.M.; Wong, T. An observationally based energy balance for the Earth since 1950. *Journal of Geophysical Research: Atmospheres* **2009**, *114*, doi:https://doi.org/10.1029/2009JD012105.
37. Lashof, D.A.; Ahuja, D.R. Relative contributions of greenhouse gas emissions to global warming.

- Nature* **1990**, 344, 529-531, doi:10.1038/344529a0.
38. Rocklöv, J.; Dubrow, R. Climate change: an enduring challenge for vector-borne disease prevention and control. *Nature Immunology* **2020**, *21*, 479-483, doi:10.1038/s41590-020-0648-y.
39. Allen, M.; Mustafa Babiker; Yang Chen; Heleen de Coninck; Sarah Connors; Renée van Diemen; Opha Pauline Dube; Kristie L. Ebi; Francois Engelbrecht; Marion Ferrat, et al. *IPCC, 2018: Summary for Policymakers. In: Global Warming of 1.5°C. An IPCC Special Report on the impacts of global warming of 1.5°C above pre-industrial levels and related global greenhouse gas emission pathways, in the context of strengthening the global response to the threat of climate change, sustainable development, and efforts to eradicate poverty [Masson-Delmotte, V., P. Zhai, H.-O. Pörtner, D. Roberts, J. Skea, P.R. Shukla, A. Pirani, W. Moufouma-Okia, C. Péan, R. Pidcock, S. Connors, J.B.R. Matthews, Y. Chen, X. Zhou, M.I. Gomis, E. Lonnoy, T. Maycock, M. Tignor, and T. Waterfield (eds.)]. In Press.; 2018.*
40. Huang, J.; Zhang, G.; Zhang, Y.; Guan, X.; Wei, Y.; Guo, R. Global desertification vulnerability to climate change and human activities. *Land Degradation & Development* **2020**, *31*, 1380-1391, doi:https://doi.org/10.1002/ldr.3556.

41. Burrell, A.L.; Evans, J.P.; De Kauwe, M.G. Anthropogenic climate change has driven over 5 million km<sup>2</sup> of drylands towards desertification. *Nature Communications* **2020**, *11*, 3853, doi:10.1038/s41467-020-17710-7.
42. Samaniego, L.; Thober, S.; Kumar, R.; Wanders, N.; Rakovec, O.; Pan, M.; Zink, M.; Sheffield, J.; Wood, E.F.; Marx, A. Anthropogenic warming exacerbates European soil moisture droughts. *Nature Climate Change* **2018**, *8*, 421-426, doi:10.1038/s41558-018-0138-5.
43. Huang, J.; Yu, H.; Guan, X.; Wang, G.; Guo, R. Accelerated dryland expansion under climate change. *Nature Climate Change* **2016**, *6*, 166-171, doi:10.1038/nclimate2837.
44. D'Odorico, P.; Bhattachan, A.; Davis, K.F.; Ravi, S.; Runyan, C.W. Global desertification: Drivers and feedbacks. *Advances in Water Resources* **2013**, *51*, 326-344, doi:<https://doi.org/10.1016/j.advwatres.2012.01.013>.
45. Reynolds, J.F.; Smith, D.M.S.; Lambin, E.F.; Turner, B.L.; Mortimore, M.; Batterbury, S.P.J.; Downing, T.E.; Dowlatabadi, H.; Fernández, R.J.; Herrick, J.E., et al. Global Desertification: Building a Science for Dryland Development. *Science* **2007**, *316*, 847-851, doi:10.1126/science.1131634.
46. Shugar, D.H.; Burr, A.; Haritashya, U.K.; Kargel, J.S.; Watson, C.S.; Kennedy, M.C.; Bevington,

- A.R.; Betts, R.A.; Harrison, S.; Strattman, K. Rapid worldwide growth of glacial lakes since 1990. *Nature Climate Change* **2020**, *10*, 939-945, doi:10.1038/s41558-020-0855-4.
47. Ouyang, Z.; Qi, D.; Chen, L.; Takahashi, T.; Zhong, W.; DeGrandpre, M.D.; Chen, B.; Gao, Z.; Nishino, S.; Murata, A., et al. Sea-ice loss amplifies summertime decadal CO<sub>2</sub> increase in the western Arctic Ocean. *Nature Climate Change* **2020**, *10*, 678-684, doi:10.1038/s41558-020-0784-2.
48. Leeson, A.A.; Shepherd, A.; Briggs, K.; Howat, I.; Fettweis, X.; Morlighem, M.; Rignot, E. Supraglacial lakes on the Greenland ice sheet advance inland under warming climate. *Nature Climate Change* **2015**, *5*, 51-55, doi:10.1038/nclimate2463.
49. Landrum, L.; Holland, M.M. Extremes become routine in an emerging new Arctic. *Nature Climate Change* **2020**, *10*, 1108-1115, doi:10.1038/s41558-020-0892-z.
50. Befus, K.M.; Barnard, P.L.; Hoover, D.J.; Finzi Hart, J.A.; Voss, C.I. Increasing threat of coastal groundwater hazards from sea-level rise in California. *Nature Climate Change* **2020**, *10*, 946-952, doi:10.1038/s41558-020-0874-1.
51. Tabari, H. Extreme value analysis dilemma for climate change impact assessment on global flood and extreme precipitation. *Journal of Hydrology* **2021**, *593*, 125932,

- doi:<https://doi.org/10.1016/j.jhydrol.2020.125932>
- .
52. Tabari, H. Climate change impact on flood and extreme precipitation increases with water availability. *Scientific Reports* **2020**, *10*, 13768, doi:10.1038/s41598-020-70816-2.
53. Shadmehri Toosi, A.; Doulabian, S.; Ghasemi Tousi, E.; Calbimonte, G.H.; Alaghmand, S. Large-scale flood hazard assessment under climate change: A case study. *Ecological Engineering* **2020**, *147*, 105765, doi:<https://doi.org/10.1016/j.ecoleng.2020.105765>
54. Hettiarachchi, S.; Wasko, C.; Sharma, A. Increase in flood risk resulting from climate change in a developed urban watershed – the role of storm temporal patterns. *Hydrol. Earth Syst. Sci.* **2018**, *22*, 2041-2056, doi:10.5194/hess-22-2041-2018.
55. Blenkinsop, S.; Fowler, H.J.; Barbero, R.; Chan, S.C.; Guerreiro, S.B.; Kendon, E.; Lenderink, G.; Lewis, E.; Li, X.F.; Westra, S., et al. The INTENSE project: using observations and models to understand the past, present and future of sub-daily rainfall extremes. *Adv. Sci. Res.* **2018**, *15*, 117-126, doi:10.5194/asr-15-117-2018.
56. Swain, D.L.; Wing, O.E.J.; Bates, P.D.; Done, J.M.; Johnson, K.A.; Cameron, D.R. Increased Flood Exposure Due to Climate Change and Population Growth in the United States. *Earth's*

- Future* **2020**, 8, e2020EF001778, doi:<https://doi.org/10.1029/2020EF001778>.
57. Borchers Arriagada, N.; Bowman, D.M.J.S.; Palmer, A.J.; Johnston, F.H. Climate Change, Wildfires, Heatwaves and Health Impacts in Australia. In *Extreme Weather Events and Human Health: International Case Studies*, Akhtar, R., Ed. Springer International Publishing: Cham, 2020; 10.1007/978-3-030-23773-8\_8pp. 99-116.
58. Abatzoglou, J.T.; Williams, A.P. Impact of anthropogenic climate change on wildfire across western US forests. *Proceedings of the National Academy of Sciences* **2016**, *113*, 11770-11775, doi:[10.1073/pnas.1607171113](https://doi.org/10.1073/pnas.1607171113).
59. Stambaugh, M.C.; Guyette, R.P.; Stroh, E.D.; Struckhoff, M.A.; Whittier, J.B. Future southcentral US wildfire probability due to climate change. *Climatic Change* **2018**, *147*, 617-631, doi:[10.1007/s10584-018-2156-8](https://doi.org/10.1007/s10584-018-2156-8).
60. Goss, M.; Swain, D.L.; Abatzoglou, J.T.; Sarhadi, A.; Kolden, C.A.; Williams, A.P.; Diffenbaugh, N.S. Climate change is increasing the likelihood of extreme autumn wildfire conditions across California. *Environmental Research Letters* **2020**, *15*, 094016, doi:[10.1088/1748-9326/ab83a7](https://doi.org/10.1088/1748-9326/ab83a7).
61. Loehman, R.A. Drivers of wildfire carbon emissions. *Nature Climate Change* **2020**, *10*, 1070-1071, doi:[10.1038/s41558-020-00922-6](https://doi.org/10.1038/s41558-020-00922-6).
62. Ortiz-Bobea, A.; Ault, T.R.; Carrillo, C.M.; Chambers, R.G.; Lobell, D.B. Anthropogenic

- climate change has slowed global agricultural productivity growth. *Nature Climate Change* **2021**, *11*, 306-312, doi:10.1038/s41558-021-01000-1.
63. Janssens, C.; Havlík, P.; Krisztin, T.; Baker, J.; Frank, S.; Hasegawa, T.; Leclère, D.; Ohrel, S.; Ragnauth, S.; Schmid, E., et al. Global hunger and climate change adaptation through international trade. *Nature Climate Change* **2020**, *10*, 829-835, doi:10.1038/s41558-020-0847-4.
64. Connolly-Boutin, L.; Smit, B. Climate change, food security, and livelihoods in sub-Saharan Africa. *Regional Environmental Change* **2016**, *16*, 385-399, doi:10.1007/s10113-015-0761-x.
65. Leisner, C.P. Review: Climate change impacts on food security- focus on perennial cropping systems and nutritional value. *Plant Science* **2020**, *293*, 110412, doi:https://doi.org/10.1016/j.plantsci.2020.110412.
66. Molotoks, A.; Smith, P.; Dawson, T.P. Impacts of land use, population, and climate change on global food security. *Food and Energy Security* **2021**, *10*, e261, doi:https://doi.org/10.1002/fes3.261.
67. Wood, A.L.; Ansah, P.; Rivers, L.; Ligmann-Zielinska, A. Examining climate change and food security in Ghana through an intersectional framework. *The Journal of Peasant Studies* **2021**, *48*, 329-348, doi:10.1080/03066150.2019.1655639.

68. Nicholls, R.J.; Cazenave, A. Sea-Level Rise and Its Impact on Coastal Zones. *Science* **2010**, *328*, 1517-1520, doi:10.1126/science.1185782.
69. Spencer, T.; Schuerch, M.; Nicholls, R.J.; Hinkel, J.; Lincke, D.; Vafeidis, A.T.; Reef, R.; McFadden, L.; Brown, S. Global coastal wetland change under sea-level rise and related stresses: The DIVA Wetland Change Model. *Global and Planetary Change* **2016**, *139*, 15-30, doi:<https://doi.org/10.1016/j.gloplacha.2015.12.018>.
70. Moon, T.A.; Overeem, I.; Druckenmiller, M.; Holland, M.; Huntington, H.; Kling, G.; Lovecraft, A.L.; Miller, G.; Scambos, T.; Schädel, C., et al. The Expanding Footprint of Rapid Arctic Change. *Earth's Future* **2019**, *7*, 212-218, doi:<https://doi.org/10.1029/2018EF001088>.
71. Fretwell, P.; Pritchard, H.D.; Vaughan, D.G.; Bamber, J.L.; Barrand, N.E.; Bell, R.; Bianchi, C.; Bingham, R.G.; Blankenship, D.D.; Casassa, G., et al. Bedmap2: improved ice bed, surface and thickness datasets for Antarctica. *The Cryosphere* **2013**, *7*, 375-393, doi:10.5194/tc-7-375-2013.
72. Hegerl, G.C.; Black, E.; Allan, R.P.; Ingram, W.J.; Polson, D.; Trenberth, K.E.; Chadwick, R.S.; Arkin, P.A.; Sarojini, B.B.; Becker, A., et al. Challenges in Quantifying Changes in the Global Water Cycle. *Bulletin of the American Meteorological Society* **2015**, *96*, 1097-1115, doi:10.1175/bams-d-13-00212.1.

73. Aronica, G.T.; Brigandí, G.; Morey, N. Flash floods and debris flow in the city area of Messina, north-east part of Sicily, Italy in October 2009: the case of the Giampilieri catchment. *Nat. Hazards Earth Syst. Sci.* **2012**, *12*, 1295-1309, doi:10.5194/nhess-12-1295-2012.
74. Neal, R.; Fereday, D.; Crocker, R.; Comer, R.E. A flexible approach to defining weather patterns and their application in weather forecasting over Europe. *Meteorological Applications* **2016**, *23*, 389-400, doi:https://doi.org/10.1002/met.1563.
75. Cipolla, G.; Francipane, A.; Noto, L.V. Classification of Extreme Rainfall for a Mediterranean Region by Means of Atmospheric Circulation Patterns and Reanalysis Data. *Water Resources Management* **2020**, *34*, 3219-3235, doi:10.1007/s11269-020-02609-1.
76. Treppiedi, D.; Cipolla, G.; Francipane, A.; Noto, L.V. Detecting precipitation trend using a multiscale approach based on quantile regression over a Mediterranean area. *International Journal of Climatology* *n/a*, doi:https://doi.org/10.1002/joc.7161.
77. Arnone, E.; Pumo, D.; Viola, F.; Noto, L.V.; La Loggia, G. Rainfall statistics changes in Sicily. *Hydrol. Earth Syst. Sci.* **2013**, *17*, 2449-2458, doi:10.5194/hess-17-2449-2013.
78. Bowman, D.M.J.S.; Balch, J.; Artaxo, P.; Bond, W.J.; Cochrane, M.A.; D'Antonio, C.M.; DeFries, R.; Johnston, F.H.; Keeley, J.E.; Krawchuk, M.A.,

- et al. The human dimension of fire regimes on Earth. *Journal of Biogeography* **2011**, *38*, 2223-2236, doi:<https://doi.org/10.1111/j.1365-2699.2011.02595.x>.
79. Sun, Q.; Miao, C.; Hanel, M.; Borthwick, A.G.L.; Duan, Q.; Ji, D.; Li, H. Global heat stress on health, wildfires, and agricultural crops under different levels of climate warming. *Environment International* **2019**, *128*, 125-136, doi:<https://doi.org/10.1016/j.envint.2019.04.025>.
80. Le Quéré, C.; Jackson, R.B.; Jones, M.W.; Smith, A.J.P.; Abernethy, S.; Andrew, R.M.; De-Gol, A.J.; Willis, D.R.; Shan, Y.; Canadell, J.G., et al. Temporary reduction in daily global CO<sub>2</sub> emissions during the COVID-19 forced confinement. *Nature Climate Change* **2020**, *10*, 647-653, doi:[10.1038/s41558-020-0797-x](https://doi.org/10.1038/s41558-020-0797-x).
81. Le Quéré, C.; Peters, G.P.; Friedlingstein, P.; Andrew, R.M.; Canadell, J.G.; Davis, S.J.; Jackson, R.B.; Jones, M.W. Fossil CO<sub>2</sub> emissions in the post-COVID-19 era. *Nature Climate Change* **2021**, *11*, 197-199, doi:[10.1038/s41558-021-01001-0](https://doi.org/10.1038/s41558-021-01001-0).
82. Forster, P.M.; Forster, H.I.; Evans, M.J.; Gidden, M.J.; Jones, C.D.; Keller, C.A.; Lamboll, R.D.; Quéré, C.L.; Rogelj, J.; Rosen, D., et al. Current and future global climate impacts resulting from COVID-19. *Nature Climate Change* **2020**, *10*, 913-919, doi:[10.1038/s41558-020-0883-0](https://doi.org/10.1038/s41558-020-0883-0).

83. Liu, Z.; Ciais, P.; Deng, Z.; Lei, R.; Davis, S.J.; Feng, S.; Zheng, B.; Cui, D.; Dou, X.; Zhu, B., et al. Near-real-time monitoring of global CO<sub>2</sub> emissions reveals the effects of the COVID-19 pandemic. *Nature Communications* **2020**, *11*, 5172, doi:10.1038/s41467-020-18922-7.
84. Wright, M.J.; Teagle, D.A.H.; Feetham, P.M. A quantitative evaluation of the public response to climate engineering. *Nature Climate Change* **2014**, *4*, 106-110, doi:10.1038/nclimate2087.
85. Griscom, B.W.; Adams, J.; Ellis, P.W.; Houghton, R.A.; Lomax, G.; Miteva, D.A.; Schlesinger, W.H.; Shoch, D.; Siikamäki, J.V.; Smith, P., et al. Natural climate solutions. *Proceedings of the National Academy of Sciences* **2017**, *114*, 11645-11650, doi:10.1073/pnas.1710465114.
86. Crook, J.A.; Jackson, L.S.; Forster, P.M. Can increasing albedo of existing ship wakes reduce climate change? *Journal of Geophysical Research: Atmospheres* **2016**, *121*, 1549-1558, doi:https://doi.org/10.1002/2015JD024201.
87. Jandaghian, Z.; Akbari, H. The Effect of Increasing Surface Albedo on Urban Climate and Air Quality: A Detailed Study for Sacramento, Houston, and Chicago. *Climate* **2018**, *6*, 19.
88. Tjiputra, J.F.; Grini, A.; Lee, H. Impact of idealized future stratospheric aerosol injection on the large-scale ocean and land carbon cycles. *Journal of Geophysical Research: Biogeosciences*

- 2016, 121, 2-27,  
doi:<https://doi.org/10.1002/2015JG003045>.
89. Smith, W. The cost of stratospheric aerosol injection through 2100. *Environmental Research Letters* **2020**, 15, 114004, doi:10.1088/1748-9326/aba7e7.
90. Smith, W.; Wagner, G. Stratospheric aerosol injection tactics and costs in the first 15 years of deployment. *Environmental Research Letters* **2018**, 13, 124001, doi:10.1088/1748-9326/aae98d.
91. Zhao, M.; Cao, L.; Duan, L.; Bala, G.; Caldeira, K. Climate More Responsive to Marine Cloud Brightening Than Ocean Albedo Modification: A Model Study. *Journal of Geophysical Research: Atmospheres* **2021**, 126, e2020JD033256, doi:<https://doi.org/10.1029/2020JD033256>.
92. Doney, S.C.; Fabry, V.J.; Feely, R.A.; Kleypas, J.A. Ocean Acidification: The Other CO<sub>2</sub> Problem. *Annual Review of Marine Science* **2009**, 1, 169-192, doi:10.1146/annurev.marine.010908.163834.
93. Betz, G.; Brachatzek, N.; Cacean, S.; Güssow, K.; Heintzenberg, J.; Hiller, S.; Hoose, C.; Klepper, G.; Leisner, T.; Oschlies, A., et al. *Gezielte Eingriffe in das Klima? Eine Bestandsaufnahme der Debatte zu Climate Engineering*; Kiel Earth Institute: 2011.
94. Williams, C.A.; Gu, H.; Jiao, T. Climate impacts of U.S. forest loss span net warming to net

- cooling. *Science Advances* **2021**, *7*, eaax8859, doi:10.1126/sciadv.aax8859.
95. Duffy, C.; O'Donoghue, C.; Ryan, M.; Styles, D.; Spillane, C. Afforestation: Replacing livestock emissions with carbon sequestration. *Journal of Environmental Management* **2020**, *264*, 110523, doi:https://doi.org/10.1016/j.jenvman.2020.110523.
96. Fuhrman, J.; McJeon, H.; Patel, P.; Doney, S.C.; Shobe, W.M.; Clarens, A.F. Food–energy–water implications of negative emissions technologies in a +1.5 °C future. *Nature Climate Change* **2020**, *10*, 920-927, doi:10.1038/s41558-020-0876-z.
97. Chatterjee, S.; Huang, K.-W. Unrealistic energy and materials requirement for direct air capture in deep mitigation pathways. *Nature Communications* **2020**, *11*, 3287, doi:10.1038/s41467-020-17203-7.
98. Sverdrup, H.; Warfvinge, P. Weathering of primary silicate minerals in the natural soil environment in relation to a chemical weathering model. *Water, Air, and Soil Pollution* **1988**, *38*, 387-408, doi:10.1007/bf00280768.
99. Peltier, L.C. The Geographic Cycle in Periglacial Regions as it is Related to Climatic Geomorphology. *Annals of the Association of American Geographers* **1950**, *40*, 214-236, doi:10.1080/00045605009352070.
100. Lasaga, A.C. Chemical kinetics of water-rock interactions. *Journal of Geophysical Research*:

- Solid Earth* **1984**, 89, 4009-4025, doi:<https://doi.org/10.1029/JB089iB06p04009>.
101. Rimstidt, J.D. Diffusion control of quartz and forsterite dissolution rates. *Applied Geochemistry* **2015**, 61, 99-108, doi:<https://doi.org/10.1016/j.apgeochem.2015.05.020>.
102. Palandri, J.L.; Kharaka, Y.K. *A compilation of rate parameters of water-mineral interaction kinetics for application to geochemical modeling*; 2004; p 64.
103. Crundwell, F.K. The mechanism of dissolution of forsterite, olivine and minerals of the orthosilicate group. *Hydrometallurgy* **2014**, 150, 68-82, doi:<https://doi.org/10.1016/j.hydromet.2014.09.006>.
104. Giannakis, G.V.; Nikolaidis, N.P.; Valstar, J.; Rowe, E.C.; Moirogiorgou, K.; Kotronakis, M.; Paranychianakis, N.V.; Rousseva, S.; Stamati, F.E.; Banwart, S.A. Chapter Ten - Integrated Critical Zone Model (1D-ICZ): A Tool for Dynamic Simulation of Soil Functions and Soil Structure. In *Advances in Agronomy*, Banwart, S.A., Sparks, D.L., Eds. Academic Press: 2017; Vol. 142, pp. 277-314.
105. Kotronakis, M.; Giannakis, G.V.; Nikolaidis, N.P.; Rowe, E.C.; Valstar, J.; Paranychianakis, N.V.; Banwart, S.A. Chapter Eleven - Modeling the Impact of Carbon Amendments on Soil Ecosystem Functions Using the 1D-ICZ Model. In

- Advances in Agronomy*, Banwart, S.A., Sparks, D.L., Eds. Academic Press: 2017; Vol. 142, pp. 315-352.
106. Taylor, L.L.; Quirk, J.; Thorley, R.M.S.; Kharecha, P.A.; Hansen, J.; Ridgwell, A.; Lomas, M.R.; Banwart, S.A.; Beerling, D.J. Enhanced weathering strategies for stabilizing climate and averting ocean acidification. *Nature Climate Change* **2016**, *6*, 402-406, doi:10.1038/nclimate2882.
107. Godd ris, Y.; Fran ois, L.M.; Probst, A.; Schott, J.; Moncoulon, D.; Labat, D.; Viville, D. Modelling weathering processes at the catchment scale: The WITCH numerical model. *Geochimica et Cosmochimica Acta* **2006**, *70*, 1128-1147, doi:https://doi.org/10.1016/j.gca.2005.11.018.
108. Beaulieu, E.; Godd ris, Y.; Donnadieu, Y.; Labat, D.; Roelandt, C. High sensitivity of the continental-weathering carbon dioxide sink to future climate change. *Nature Climate Change* **2012**, *2*, 346-349, doi:10.1038/nclimate1419.
109. Roelandt, C.; Godd ris, Y.; Bonnet, M.-P.; Sondag, F. Coupled modeling of biospheric and chemical weathering processes at the continental scale. *Global Biogeochemical Cycles* **2010**, *24*, doi:https://doi.org/10.1029/2008GB003420.
110. Warfvinge, P.; Sverdrup, H. Calculating critical loads of acid deposition with PROFILE — A steady-state soil chemistry model. *Water, Air, and*

- Soil Pollution* **1992**, 63, 119-143, doi:10.1007/bf00475626.
111. Warfvinge, P.; Falkengren-Grerup, U.; Sverdrup, H.; Andersen, B. Modelling long-term cation supply in acidified forest stands. *Environmental Pollution* **1993**, 80, 209-221, doi:[https://doi.org/10.1016/0269-7491\(93\)90041-L](https://doi.org/10.1016/0269-7491(93)90041-L).
112. Cosby, B.J.; Ferrier, R.C.; Jenkins, A.; Wright, R.F. Modelling the effects of acid deposition: refinements, adjustments and inclusion of nitrogen dynamics in the MAGIC model. *Hydrol. Earth Syst. Sci.* **2001**, 5, 499-518, doi:10.5194/hess-5-499-2001.
113. Keating, B.A.; Carberry, P.S.; Hammer, G.L.; Probert, M.E.; Robertson, M.J.; Holzworth, D.; Huth, N.I.; Hargreaves, J.N.G.; Meinke, H.; Hochman, Z., et al. An overview of APSIM, a model designed for farming systems simulation. *European Journal of Agronomy* **2003**, 18, 267-288, doi:[https://doi.org/10.1016/S1161-0301\(02\)00108-9](https://doi.org/10.1016/S1161-0301(02)00108-9).
114. Hartman, M.D.; Baron, J.S.; Ojima, D.S. Application of a coupled ecosystem-chemical equilibrium model, DayCent-Chem, to stream and soil chemistry in a Rocky Mountain watershed. *Ecological Modelling* **2007**, 200, 493-510, doi:<https://doi.org/10.1016/j.ecolmodel.2006.09.001>.

115. Lewis, A.L.; Sarkar, B.; Wade, P.; Kemp, S.J.; Hodson, M.E.; Taylor, L.L.; Yeong, K.L.; Davies, K.; Nelson, P.N.; Bird, M.I., et al. Effects of mineralogy, chemistry and physical properties of basalts on carbon capture potential and plant-nutrient element release via enhanced weathering. *Applied Geochemistry* **2021**, *132*, 105023, doi:<https://doi.org/10.1016/j.apgeochem.2021.105023>.
116. Beerling, D.J.; Kantzas, E.P.; Lomas, M.R.; Wade, P.; Eufrazio, R.M.; Renforth, P.; Sarkar, B.; Andrews, M.G.; James, R.H.; Pearce, C.R., et al. Potential for large-scale CO<sub>2</sub> removal via enhanced rock weathering with croplands. *Nature* **2020**, *583*, 242-248, doi:10.1038/s41586-020-2448-9.
117. Soulaine, C.; Roman, S.; Kovscek, A.; Tchelepi, H.A. Mineral dissolution and wormholing from a pore-scale perspective. *Journal of Fluid Mechanics* **2017**, *827*, 457-483, doi:10.1017/jfm.2017.499.
118. Maher, K. The dependence of chemical weathering rates on fluid residence time. December 01, 2009; pp. EP52B-01.
119. Uroz, S.; Calvaruso, C.; Turpault, M.-P.; Frey-Klett, P. Mineral weathering by bacteria: ecology, actors and mechanisms. *Trends in Microbiology* **2009**, *17*, 378-387, doi:<https://doi.org/10.1016/j.tim.2009.05.004>.

120. Bonneville, S.; Smits, M.M.; Brown, A.; Harrington, J.; Leake, J.R.; Brydson, R.; Benning, L.G. Plant-driven fungal weathering: Early stages of mineral alteration at the nanometer scale. *Geology* **2009**, *37*, 615-618, doi:10.1130/g25699a.1.
121. Wild, B.; Daval, D.; Guyot, F.; Knauss, K.G.; Pollet-Villard, M.; Imfeld, G. pH-dependent control of feldspar dissolution rate by altered surface layers. *Chemical Geology* **2016**, *442*, 148-159, doi:https://doi.org/10.1016/j.chemgeo.2016.08.035.
122. Gautier, J.-M.; Oelkers, E.H.; Schott, J. Are quartz dissolution rates proportional to B.E.T. surface areas? *Geochimica et Cosmochimica Acta* **2001**, *65*, 1059-1070, doi:https://doi.org/10.1016/S0016-7037(00)00570-6.
123. Rodríguez-Iturbe, I.; Porporato, A. *Ecohydrology of Water-Controlled Ecosystems: Soil Moisture and Plant Dynamics*; Cambridge University Press: Cambridge, 2005; Doi: 10.1017/cbo9780511535727.
124. McCauley, A.; Jones, C.; Olson-Rutz, K. Soil pH and Organic Matter. In *Nutrient Management Module No. 8*, Montana State University Extension Service, Bozeman, Montana: 2017; pp. 1-12.

125. Porporato, A.; D'Odorico, P.; Laio, F.; Rodriguez-Iturbe, I. Hydrologic controls on soil carbon and nitrogen cycles. I. Modeling scheme. *Advances in Water Resources* **2003**, *26*, 45-58, doi:[https://doi.org/10.1016/S0309-1708\(02\)00094-5](https://doi.org/10.1016/S0309-1708(02)00094-5).
126. Morel, F.; Hering, J. *Principles and Applications of Aquatic Chemistry*; Wiley: 1993.
127. Maher, K.; Steefel, C.I.; White, A.F.; Stonestrom, D.A. The role of reaction affinity and secondary minerals in regulating chemical weathering rates at the Santa Cruz Soil Chronosequence, California. *Geochimica et Cosmochimica Acta* **2009**, *73*, 2804-2831, doi:<https://doi.org/10.1016/j.gca.2009.01.030>.
128. Bond-Lamberty, B.; Wang, C.; Gower, S.T. A global relationship between the heterotrophic and autotrophic components of soil respiration? *Global Change Biology* **2004**, *10*, 1756-1766, doi:<https://doi.org/10.1111/j.1365-2486.2004.00816.x>.
129. D'Odorico, P.; Laio, F.; Porporato, A.; Rodriguez-Iturbe, I. Hydrologic controls on soil carbon and nitrogen cycles. II. A case study. *Advances in Water Resources* **2003**, *26*, 59-70, doi:[https://doi.org/10.1016/S0309-1708\(02\)00095-7](https://doi.org/10.1016/S0309-1708(02)00095-7).
130. Daly, E.; Oishi, A.C.; Porporato, A.; Katul, G.G. A stochastic model for daily subsurface CO<sub>2</sub> concentration and related soil respiration.

- Advances in Water Resources* **2008**, *31*, 987-994, doi:<https://doi.org/10.1016/j.advwatres.2008.04.01>.
131. Riley, W.J.; Subin, Z.M.; Lawrence, D.M.; Swenson, S.C.; Torn, M.S.; Meng, L.; Mahowald, N.M.; Hess, P. Barriers to predicting changes in global terrestrial methane fluxes: analyses using CLM4Me, a methane biogeochemistry model integrated in CESM. *Biogeosciences* **2011**, *8*, 1925-1953, doi:10.5194/bg-8-1925-2011.
132. Rice, K.C.; Deviney, F.A.J.; Olson, G. Acid rain in Shenandoah National Park, Virginia. U.S. Geological Survey Fact Sheet 2007–3057: 2007; p. 4.
133. Coleman, N.T.; Mehlich, A. The chemistry of soil pH. USDA Yearbook, Washington, DC, USA: 1957; pp. 72-79.
134. Suarez, D.L.; Šimůnek, J. UNSATCHEM: Unsaturated Water and Solute Transport Model with Equilibrium and Kinetic Chemistry. *Soil Science Society of America Journal* **1997**, *61*, 1633-1646, doi:<https://doi.org/10.2136/sssaj1997.03615995006100060014x>.
135. Mau, Y.; Porporato, A. A dynamical system approach to soil salinity and sodicity. *Advances in Water Resources* **2015**, *83*, 68-76, doi:<https://doi.org/10.1016/j.advwatres.2015.05.010>.

136. Rodriguez-Iturbe, I.; Porporato, A.; Ridolfi, L.; Isham, V.; Coxi, D.R. Probabilistic modelling of water balance at a point: the role of climate, soil and vegetation. *Proceedings of the Royal Society of London. Series A: Mathematical, Physical and Engineering Sciences* **1999**, *455*, 3789-3805, doi:doi:10.1098/rspa.1999.0477.
137. Stumm, W.; Morgan, J.J. *Aquatic Chemistry: Chemical Equilibria and Rates in Natural Waters*; 1995.
138. Calabrese, S.; Parolari, A.J.; Porporato, A. Hydrologic Transport of Dissolved Inorganic Carbon and Its Control on Chemical Weathering. *Journal of Geophysical Research: Earth Surface* **2017**, *122*, 2016-2032, doi:https://doi.org/10.1002/2017JF004346.
139. Calabrese, S.; Porporato, A. Wetness controls on global chemical weathering. *Environmental Research Communications* **2020**, *2*, 085005, doi:10.1088/2515-7620/abad7b.
140. Atkinson, C.J.; Fitzgerald, J.D.; Hipps, N.A. Potential mechanisms for achieving agricultural benefits from biochar application to temperate soils: a review. *Plant and Soil* **2010**, *337*, 1-18, doi:10.1007/s11104-010-0464-5.
141. Pulido-Villena, E.; Reche, I.; Morales-Baquero, R. Significance of atmospheric inputs of calcium over the southwestern Mediterranean region: High mountain lakes as tools for detection. *Global*

- Biogeochemical Cycles* **2006**, *20*,  
doi:<https://doi.org/10.1029/2005GB002662>.
142. Groshans, G.R.; Mikhailova, E.A.; Post, C.J.; Schlautman, M.A.; Cope, M.P.; Zhang, L. Ecosystem Services Assessment and Valuation of Atmospheric Magnesium Deposition. *Geosciences* **2019**, *9*, 331.
143. Mikhailova, E.A.; Post, G.C.; Cope, M.P.; Post, C.J.; Schlautman, M.A.; Zhang, L. Quantifying and Mapping Atmospheric Potassium Deposition for Soil Ecosystem Services Assessment in the United States. *Frontiers in Environmental Science* **2019**, *7*, doi:10.3389/fenvs.2019.00074.
144. Suweis, S.; Rinaldo, A.; Van der Zee, S.E.A.T.M.; Daly, E.; Maritan, A.; Porporato, A. Stochastic modeling of soil salinity. *Geophysical Research Letters* **2010**, *37*,  
doi:<https://doi.org/10.1029/2010GL042495>.
145. Porporato, A.; Rodriguez-Iturbe, I. From random variability to ordered structures: a search for general synthesis in ecohydrology. *Ecohydrology* **2013**, *6*, 333-342,  
doi:<https://doi.org/10.1002/eco.1400>.
146. Pelak, N.; Revelli, R.; Porporato, A. A dynamical systems framework for crop models: Toward optimal fertilization and irrigation strategies under climatic variability. *Ecological Modelling* **2017**, *365*, 80-92,  
doi:<https://doi.org/10.1016/j.ecolmodel.2017.10.003>.

147. Weiß, M.; Menzel, L. A global comparison of four potential evapotranspiration equations and their relevance to stream flow modelling in semi-arid environments. *Adv. Geosci.* **2008**, *18*, 15-23, doi:10.5194/adgeo-18-15-2008.
148. Slessarev, E.W.; Lin, Y.; Bingham, N.L.; Johnson, J.E.; Dai, Y.; Schimel, J.P.; Chadwick, O.A. Water balance creates a threshold in soil pH at the global scale. *Nature* **2016**, *540*, 567-569, doi:10.1038/nature20139.
149. Merry, R.H. Acidity and Alkalinity of Soils. In *Environmental and Ecological Chemistry - Vol.II*, Sabljic, A., Ed. Eolss Publisher Co. Ltd., Oxford, United Kingdom: 2009; pp. 115-131.
150. Kopittke, P.M.; Menzies, N.W. A Review of the Use of the Basic Cation Saturation Ratio and the “Ideal” Soil. *Soil Science Society of America Journal* **2007**, *71*, 259-265, doi:https://doi.org/10.2136/sssaj2006.0186.
151. Shen, X.; Yang, F.; Xiao, C.; Zhou, Y. Increased contribution of root exudates to soil carbon input during grassland degradation. *Soil Biology and Biochemistry* **2020**, *146*, 107817, doi:https://doi.org/10.1016/j.soilbio.2020.107817
152. Wang, J.; Wang, X.; Xu, M.; Feng, G.; Zhang, W.; Yang, X.; Huang, S. Contributions of wheat and maize residues to soil organic carbon under long-term rotation in north China. *Scientific Reports* **2015**, *5*, 11409, doi:10.1038/srep11409.

153. Buchhorn, M.; Lesiv, M.; Tsendbazar, N.-E.; Herold, M.; Bertels, L.; Smets, B. Copernicus Global Land Cover Layers—Collection 2. *Remote Sensing* **2020**, *12*, 1044.
154. Hengl, T.; Mendes de Jesus, J.; Heuvelink, G.B.M.; Ruiperez Gonzalez, M.; Kilibarda, M.; Blagotić, A.; Shangguan, W.; Wright, M.N.; Geng, X.; Bauer-Marschallinger, B., et al. SoilGrids250m: Global gridded soil information based on machine learning. *PLoS One* **2017**, *12*, e0169748, doi:10.1371/journal.pone.0169748.
155. Fan, J.; McConkey, B.; Wang, H.; Janzen, H. Root distribution by depth for temperate agricultural crops. *Field Crops Research* **2016**, *189*, 68-74, doi:https://doi.org/10.1016/j.fcr.2016.02.013.
156. Clapp, R.B.; Hornberger, G.M. Empirical equations for some soil hydraulic properties. *Water Resources Research* **1978**, *14*, 601-604, doi:https://doi.org/10.1029/WR014i004p00601.
157. Laio, F.; Porporato, A.; Ridolfi, L.; Rodriguez-Iturbe, I. Plants in water-controlled ecosystems: active role in hydrologic processes and response to water stress: II. Probabilistic soil moisture dynamics. *Advances in Water Resources* **2001**, *24*, 707-723, doi:https://doi.org/10.1016/S0309-1708(01)00005-7.
158. FAO; ITPS. *Global Soil Organic Carbon Map (GSOCmap). Technical Report.*; Rome, 2018; p 162 pp.

159. Ballabio, C.; Lugato, E.; Fernández-Ugalde, O.; Orgiazzi, A.; Jones, A.; Borrelli, P.; Montanarella, L.; Panagos, P. Mapping LUCAS topsoil chemical properties at European scale using Gaussian process regression. *Geoderma* **2019**, *355*, 113912, doi:<https://doi.org/10.1016/j.geoderma.2019.113912>.
160. Hempel, J.; Libohova, Z.; Thompson, J.; Odgers, N.P.; Smith, C.; Lelyk, G.; Geraldo, G. GlobalSoilMap North American Node progress.
161. Libohova, Z.; Wills, S.; Odgers, N.P.; Ferguson, R.; Nesser, R.; Thompson, J.A.; West, L.T.; Hempel, J.W. Converting pH1:1 H<sub>2</sub>O and 1:2CaCl<sub>2</sub> to 1:5 H<sub>2</sub>O to contribute to a harmonized global soil database. *Geoderma* **2014**, *213*, 544-550, doi:<https://doi.org/10.1016/j.geoderma.2013.08.019>.
162. Hartmann, J.; Moosdorf, N. The new global lithological map database GLiM: A representation of rock properties at the Earth surface. *Geochemistry, Geophysics, Geosystems* **2012**, *13*, doi:<https://doi.org/10.1029/2012GC004370>.
163. Plummer, L.N.; Parkhurst, D.L.; Wigley, T.M.L. Critical Review of the Kinetics of Calcite Dissolution and Precipitation. In *Chemical Modeling in Aqueous Systems*, AMERICAN CHEMICAL SOCIETY: 1979; Vol. 93, pp. 537-573.

164. Singer, M.B.; Asfaw, D.T.; Rosolem, R.; Cuthbert, M.O.; Miralles, D.G.; MacLeod, D.; Quichimbo, E.A.; Michaelides, K. Hourly potential evapotranspiration at 0.1° resolution for the global land surface from 1981-present. *Scientific Data* **2021**, *8*, 224, doi:10.1038/s41597-021-01003-9.
165. Bruni, E.; Guenet, B.; Clivot, H.; Kätterer, T.; Martin, M.; Virto, I.; Chenu, C. Defining Quantitative Targets for Topsoil Organic Carbon Stock Increase in European Croplands: Case Studies With Exogenous Organic Matter Inputs. *Frontiers in Environmental Science* **2022**, *10*, doi:10.3389/fenvs.2022.824724.
166. Johan van den Hoogen; Jonas Lembrechts; SoilTemp; Ivan Nijs; Lenoir, J. Global Soil Bioclimatic variables at 30 arc second resolution. 2021; 10.5281/zenodo.4558732.
167. Vico, G.; Porporato, A. From rainfed agriculture to stress-avoidance irrigation: II. Sustainability, crop yield, and profitability. *Advances in Water Resources* **2011**, *34*, 272-281, doi:https://doi.org/10.1016/j.advwatres.2010.11.011.
168. Vico, G.; Porporato, A. From rainfed agriculture to stress-avoidance irrigation: I. A generalized irrigation scheme with stochastic soil moisture. *Advances in Water Resources* **2011**, *34*, 263-271, doi:https://doi.org/10.1016/j.advwatres.2010.11.010.

169. Cipolla, G.; Calabrese, S.; Noto, L.V.; Porporato, A. The role of hydrology on enhanced weathering for carbon sequestration II. From hydroclimatic scenarios to carbon-sequestration efficiencies. *Advances in Water Resources* **2021**, *154*, 103949, doi:<https://doi.org/10.1016/j.advwatres.2021.103949>.
170. Du, E.; Terrer, C.; Pellegrini, A.F.A.; Ahlström, A.; van Lissa, C.J.; Zhao, X.; Xia, N.; Wu, X.; Jackson, R.B. Global patterns of terrestrial nitrogen and phosphorus limitation. *Nature Geoscience* **2020**, *13*, 221-226, doi:10.1038/s41561-019-0530-4.
171. Wieder, W.R.; Allison, S.D.; Davidson, E.A.; Georgiou, K.; Hararuk, O.; He, Y.; Hopkins, F.; Luo, Y.; Smith, M.J.; Sulman, B., et al. Explicitly representing soil microbial processes in Earth system models. *Global Biogeochemical Cycles* **2015**, *29*, 1782-1800, doi:<https://doi.org/10.1002/2015GB005188>.
172. Manzoni, S.; Porporato, A. Soil carbon and nitrogen mineralization: Theory and models across scales. *Soil Biology and Biochemistry* **2009**, *41*, 1355-1379, doi:<https://doi.org/10.1016/j.soilbio.2009.02.031>.
173. Hao, T.; Zhu, Q.; Zeng, M.; Shen, J.; Shi, X.; Liu, X.; Zhang, F.; de Vries, W. Quantification of the contribution of nitrogen fertilization and crop harvesting to soil acidification in a wheat-maize

---

double cropping system. *Plant and Soil* **2019**, *434*, 167-184, doi:10.1007/s11104-018-3760-0.